Effects of Bi on the Morphology and Atomic Structure of III-V Semiconductor Surfaces

by

Adam James Duzik

A dissertation submitted in partial fulfillment
of the requirements for the degree of
Doctor of Philosophy
(Materials Science and Engineering)
in The University of Michigan
2013

Doctoral Committee:

Professor Joanna M. Millunchick, Chair
Professor Chris A. Pearson
Associate Professor Jamie D. Phillips
Professor Anton Van der Ven

For my Lord and Savior, through the hands of His holy mother.

ACKNOWLEDGEMENTS

In my humble estimation it is only by the grace of God Almighty that I have made it to this point. Only by His divine Providence have I overcome the large number of setbacks, seemingly endlessly broken equipment, and the trail of dead Bi cells and crucibles left in my wake. Only by His workings in His many mysterious ways through the things and people of my life to overcome the slings and arrows of graduate school. Truly, I am blessed and privileged to have even gone on this journey, let alone finish it. Deo gratias (thanks be to God), indeed!

I would be remiss if I did not mention how much I owe to several people. I would like to thank my advisor, Prof. Joanna Millunchick, who has taught me much, not only about how to do research, but how to write and present about it well, and how to deal calmly with broken, expensive equipment. Such calm under that pressure is not lost on me. Truth be told, a lesser person would have broken when considering the baffling ordeal of maintaining the chamber and the litany of horrors the group has had to deal with in the last five years.

I also must thank my group mates, past and present, for their teaching me how to use the equipment, how to do simulations, and for being my brothers and sisters in arms for when the MBE chamber needs to be fixed. Special thanks to Lee "Trey" Sears, Jennifer Lee-Feldman, Jessica Bickel, and Kevin Grossklaus for showing me how to run the MBE without breaking it. Special thanks to John C. Thomas, for his patient and knowledgable guidance in all the simulation work I have done. I would also like to thank Dr. Normand Modine for being a wonderful collaborator

out at Sandia; truly, I looked forward to my annual August visits that were always illuminating and worthwhile.

I also want to thank and to wish my best to Matt DeJarld, Evan Anderson, Lifan Yan, Garrett Rodriguez, and Ryan Tait as I commend care of the lab into your capable hands. I hope and pray I have not been negligent in teaching you all that I know. May my experiences serve you all well and may I have made all the mistakes so you don't have to.

I would also like to thank my friends, Mike Waters, Jake Jokisaari, Eleanor Coyle, Dr. Susan Gentry, Ryan Breneman, Dr. Mike Katz, and especially Dr. Anne Juggernauth who offered great consolation and comfort during my time here in Michigan. You all taught me to be a little braver and to try new things; I am a better person for it. I also must thank all those I worked with on opposing the insanity of the GSRA unionization campaign. Special thanks to Stephen Raiman, Anna Belak, Layla Houshmand, Dr. Melinda Day, Dr. Paul Guiliano, Bill Rosemurgy, and all the others for keeping me motivated and giving me the confidence that we could prevail. Extra special thanks to Patrick Wright for helping us lead the charge. You truly made all the difference in our struggle.

Last, but certainly not least, I must thank my family and especially my parents who have moved heaven and earth to help me finish. I would never even have gotten here if it were not for all the years of teaching me to be a decent, God-fearing, red-blooded American and upstanding citizen. Graduate school is not for the weak, but you made me strong enough to do it. That said, after all the trials and tribulations, after all the dust has settled, I feel vindicated that the following applies:

"I know how to be abased, and I know how to abound; in any and all circumstances I have learned the secret of facing plenty and hunger, abundance and want. I can do all things in him who strengthens me."

St. Paul, Phillipians 4:12-13

"I have fought the good fight, I have finished the race, I have kept the faith"

St. Paul, 2 Timothy 4:7

The Holy Bible, Revised Standard Version, Second Catholic Edition

TABLE OF CONTENTS

LIST OF FIGURES

Figure

LIST OF TABLES

Table

LIST OF APPENDICES

Appendix

LIST OF ABBREVIATIONS

AFM atomic force microscopy

AGR absolute growth rate

BEP beam equivalent pressure

BFM beam flux monitor

BGR Bi relative growth rate

CASM Cluster Assisted Statistical Mechanics

DFT density functional theory

ECI effective cluster interaction

ECM electron counting model

EDS energy-dispersive spectroscopy

EXAFS extended x-ray absorption fine spectra

FWHM full-width, half-maximum

HRXRD high resolution x ray diffraction

LDA local density approximation

LEED low-energy electron diffraction

MBE molecular beam epitaxy

ML monolayer

MLS micron length scale

ML/s monolayers per second

NLS nanometer length scale

NNN next-nearest neighbors

PID proportional-integral-differential

RBS Rutherford backscatter spectroscopy

RHEED reflective high-energy electron diffraction

SEM scanning electron microscopy

SIMS secondary ion mass spectroscopy

sMC statistical Monte Carlo

SOS solid-on-solid

STM scanning tunneling microscopy

STS scanning tunneling spectroscopy

UHV Ultra-high Vacuum

VASP Vienna *ab-initio* Simulation Package

XRD x-ray diffraction

ABSTRACT

Effects of Bi on the Morphology and Atomic Structure of III-V Semiconductor Surfaces

by

Adam James Duzik

Chair: Joanna M. Millunchick

Use of Bi in III-V semiconductor films in recent years has a variety of applications. Bi lowers the bandgap, introduces a large spin-orbit coupling, and preserves electron mobility, enabling low bandgap, high mobility and novel spintronic devices. Bi is also a nearly ideal surfactant, smoothing the surface, creating the right conditions for a sharp, high quality interface. However, the mechanism for this behavior and the atomic surface reconstructions are poorly characterized, both for surface- and bulk-incorporated Bi. This dissertation consists of four studies to investigate this behavior.

The first half explores the effects of Bi as an ideal surfactant. The first study is an experimental scanning tunneling microscopy characterization of the Bi/GaAs surface, revealing the same reconstruction appears for the observed (1x3), (2x3), and (4x3) reflective high-energy electron diffraction patterns. Steps become wider on the micron length scale from the induced smoothing, owing to the increase of opposite direction step edges on the nanometer length scale. The second study is a combined cluster expansion aand density functional theory (DFT) analysis of the Bi/GaAs

reconstructions. The (4x3) reconstruction was found to stabilize into a variety of compositions in the presence of Bi. Monte Carlo analysis of the (4x3) reconstruction shows a strong propensity for surface disorder even at temperatures well below Bi deposition temperatures.

The second half focuses on the surface effects of incorporated Bi. In the third study, several GaSbBi films were grown as a function of Ga, Sb, and Bi growth rates. Biphasic droplets were observed, with sub-droplets, facets, and etching into the film. X-ray diffraction and Rutherford backscatter measurements showed a concurrent increase in Bi and As concentration, indicating a previously unseen strain auto-compensation mechanism. The fourth study is a cluster expansion/DFT characterization of the Bi/GaSb surface system as a proxy for the GaSbBi surface. In particular, the c(2x10) reconstruction was investigated for the bare GaSb and Bi/GaSb systems, where the instability of this reconstruction was established in a rigorous manner. Finally, the Bi-induced (2x1) reconstruction was found to be stable in the Bi/GaSb system, consistent with other Bi/III-V systems.

CHAPTER I

Introduction

The rapid explosion of technology into daily life has driven the demand for higher quality semiconductor devices, particularly in optoelectronic devices such as solar cells, light emitting diodes, photodetectors, and lasers. As such, the importance of the direct bandgap III-V semiconductors such as GaAs, InAs, and GaSb, has increased. These materials consist of one group III element as a positively charged cation species and a group V element as a negatively charged anion species. III-V semiconductors are particularly applicable to making optoelectronic devices owing to the direct energy bandgap that permits easy absorption and emission of photons. Depending on the bandgap of the semiconductor, devices can be tailored to specific wavelengths of light. Heterostructure devices exploit this behavior using differences in energy bandgaps between two dissimilar III-V semiconductors. These are known as heterostructure devices. A common means of producing these devices is through molecular beam epitaxy (MBE), a method for depositing the constituent elements of the desired semiconductor onto a III-V substrate.

1.1 Surface Reconstructions

At the surface created by cleaving a bulk crystal, the octet rule for the atoms at the surface is no longer satisfied. These atoms will bond to one another in order to

reduce the surface energy, causing these atoms to reconstruct into a different structure at the surface. The type of reconstruction that appears depends heavily on the bulk crystal structure, the atomic species involved, and the crystallographic orientation of the cleavage plane.

Most III-V semiconductors have a zinc blende bulk crystal structure, including GaAs and GaSb, the two materials studied in this work. A unit cell of the zinc blende crystal structure is shown in Fig. 1.1. In this work, all the surface reconstruction studies focused on those of the (001) plane. The {001} family of planes are parallel with the faces of the unit cell in Fig. 1.1 and are either all cation or all anion terminated. Because of this, surface reconstructions are referred to as anion terminated or cation terminated, but in practice, anion terminated surfaces are the most common as any excess in group V anion species do not form undesirable metallic droplets on the surface like group III cation elements do. As such, surfaces are often subjected to a constant incoming anion flux to maintain the anion-terminated surface and to prevent anion desorption.

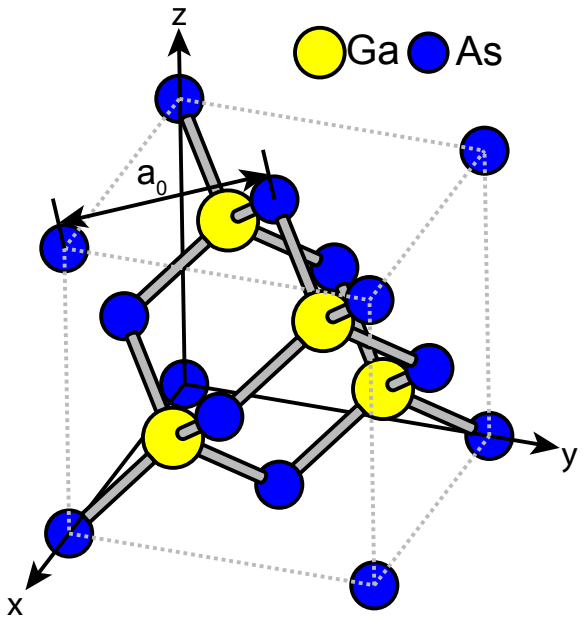

Figure 1.1. Zinc blende crystal structure unit cell. The distance a_0 is the shortest surface spacing between two adjacent atoms in the [110] and [$\bar{1}$10] directions.

Surface atoms commonly form dimers when reconstructing, which bond along the $\langle 110 \rangle$ family of directions on the (001) plane, as shown in Fig. 1.1. This is the shortest distance between two dimerizing atoms at the surface, specified as a_0. All surface reconstruction unit cells are measured in multiples of a_0. The convention in specifying a reconstruction is $(x \times y)$, where x and y are the in-plane multiples of a_0 *normal* to the [110] and $[\bar{1}10]$ directions, respectively. Several examples of the common reconstructions on the GaAs(001) surface are shown in Fig. 1.2. Prefixes such as "$\alpha 2$" and "$\beta 2$" distinguish reconstructions of the same size but different atomic arrangement. In some cases, the edges of the reconstruction unit cell are not aligned with the [110] and $[\bar{1}10]$ directions, such as the case of the $c\,(4 \times 4)$ reconstruction. The "c" designation stands for "centered", and is used when a feature, such as the three dimers in the $c\,(4 \times 4)$ reconstruction, are staggered and do not line up along the [110] or $[\bar{1}10]$ directions.

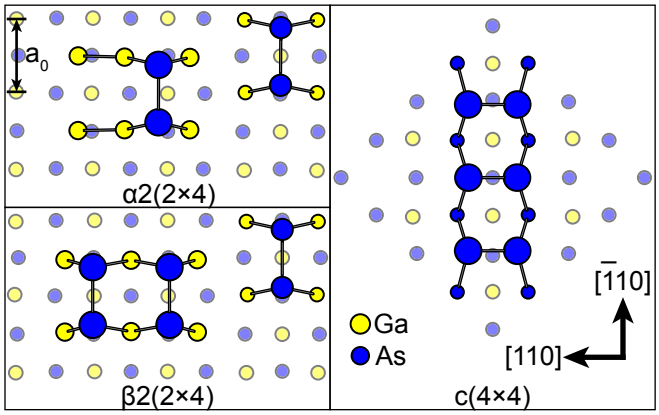

Figure 1.2. Common GaAs(001) surface reconstructions. The distance a_0 is the same spacing as in Fig. 1.1.

1.2 Bi-containing III-V Semiconductors

More recently, the Bi has gained a great deal of attention in this field. Several studies into Bi incorporation into GaAs to form GaAsBi have shown a number of useful advantages, such as a large bandgap reduction,[3, 4, 5, 6, 7, 8, 9] preservation

of electron mobility,[10, 11, 12, 13, 14] and a large spin-orbit coupling for potential use in novel spintronic devices.[15, 16] Similarly, Bi has been shown to cause a bandgap reduction in GaSb,[17] useful for obtaining low energy bandgaps for use in long-wavelength optoelectronic devices. However, Bi is the largest group V element, preferring to surface segregate rather than incorporate.[18] Such behavior necessitates the need for low growth temperatures and As:Ga ratios of $\sim$1 in order to achieve appreciable incorporation. On the other hand, Bi is a nearly ideal surfactant, causing a surface smoothing effect without changing the underlying device composition. Such behavior is useful to obtaining sharp interfaces for high-quality devices.

This surfactant behavior has been well characterized on the micron length scale (MLS) but is poorly understood on the nanometer length scale (NLS). The atomic surface structure, known as the surface reconstruction, is only understood for a limited set of conditions. Work by Laukkanen *et al.* show that after room temperature Bi deposition onto GaAs, Bi-induced (2×1) and $\alpha 2\,(2 \times 4)$ surface reconstructions appear.[19, 20, 21] Under typical conditions observed in MBE, other work by Young and Masnadi-Shirazi *et al.* relied on reflective high-energy electron diffraction (RHEED) for characterizing the reconstruction as having an $(n \times 3)$ periodicity during growth.[22, 23] Such methods only provide periodicity information, and while the surface reconstruction influences the final bulk atomic structure and ordering,[24, 25] detailed information about these surface reconstructions is lacking. **This dissertation is a comprehensive study of the atomic structure, ordering, and stability of the Bi-induced surface reconstructions on the (001) surface plane under MBE conditions that produces the corresponding MLS morphology.**

1.3 Topics

A wide variety of experimental and computational methods were applied to understanding the Bi-induced surface reconstructions on GaAs and GaSb, all of which are described in Ch. II. Chapter III is a combined RHEED, scanning tunneling microscopy (STM), and atomic force microscopy (AFM) study of the Bi/GaAs system produced via MBE. STM of the surface shows a large increase in the step edge density, resulting in a great deal of height modulation on the NLS. High resolution STM images were used to identify a model for the observed disordered $(n \times 3)$ reconstruction; based on the observed structure and row spacing, the (4×3) reconstruction is proposed as the model. A mechanism is also proposed for the surface smoothing observed on the MLS with AFM, where the decrease in roughness is attributed to the increase in step edge density observed in the STM causing a suppression of step trains on the MLS.

While experimental characterization with STM provides many useful details on the $(n \times 3)$ reconstruction, including a suggested model, several issues still remain with characterizing this reconstruction. Limits on STM resolution and the surface disorder prevent characterization of variations in composition in the $(n \times 3)$ reconstruction. The stability of this reconstruction relative to the other GaAs reconstructions is also poorly understood. Chapter IV is a cluster expansion study of the thermodynamic stability of the GaAs(001) reconstructions, including the (4×3) and (2×1) reconstructions, as determined from density functional theory (DFT) calculations of various compositional configurations and comparison of the final energies result in the 0 K phase diagram of the Bi/GaAs surface reconstructions. Monte Carlo simulations of the (4×3) configurations reveal this reconstruction is inherently disordered, consistent with the experimental observations of Ch. III.

Chapters III and IV show the effects of Bi as a surfactant on the GaAs surface, but the effects of incorporated Bi on the same remains to be explored. Chapter V

is an investigation of the surface morphology of GaSbBi/GaSb films. Surface droplet formation is observed with scanning electron microscopy (SEM) and AFM, which are discovered to be biphasic, with Ga-rich and Bi-rich phases. RBS and x-ray diffraction (XRD) analysis of the films show simultaneous Bi *and* As concentration, indicating a strain auto-compensation mechanism occurs during growth, as also evidenced by the calculated strain relaxation.

The GaSbBi(As)/GaSb films of Ch. V were too rough and covered in droplets to analyze experimentally with STM. As an alternative, the reconstructions of the Bi/GaSb system were explored in Ch. VI with the cluster expansion and DFT methods. In particular, the $c\,(2 \times 10)$ reconstruction is explored, which is also proposed as the Sb-rich reconstruction that appears on GaSb in place of the common $c\,(4 \times 4)$ reconstruction that appears under As-rich conditions in GaAs and InAs.[26, 27] $\mathrm{Ga_{Sb}}$ anti-site defects in the $c\,(2 \times 10)$ reconstruction have been suggested as the reason for the stability of this reconstruction,[28, 29, 30] but the exact location of these defects is unknown. As such, the stability of all the GaSb reconstructions must be established first, then that of the Bi/GaSb reconstructions. From the cluster expansion it is seen the (4×3) reconstruction is stable under all conditions for both systems.

CHAPTER II

Background

Growth of the samples needed to study the effects of Bi on III-V semiconductors requires particular equipment and methods. A high degree of cleanliness is required; even trace amounts of water molecules, organic molecules, or carbon-containing gases such as CO or CO_2 can form undesirable trap states and defects in a III-V crystal. Several techniques for producing and analyzing these samples were used in this work, the details of which are given below.

2.1 Molecular Beam Epitaxy (MBE)

All sample preparation and growth is carried out under ultra-high vacuum (UHV) conditions in an EPI 930 MBE chamber, which consists of several components necessary for producing samples. A model of an MBE chamber is shown in Fig. 2.1.[1] The first component is the vacuum chamber itself, which is sealed tightly enough to attain UHV pressures. Samples are introduced via a load lock introduction vacuum chamber that can be vented and evacuated independently from the main MBE chamber. Once the introduction chamber is pumped down sufficiently, samples are introduced into the MBE chamber via a buffer chamber, which connects the MBE chamber with the STM chamber, allowing sample transfer between the two chambers entirely under vacuum, preserving the as-grown sample surface from atmospheric contamination.

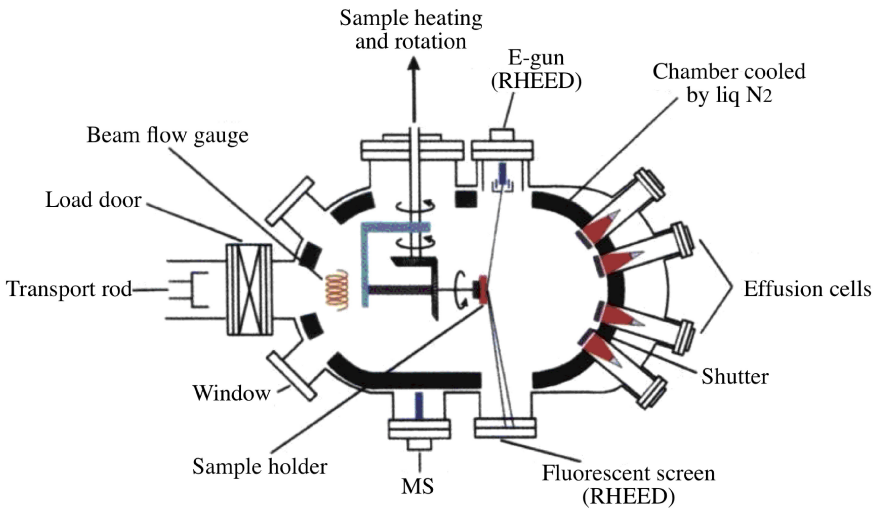

Figure 2.1. Model of an MBE chamber. Taken from [1].

Vacuum is achieved and maintained through the use of several pumps. A scroll pump attached to the introduction chamber is used when pumping from atmosphere, lowering the pressure of the MBE chamber to $\sim 1 \times 10^{-3}$ torr. A turbomolecular pump, also attached to the introduction chamber, is then used to pump down to $\sim 1 \times 10^{-8}$ torr. These two pumps are used for evacuating the introduction chamber after loading samples, or for evacuating the MBE or STM chambers after venting these to atmosphere for maintenance.

When evacuating the MBE chamber, the turbomolecular pump reduces pressure to only $\sim 1 \times 10^{-4}$ torr, on account of the larger volume. At this point the ion pump is activated, which lowers the pressure further to $\sim 1 \times 10^{-6}$ torr (as measured by an ion gauge), after which the scroll and turbomolecular pumps are closed off from the MBE chamber via a gold seal valve. With the ion pump maintaining vacuum in the MBE chamber, it is then aided by a cryogenic pump, lowering the overall pressure down to $\sim 1 \times 10^{-8}$ torr. The partial pressures of the individual contaminants were below the UHV threshold of $\sim 1 \times 10^{-10}$ torr. While this is sufficient for when the chamber is not in active use, the vacuum is improved still further by running liquid N_2 through a cryogenic shroud in the walls of the MBE chamber, achieving maximum

cleanliness while performing epitaxial growth.

Substrates consisted of cleaved pieces broken off of larger wafers. All these wafers were cut from commercially produced single crystal ingots such that the surfaces are parallel with the (001) crystal lattice plane. The wafers were cleaved into smaller pieces with a diamond-tipped scribe along the {110} family of lattice planes; these planes then correspond to the edge faces of the sample. Sizes ranged from 0.5-1.5 cm along an edge, with the smaller sizes needed for mounting on Mo scanning tunneling microscopy (STM) sample blocks. The larger ones were mounted on plain Mo blocks and were more suitable for RHEED, XRD, SEM, and RBS analysis. In either case, samples were adhered to the blocks via In bonding, where the capillary force of liquid In metal is used to hold the sample in place during growth. Samples are baked to 150°C in the introduction chamber after establishing vacuum in order to remove surface oxide and atmospheric contaminants. The sample is then loaded into the MBE chamber and engaged with the substrate holder, which can be heated to the necessary temperatures. The particulars of growth conditions for the GaAs and GaSb samples will be discussed within the individual chapters.

The principle of vapor pressure is used to deposit material on the substrate. Source material is loaded into a pyrolytic boron-nitride (PBN) crucible, which in turn is loaded into a Knudsen effusion cell. The cell heats the crucible and source material by resistive heating, which is controlled by a power supply with a proportional-integral-differential (PID) temperature controller to maintain temperature as measured by a thermocouple. Individual cells for Ga, In, Al, Bi, Be, and Si were present on the MBE chamber used in this work. Shutters are used to block the fluxes when not growing, giving precise control over the final thickness of the growth.

The group V elements As and Sb require more specialized equipment known as a valved cracker to produce a useable flux of those elements. Like in the Knudsen cells, the As or Sb source material is placed in a crucible which can be heated. The

evaporated molecules are then directed through a cracking zone, which can be heated independently with a separate PID controller to a higher temperature than the bulk source material. As molecules dissociates smaller molecules more suitable for MBE growth when traveling through the cracking zone. A Veeco mark IV As cracker used in this work produced As tetramers (As_4, $T^{As}_{Cracker} = 600°C$) or As dimers (As_2, $T^{As}_{Cracker} = 1000°C$). Sb was primarily used in atomic form (Sb_1) with some Sb dimers (Sb_2) for $T^{Sb}_{Cracker} = 900°C$.[31] In this work, As_4 and Sb_1/Sb_2 molecules were used.

2.1.1 Bi Effusion Cell

Given the novelty of using Bi in MBE applications, special mention of the Bi source and potential hazards is in order. Unlike As and Sb, Bi does not require a valved cracker to produce a usable flux, but is rather placed in a standard Knudsen cell. Various crucible designs were considered to find the one least prone to fracture via thermal expansion. Each crucible had a 40 cc capacity and were all cylindrical, loaded with about 100-150 g of Bi. Flat-bottomed crucibles were found to have large stress concentrations at the corners, and were susceptible to breaking while cooling the Bi source material in both the single-walled and double-walled variants. A rounded-bottom crucible was tried to ameliorate the issue, but it too eventually broke during cooling.

The issue is the fact that Bi, like Ga, expands ≈3.3% upon freezing. Even cooling at slow rates of 1°C/min. or lower did not help. After several broken crucibles, the cell was redesigned to a larger 150cc crucible and loaded with less source material (about 30g) than in the 40cc crucible. Finally, the new cell was attached in a more horizontal position. These three steps prevent the Bi source material from contacting all the side wall around the bottom of the crucible; this permitted room for the source material to expand upon freezing. To date, no issues with this configuration have been seen.

The temperature of the cell was controlled with a PID controller on a single power supply. Any attempt to auto-tune the PID parameters near the Bi melting point (271°C) would be dangerous, as the auto-tune algorithm induces a large temperature oscillation over a short period of time. Tuning near the melting point is not an option. As an alternative, manually controlling the output power was automated through the use of the Amber control software. Heating from room temperature to 200°C was done normally with PID control, after which the controller was set to manual mode, where the output power is controlled directly. The current limit was set from 10A to 5.5A, providing a finer control over the output power. The Amber software was then programmed to increase the output power percentage by 0.2-0.3% every 2-3 minutes, producing a steady increase in Bi cell temperature of less than 1°C/min. A similar procedure was done for cooling through the melting point, where output power was decreased 0.2-0.3% every 3 minutes, cooling the cell at a rate of less than 1°C/min.

2.2 Reflective High-energy Electron Diffraction (RHEED)

An in-situ technique carried during epitaxial growth, the RHEED system consists of an electron source and a phosphorescent screen. A focused electron beam is produced from the source that impinges on the surface at a glancing incidence angle of around 2-3° with respect to the sample surface plane. The electrons diffract off the sample surface into the screen, producing a diffraction pattern, as shown in Fig. 2.2. Given the glancing angle of incidence, the electrons do not penetrate deeply into the sample, causing all diffraction information to come from the surface only; this provides many useful details on the surface conditions.

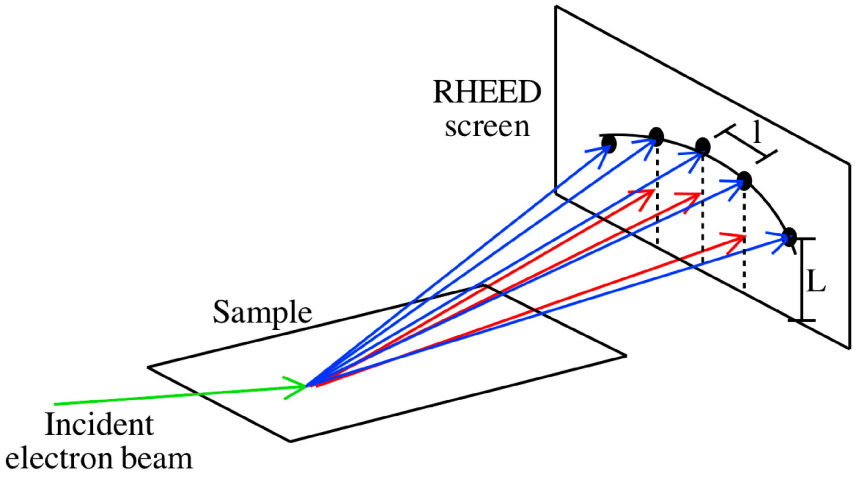

Figure 2.2. Model of RHEED. Taken from [1].

A rough surface will produce a spotty RHEED pattern, useful for identifying the onset of quantum dot nucleation or 3D island growth, while streaks in the RHEED pattern indicate a flat surface. Streaky RHEED patterns also provide useful information on the periodicity of the atomic surface reconstruction, that is the rearrangement of undercoordinated atoms at the surface. Principle streaks appear from the sampling of the underlying bulk periodicity of the crystal lattice, and because this periodicity is the smallest in real space these streaks are the furthest spaced in reciprocal space. Non-principle streaks arise from longer-range periodicities in the surface reconstruction, corresponding to a smaller spacing between these streaks in the RHEED pattern (see Fig. 2.3). In real space, the periodicity in the surface structure is in multiples of the surface lattice constant, meaning the number of non-principle streaks between the principle streaks is a measure of how many lattice constant spacings the structure spans.

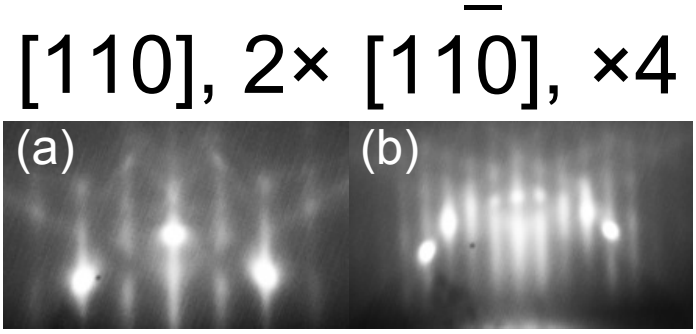

Figure 2.3. RHEED image of the $\beta 2\,(2 \times 4)$ surface. (a) RHEED of the [110] zone axis showing the 2× periodicity. (b) RHEED of the [$\bar{1}$10] zone axis showing the ×4 periodicity.

All RHEED measurements in this work were performed during MBE growth with a Staib Instrumente RHEED system operated at 15 kV and 1.5 mA with a k-Space phosphorescent screen. RHEED images and movies were recorded using a k-Space RHEED camera setup and the corresponding KSA400 software. Image collection focused primarily upon either the [110] or [$\bar{1}$10] zone axes, that is along the easily cleaved edges of the sample with a (001) surface. Surface reconstruction of surface atoms aligns along these edges, and are hence the most important directions for determining reconstruction periodicity.

2.2.1 Oscillations

A particularly useful technique used in RHEED is to measure the growth rate of the film by tracking the oscillation in RHEED specular spot intensity. In the initial stage, prior to any growth, the surface is flat, electron scattering is low, and the RHEED intensity is high. As the growth starts, new islands are nucleated and begin to grow, temporarily increasing roughness and electron scattering. Thus, the RHEED intensity drops. This continues as new islands form and old ones grow, until the scattering is maximized. After this, the islands begin to merge with one another as more incident atoms attach to the surface, causing roughness to decrease. The

RHEED intensity begins to increase again, until the layer is completed and the flat surface is restored, resulting in maximum RHEED intensity again. Then the process repeats with the next layer. The time between the peaks in RHEED intensity is the time it takes for one monolayer (ML) to grow in seconds. Averaging over several peaks gives an accurate measurement of the growth rate.

Since III-V semiconductors are compound materials, RHEED will measure the growth rate of the least available species. For instance, to measure the Ga rate on GaAs, the As overpressure is set such that the As rate is known to be 2-4 times the Ga rate. The frequency of intensity oscillation is then attributed to Ga, the rate limiting species. An analogous procedure can be done for other group III elements such as Al and In. Measurement of group V elements requires an excess of the group III species. A continuous flux of Ga would result in surface droplet formation, ruining the surface; instead, only a limited amount of Ga is deposited under no As overpressure to produce a Ga-terminated surface. Shutting off the Ga flux and turning on the As flux results in a brief period of growth limited by As flux, where the incoming As is reacting with the surface Ga to grow the layer. The intensity oscillation is tracked during this process, which is known as an uptake oscillation as the excess Ga "takes up" all the incoming As.

2.3 Scanning Tunneling Microscopy (STM)

2.3.1 Principle of Operation

After sample growth, samples were transferred under vacuum into an RHK STM100 STM system, allowing the atomic surface structure to be imaged without interference from surface oxide. STM uses the principle of quantum tunneling to infer the surface topography from the orbital states of the surface atoms, as demonstrated in Fig. 2.4.[2] An atomically sharp tip (W in this work) is lowered via piezoelectric ac-

tuators such that the tip atom is within a few angstroms of the surface atoms. With only one atom at the tip, there is one orbital that protrudes out from the tip, and this interacts with the orbitals protruding from the surface. As the tip is scanned laterally over the surface, the orbitals overlap, and electrons tunnel either from the surface atom to the tip atom or from the tip to the surface, depending on the voltage bias placed across the tunneling gap. Negative bias in this work indicates the surface is negatively biased relative to the tip while positive bias indicates the tip is negatively biased relative to the surface. The first condition is also referred to as forward bias while the latter is called reverse bias.

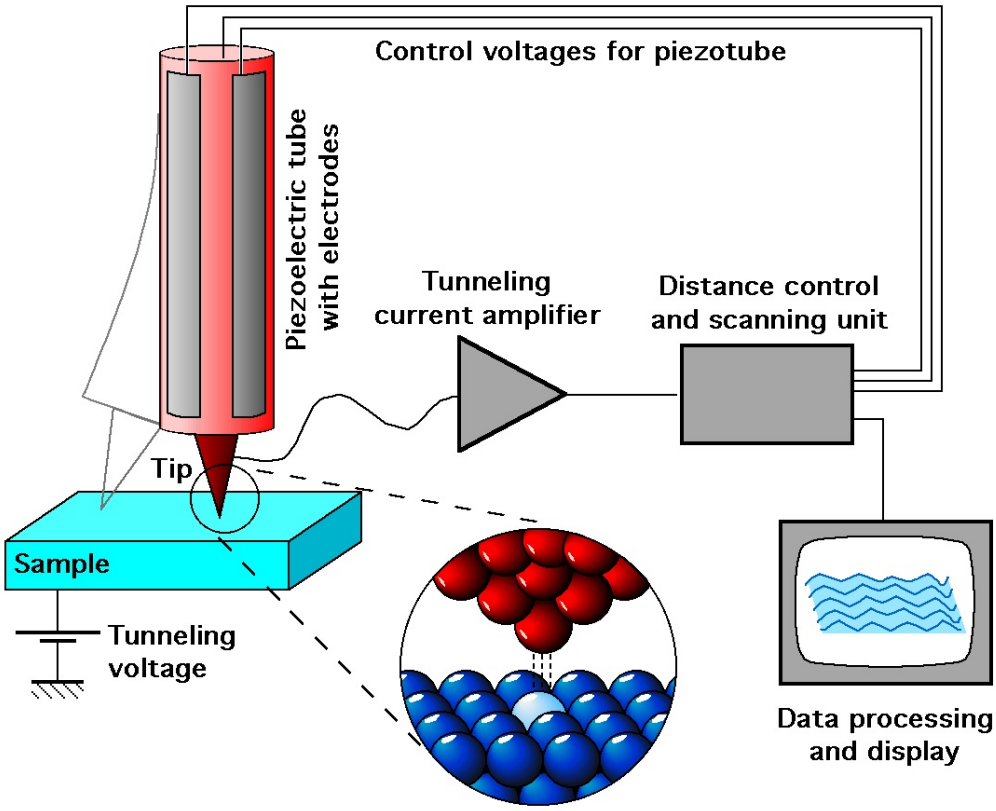

Figure 2.4. Model of the STM setup for mapping surface topography. Figure generated by Michael Schmid, TU Wien.[2]

As such, a forward bias would raise the filled anion states relative to the Fermi level in the tip, causing ready tunneling from the surface anions to the tip. Any

surface cations do not have electrons in their conduction band states, and are not resolved. This is called filled states imaging. The reverse, known as empty states imaging, occurs under reverse bias, where the tip Fermi level is raised relative to that of the surface Fermi level. Electrons will not tunnel from the tip to the surface anions since those states are already filled, but they will tunnel to the empty valence band states in the cations. Hence, in this mode cations are easily visible and anions are not resolved. In this work, the surfaces studied were all anion-terminated. Thus, the imaging was all done under forward bias.

2.3.2 Sample Mounting and Tip Approaching

All samples prepared for STM imaging were mounted on Mo blocks designed for use with the STM100 system. Since samples were imaged after growth without removing them from vacuum, the Mo blocks had to be compatible with both the MBE chamber and the STM chamber. Each block had three keyholes machined out on the edges for interlocking with the holding pins on the MBE substrate manipulator, while the center of the block contained a small sample mounting area surrounded by three ramps (see Fig. 2.5). Samples are mounted with liquid In bonding in the same manner as with standard Mo blocks, although the samples are smaller in order to fit in the space between the ramps.

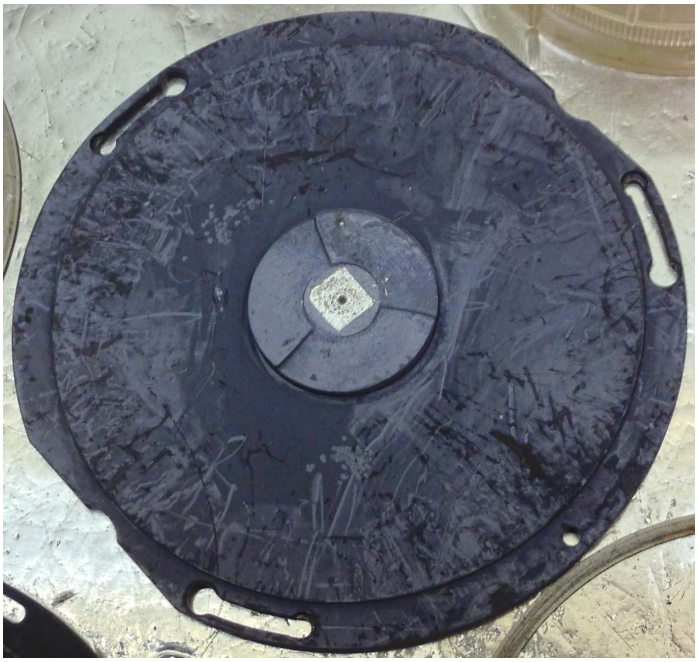

Figure 2.5. Photo of a STM Mo mounting block used in this work

In the STM100 system, the tip is held in the center of a scan head that has three legs evenly spaced on the outside of the head. Each leg is equipped with piezoelectric actuators to control displacement in all three dimensions. When lowered onto the Mo block, the scan head legs sit on the ramps, allowing small, highly controlled displacements of the tip towards the surface as the piezoelectric actuators "walk" the legs down the ramps. Initially, the tip is far away from the surface and a fast, continuous approach may be used, but upon getting closer to the surface, a more cautious approach is used. In this step of the approach, the legs walk down the ramps a certain amount, then retract slightly, resulting in an incremental approach until the tip orbital engages with the surface orbitals, after which the approach is complete and imaging may begin.

2.3.3 Tip Preparation

All tips used in this work were made of etched W produced in a homemade tip etching system. This system uses electrochemical etching between a piece of W wire

feed through the center of a stainless steel ring electrode, both of which are just barely submerged beneath the surface of a 5M aqueous solution of NaOH. A power supply drives the reaction, causing the wire to etch away at the section of wire in the plane of the ring electrode. As the reaction progresses, a neck starts to form in the wire, until eventually the current spikes from the small amount of remaining W in the neck. This indicates the two halves are nearly separated, and a differentiator is used to cut the current when this spike occurs past a certain current threshold. Otherwise, the reaction would continue too long and the atomically sharp point would be etched away. Upon finishing etching, a new tip was removed from the setup and cleaned with distilled water and then acetone before promptly loading it into vacuum on a tip holder before W oxide formation progressed too far. Tip holders consist of the housing and the sheath that directly holds the tip itself. The housing is made of a stainless steel cylinder, with three legs pointing upward and a three-pointed spring that holds the tip sheath (see Fig. 2.6). The sheath is just a small, hollow tube that holds the remaining half of the W wire from the etching process. Both are loaded onto a tip holding puck that is then loaded onto the STM sample stage. Once there, the scan head is lowered onto the housing, where the legs align with holes in the scan head, lining the scan head up to grab the tip sheath. Once completely lowered, the wire holding the tip sheath in the housing is disengaged and the scan head is raised, with the new tip installed. This procedure allows the making and installation of new tips without venting the STM chamber.

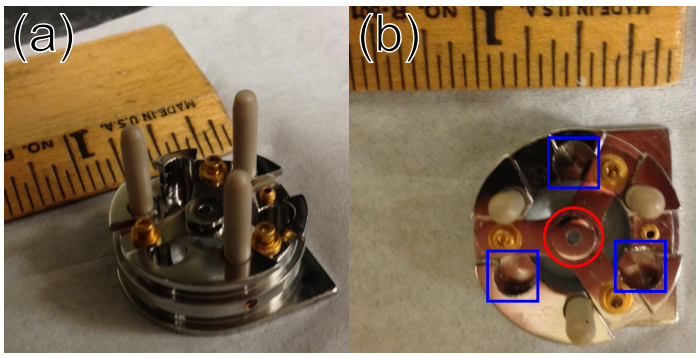

Figure 2.6. (a) STM tip holder for loading new tips. (b) Top view of the holder. The center hole that holds the tip sheath and W wire is circled. Squares indicate where the STM scan head legs go when changing tips.

2.4 Atomic Force Microscopy (AFM)

Other methods were used on the samples after they were removed from the vacuum chamber. AFM is a related technique to STM in that an atomically sharp probe is used to map the topography of the surface. While STM uses quantum tunneling between tip and surface states, AFM operates on the principle of atomic force repulsion. This was implemented in a Veeco Nanoscope-IIIA AFM which was used in all AFM images in this study. In this setup, an Si cantilever with an atomically sharp tip at the end of the cantilever oscillates near its resonance frequency at 200-300 kHz. Samples are mounted on magnetic disks using an adhesive, then loading the disk with the sample under the tip. A laser is shone on the top of the cantilever, which is coated with a reflective coating, causing the laser light to reflect into a photodetector.

As the cantilever oscillates, the laser reflection direction changes, which is measured by the photodetector. Far from the sample surface, the cantilever oscillates freely. As the tip approaches the surface, the tip atom on the bottom of the cantilever taps on the surface atoms. The atoms interact via electrostatic forces, producing a change in the oscillation of the cantilever and thus a change in the measured laser light in the photodetector. These signals are sent to the computer, from which quantities such as surface height, signal amplitude, and phase angle can be calculated. The

ability to track several quantities simultaneously is a major advantage for AFM. For the purposes of this work, though, larger-scale topography that could not be obtained through STM was sufficient.

2.5 X-ray Diffraction (XRD)

2.5.1 Theory

An XRD system consists of three basic parts: an x ray source, the sample, and the detector. The x-ray source consists of a filament and a target. The filament is resistively heated with an electrical current, causing electrons to be ejected from the filament into the target. Some of these electrons are slowed as they pass through the target, causing them to lose energy in the form of x ray emission, causing what is known as bremsstralung, or "braking radiation". Other incoming electrons will ionize the target by colliding with and ejecting core shell electrons in the target atoms, causing these atoms to become higher in energy. To lower the energy, valence electrons will fill the vacancy created, emitting the energy in the form of an x ray. Since the energy levels are quantized and discrete due to the quantum nature of the atom, the x rays emitted in this manner are consistent in energy and unique to that atomic species, and are thus called characteristic x rays. These x rays are used for XRD as the wavelength is largely constant. In either case, the x rays are allowed out through a narrow aperture, forming an x ray beam that is focused onto the sample, which reflect off the sample into the detector.

All XRD information is based upon the interaction of incident x rays with the sample's atomic lattice planes. Some x rays will diffract off the top-most plane, some off of the plane immediately next to that plane, and some off of the plane below that, and so on, up to a certain penetration depth. As x rays diffract off of the various lattice planes in the crystalline sample, the x-ray waves interfere with one

another, often producing destructive interference. For certain angles the waves will constructively interfere; these angles are known as Bragg angles and can be calculated according to the Bragg equation:

$$n\lambda = 2dsin\theta \tag{2.1}$$

where λ is the x-ray wavelength, n is an integer multiple of the x-ray wavelength, d is the lattice spacing, and θ is the Bragg angle. This equation states that for constructive interference to occur, the distance x rays diffracting off of planes deeper into the sample must be an integer number of wavelengths longer than the distance traveled by the x rays diffracting off of the top-most lattice plane. Whenever constructive interference occurs, the detector registers a peak in intensity. The lattice spacing d is a function of the Bragg angle, and thus the lattice constant can be determined from the peaks in intensity that arise as θ is changed. This is known as a rocking curve (see Fig. 2.7 for an example), in that the sample angle is "rocked" around the value of θ with the maximum x-ray intensity, which corresponds to the sample substrate.

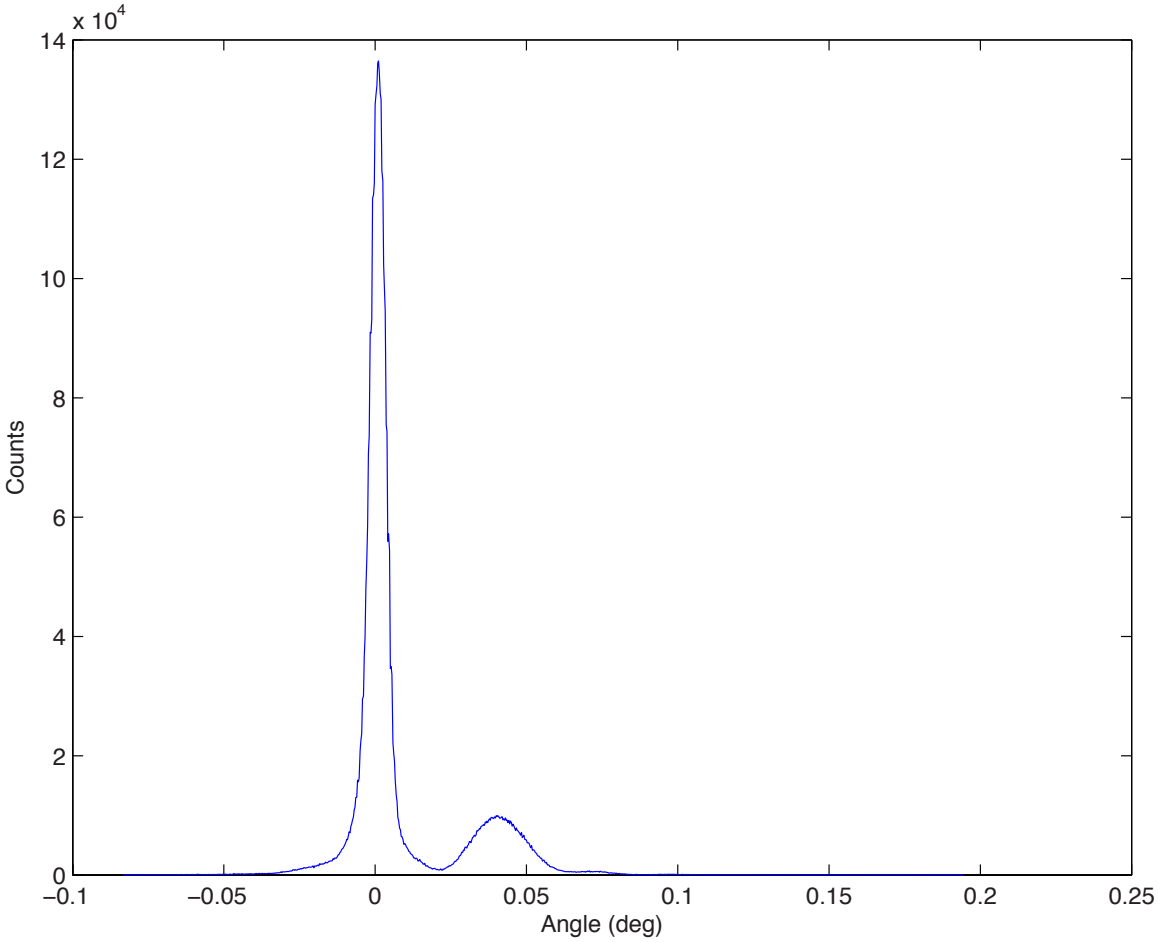

Figure 2.7. Example of an x ray rocking curve of a GaSb substrate (tall peak) with a GaSb buffer showing residual As incorporation (short peak).

Other peaks of lesser intensity correspond to films grown on top of the substrate. Depending on the composition and subsequent lattice constants of these films, the peaks will appear at higher or lower values of θ. According to Eq. 2.1, for fixed values of n and λ, d and θ are inversely related. For a film with a larger lattice constant (and thus larger value of d), than the substrate, θ of the peak for the film will be less than that of the substrate, and vice versa for films with smaller lattice constants. For layers of the same crystal structure as the substrate and assuming full film relaxation, film composition can be determined from the lattice spacing by averaging the lattice constants of the constituents in the ternary film according to the rule of mixtures equation:

$$a_{Film} = x\,(a_1) + (1 - x)\,(a_2) \tag{2.2}$$

where a_{Film}, a_1, and a_2 are the lattice constants of the film, constituent 1, and constituent 2, respectively, while x is the fraction of constituent 1 present in the film. Given a ternary film, say $GaAs_xSb_{1-x}$, the constituents would be GaAs and GaSb. In this case, x is the fraction of zinc-blende anion sites occupied with As.

Other useful information can be inferred from rocking curve film peaks. The full-width, half-maximum (FWHM) of a peak is a measure of film uniformity and quality. A low FWHM arises from little variation in the film lattice constant, which suggests a more uniform film. In contrast, a broader peak with a higher FWHM indicates the film is exhibiting constructive x-ray interference over a wider range of angles, which requires a variation in lattice spacing. This in turn is indicative of film relaxation through dislocation formation or composition homogeneity. As such, film strain and relaxation are related to film composition, making a determination of the effects of each difficult with XRD alone, but if the one is known, the other can be calculated using Eqns. 2.1 and 2.2.

2.5.2 Experimental Setup

All high resolution x ray diffraction (HRXRD) scans were performed using a Bede D1 HRXRD system. X rays were produced with a Cu target ($\lambda = 1.54$ Å) and filtered through two single crystal Si beam conditioners to monochromate and focus the x-ray beam. Samples were mounted by starting with the same method described above for AFM, then the magnetic disks subsequently mounted on a magnetic sample plate, which was then in turn loaded into the path of the x-ray beam. The ω and 2θ axes were set to the Bragg angles for the (004) and (224) diffraction planes.

After optimizing the axes in order to achieve maximum x-ray intensity in the detector at the Bragg angle, scans along the $\omega - 2\theta$ axis were taken. Such a scan is

analogous to a $\theta - 2\theta$ scan commonly used in powder diffraction, where the source and detector move by the same angle while the sample remains fixed. The same is accomplished in this setup by moving the sample (ω axis) and detector (2θ axis) while the x-ray source remains fixed. For these scans, a slit is placed between the detector and the sample to reduce the spread of x-ray energies allowed into the detector, increasing resolution of the peaks in the scan. After scanning, the Bede Peaksplit software was used to analyze the results and calculate the relaxation and composition of epitaxially grown films according to Eqs. 2.1 and 2.2.

2.6 Rutherford Backscatter Spectroscopy (RBS)

2.6.1 Theory

RBS operates on the principle of measuring energy losses of ions after having collided with the nuclei of the sample atoms. Like in a XRD setup, a RBS setup consists of a source, a sample, and a detector. The source emits ions of low mass (He^{++} in this work) that are collimated into a beam by magnetic focusing coils and are accelerated to energies in the $\sim$1 MeV range. An ion incident upon the surface is reflected back upon colliding with the nuclei in the sample, where the energy of the ion is measured via the detector. The amount of energy the ion loses in the process depends upon the mass ratio of the incident ion and the target atom. Collision with a heavy atom results in little energy loss, while collisions with lighter atoms will result in more ion energy loss. The number of ions counted with a given energy indicate how prevalent that species is in the sample. Such a method provides a non-destructive means of determining sample composition.

2.6.2 Experimental Setup

All RBS measurements were carried out at the University of Michigan Ion Beam Laboratory (MIBL) on a 1.7 MV Tandem Accelerator.[32] He^{++} ions with 2 MeV of energy were normally incident on the sample surface ($\alpha = 0°$) (see Fig. 2.8,[33] either reflecting off the surface at an angle of $\beta = 20°$ or scattering into the sample at an angle of $\theta = 160°$. The reflected ion energies were measured with a detector, from which the spectra could be reproduced using a computer. Reference targets of Au and Si were used to calibrate the system. In order to obtain the compositions of the samples, the simulation software SimNRA was used to fit samples of various compositions to the data.[33, 34]

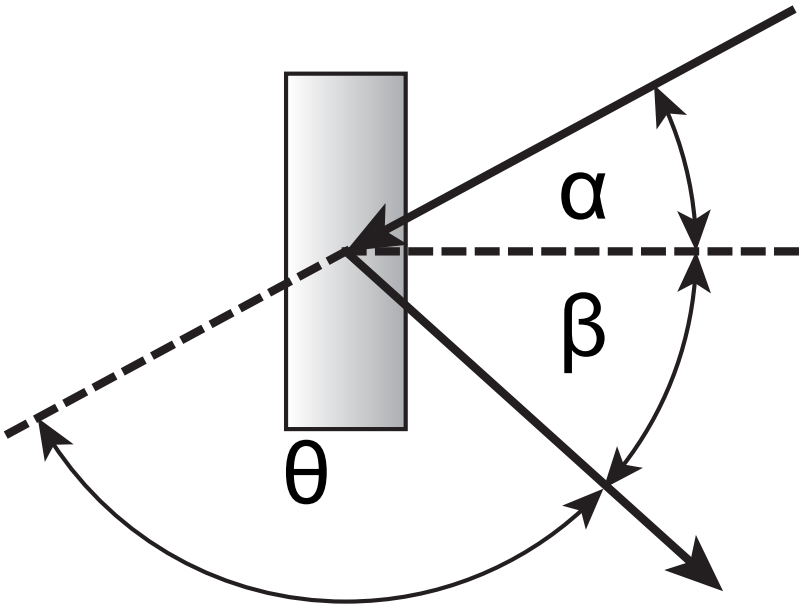

Figure 2.8. Geometry of the incident He^{++} ions after impinging on the sample surface. α is the incident angle, β is the angle of reflection (also known as the exit angle), and θ is the scattering angle with which the ions enter the sample.

2.7 Scanning Electron Microscopy (SEM)

SEM operates consists of a focused beam of electrons accelerated to 5-20 kV to scanned across the surface of a sample. The electrons are generated from an electron

gun, which comprises the electron beam, which then pass through a series of magnetic focusing lenses that focus and raster the beam across the surface. Some electrons in the beam eject electrons out of the sample, producing what is known as secondary electrons. These can be detected and are used for obtaining surface topography and features. If an incident electron causes a core shell electron to be ejected, higher orbital electrons will take the place of the ejected electron, emitting an x ray in the process. Since the energy levels in each element are quantized, the x-ray energies are very specific and can be used to characterize the sample composition, a technique known as energy-dispersive spectroscopy (EDS). Finally, other electrons in the beam will instead reflect off of the sample surface, which can be collected by a backscatter detector, providing information on chemical composition.

All SEM work was carried out on a FEI Nova Nanolab 200 combined focused ion beam and SEM system equipped with a field emission gun for high resolution imaging and an EDS detector for composition mapping. Secondary images were taken using a through-the-lens detector (TLD) at 10-15 kV at 0.15-0.19 nA of beam current. These settings were chosen in order to keep the electron energy low enough to obtain high enough resolution while simultaneously having enough energy to eject core shell electrons for EDS mapping of the surface.

2.8 Simulation Methods

In addition to the experimental techniques outlined above, several simulation techniques were employed. Among these are DFT, the cluster expansion formalism, and statistical Monte Carlo (sMC). These methods were used to augment the observations obtained through STM in order to more clearly determine the atomic structure and composition of the surface reconstructions, as these fine details are not easily obtainable by experimental means. Moreover, these methods also provide a means of calculating relative stabilities of the surface reconstructions.

2.8.1 Density Functional Theory (DFT)

DFT is a method for reducing the complex calculations of atomic interactions into a more tractable problem. The interactions between each electron in every atom is computationally intensive, limiting the size of the systems that can be simulated. DFT approximates the groundstate energy of a given system by calculating three separate components according to the Kohn-Sham equation:[35]

$$E = KE + V_{ext} + E_{ee} + E_{xc} \tag{2.3}$$

where KE is the kinetic energy of the system, V_{ext} is the external potential an electron experiences, E_{ee} is the classical electron-electron interaction energy, and E_{xc} is the exchange-correlation term. E_{xc} encompasses the energy of two electrons exchanging positions and the correlation of motion of one electron with respect to another, capturing the quantum mechanical behavior to an extent, but in general is not known exactly and thus must be approximated.

DFT is based on the Hohenberg-Kohn theorems which state that the groundstate energy and potentials are determined by the electron density $n(r)$.[36] Calculations are performed in a self consistent manner. Starting with a given set of atom positions, a trial wavefunction can be calculated, from which the electron density is determined. Then the energy is calculated according to the Kohn-Sham equation. Depending on the energy, the atoms in the system can be moved to lower the energy, producing a new wavefunction, from which the electron density and energy is calculated. This cycle is repeated for all the atoms in the system until all the atoms are in their equilibrium positions and the system is considered relaxed into the lowest energy groundstate.

All DFT calculations in this work were performed using the Vienna *ab-initio* Simulation Package (VASP) using the local density approximation (LDA) to the exchange-correlation.[37] All calculations were performed on the Red Sky supercomputing sys-

tem at Sandia National Laboratories.

In this work, all DFT calculations were of surface reconstructions. Since DFT uses periodic boundary conditions, simply creating a semi-infinite system is impossible; the system would be infinitely large in the surface normal direction. Instead, simulating surfaces in DFT requires the use of slabs, that is layers of atoms with the same crystal structure as the bulk, separated by a vacuum layer. After constructing a finite number of layers, the reconstruction is placed on the top surface of the slab. The bottom surface dangling bonds were passivated with pseudo-H atoms, a fictitious species with a non-physical charge of 0.75 that satisfies the bonding for the bottom surface anions. Thus, the bottom surface becomes charge neutral and does not introduce any artifacts into the energy.

2.8.2 Cluster Expansion

The energies of the reconstructed surfaces studied in this work were influenced by two kinds of configuration: structural and compositional. The structural configuration refers to the atomic structure and arrangement, while the compositional configuration refers to different occupancies of species of the sites defined by the structural configuration. As such, structural configuration has about an order of magnitude larger effect (~ 100 meV$/(1 \times 1)$ unit area) on the surface energy than compositional configuration (~ 10 meV$/(1 \times 1)$ unit area).[38] Also, each structure can contain up to several thousand different potential different compositional configurations.

In theory, each one of these configurations could be simulated using the DFT slab method outlined above and the energies compared to obtain the groundstate configurations. In reality, this is computationally impractical to do. An alternative to this is to use the cluster expansion formalism,[39] a method that isolates the governing behavior and underlying correlations to predict the energies of any compositional configuration using only a subset of all possible configurations. Since this assumes

a particular structure (in this case a particular reconstruction), a cluster expansion must be constructed for each structural configuration. Once the groundstate energies for each reconstruction are determined, these energies are compared to determine the regions of stability between reconstructions and stability of each compositional configuration within each reconstruction.

In this work, the Cluster Assisted Statistical Mechanics (CASM) code was used to carry out the cluster expansions.[40] Given a set of sites that are allowed to vary in occupation, the program finds all clusters, that is all pairs, triplets, quadruplets, etc. of sites, up to a specified cutoff distance. Each cluster has an effective cluster interaction (ECI), which is a measure of how correlated the occupancy of a particular species on a particular site affects the occupancy of other sites in the cluster. A high ECI indicates a particular occupancy in all the sites in a that cluster is energetically favorable. If all the important ECI are known, then the energy for any configuration can be predicted.

Obtaining the ECI is an iterative process:

1. The relaxation energies of a small subset of configurations is calculated using DFT.

2. The energies are put into a genetic fitting algorithm that determines each ECI and construct the set of ECI that minimize the cross-validation (CV) score.[41]

3. With the ECI, the new groundstates are predicted, which can then be calculated with DFT.

4. The process repeats until no new groundstates are predicted.

With the groundstate energies calculated, the energies of all the groundstates for each reconstruction are compared as a function of chemical potential. Doing so produces a phase diagram of the stability of surface reconstructions and the various

compositions relative to one another. The details of this process will be discussed more in Ch. IV.

2.8.3 Statistical Monte Carlo (sMC)

While the DFT and cluster expansion methods provide a wealth of information on stability of the surface reconstructions, these calculations do not account for thermal atomic vibrations, that is for the system at 0 K. In order to simulate some of the effects of temperature, including compositional disorder, a sMC method was used as implemented in the CASM code. For these surface studies, chemical potential μ and temperature T are the control variables.

When run, the simulation starts at a given (μ, T) and constructs a supercell (16×16 in this work) of a specific reconstruction configuration (such as the all-As configuration) as a starting point. The simulation then proceeds from this point in steps, where the sites are visited at random and a species occupancy change considered. The ECIs calculated from the cluster expansion fits are used in the Metropolis algorithm to predict the energy of the change in occupancy.[42] According to the algorithm, if an occupancy change results in a lower predicted energy, the change is always accepted. On the other hand, if the predicted energy is higher, it is accepted with a certain probability in order to avoid local energy minima to find the global energy minimum.

Enough steps (5000 in this work) must be done before the residual effects of the starting surface are eliminated. After this, the system is considered to be in equilibrium; for each subsequent step, the thermodynamic quantities are recorded, including energy and average surface composition. After a given number of steps (5000 in this work, for 10000 steps total), the average of these quantities is recorded. Once this done, the simulation proceeds to the next set of (μ, T) and repeats the process of equilibrating the surface under the new conditions and then calculating the

thermodynamic averages. Other quantities such as entropy S and order parameters can be derived from this data, which in turn are useful measures of surface order.

CHAPTER III

Bi-terminated GaAs Surfaces

3.1 Introduction

Understanding the effect of Bi on atomic surface structure is crucial to predicting film growth behavior. Evidence exists that incorporated Bi atoms form clusters in bulk GaAsBi, as confirmed by extended x-ray absorption fine spectra, [43] photoluminescence measurements,[4] and aberration-corrected scanning transmission electron microscopy.[44] Since bulk diffusion is slow, these clusters likely nucleate at the surface during growth; therefore, understanding how Bi alters the surface structure and morphology will lead to an understanding of the growth of Bi-containing materials.

Some progress already exists in this area. Laukkanen et al. has studied Bi deposition onto III-V alloy surfaces (primarily GaAs and InP) at room temperature using W-coil evaporation, Bi-induced (2×1) and $\beta 2\,(2 \times 4)$ reconstructions were observed using low-energy electron diffraction (LEED), STM, scanning tunneling spectroscopy (STS), and photoelectron spectroscopy.[45, 19, 46, 47, 48, 49, 20] They showed the GaAs and InP (2×1) reconstructions are a combination of metallic (Bi-Bi dimer) and semiconducting (2×1) (Bi-As or Bi-P dimer) unit cells, while the $\beta 2\,(2 \times 4)$ reconstructed surface is also a mixture of homodimer and heterodimer terminated $\beta 2\,(2 \times 4)$ unit cells. The stability of these particular reconstructions have also been supported by previous density functional theory simulations.[50, 51]

In contrast, the structural details of the reconstructions obtained under Bi deposition under MBE conditions have received little attention. Bi deposition onto the GaAs(001) surface at 500-520°C produced a $(n \times 3)$ surface, where $n = 1\text{or}2$ according to reflection high energy electron diffraction.[52, 53] Another study by Masnadi-Shirazi et al. produced a RHEED phase diagram for GaAsBi, where similar $(n \times 3)$ surface periodicities were observed.[23] However, despite these investigations, the details of the surface reconstruction are unknown. The appearance of several $\times 3$ periodicities suggests a (4×3) reconstruction, which will be discussed later. This chapter details the experimental studies to more fully determine the atomic structure of the $(n \times 3)$ surfaces. This work represents the first STM studies of the $(n \times 3)$ surface structure to be carried out, providing valuable information on the surface at the 1 nm length scale (NLS), while AFM studies at the 1 μm length scale (MLS) showed the surface smoothing effect observed elsewhere.[52, 53, 54] Based on the observations in this chapter, a mechanism is proposed for this behavior and suggests future work to be addressed in order to verify this.

3.2 Experimental Setup

The Bi-terminated GaAs films were grown in the MBE setup described in Ch. II. The Ga beam equivalent pressure (BEP) was measured as 3×10^{-7} torr, while the As_4 BEP was 5×10^{-6} torr, which corresponds to 2.4 monolayers per second (ML/s) according to RHEED oscillations for As-limited growth. The Bi BEP was measured as 1.5×10^{-7} torr, but since GaBi alloy cannot be grown, the growth rates were not measurable by RHEED oscillations. As a substitute, the growth rate can be approximated according to desorption of Bi after deposition onto GaAs(001) surface,[53] which gives a growth rate of ~ 0.2 ML/s.

Samples were produced according to the following recipe. First, the GaAs n+ substrate was desorbed at 620°C, then a 500 nm GaAs buffer layer was grown at about

585°C at a Ga-limited rate of 0.66 ML/s. Two different series of samples branch out from this point. The first is the study of Bi deposition on the $\beta 2\,(2\times 4)$ reconstruction, the second the same deposition on the $c\,(4\times 4)$ reconstruction. For the $\beta 2\,(2\times 4)$ starting surface, after growing the buffer layer, the As flux was stopped, then the substrate cooled in order to prevent the $\beta 2\,(2\times 4)\rightarrow c\,(4\times 4)$ reconstruction. Bi was deposited at substrate temperatures of $390°C \leq T \leq 440°C$ and As_4/Bi flux ratios of $0 \leq As_4/Bi \leq 0.2$. For the $c\,(4\times 4)$ starting surface, the As flux remained on while cooling the sample to $440°C$, then annealed for 30 minutes (30 min) under a low As_4 overpressure to remove excess surface As atoms while maintaining the $c\,(4\times 4)$ surface. The As_4 flux was discontinued before depositing 0.6 ML of Bi. In both series, after deposition was complete, each sample was quenched to $200°C$ under no overpressure in order to preserve the Bi-terminated surface. After in vacuo transfer to the STM chamber, STM images were taken in constant current mode, where tunneling voltages ranged from -2.50V to -6.00V and tunneling currents were 0.1-0.16 nA.

3.3 Results

3.3.1 $\beta 2\,(2\times 4)$ Series

The RHEED pattern in Fig. 3.1(a-b) are typical of the starting $\beta 2\,(2\times 4)$ GaAs surface prior to Bi deposition. Quenching the sample and imaging with STM as shown in Fig. 3.1(c) reveals a typical $\beta 2\,(2\times 4)$ surface reconstruction, with ordered, straight rows and large flat terraces.

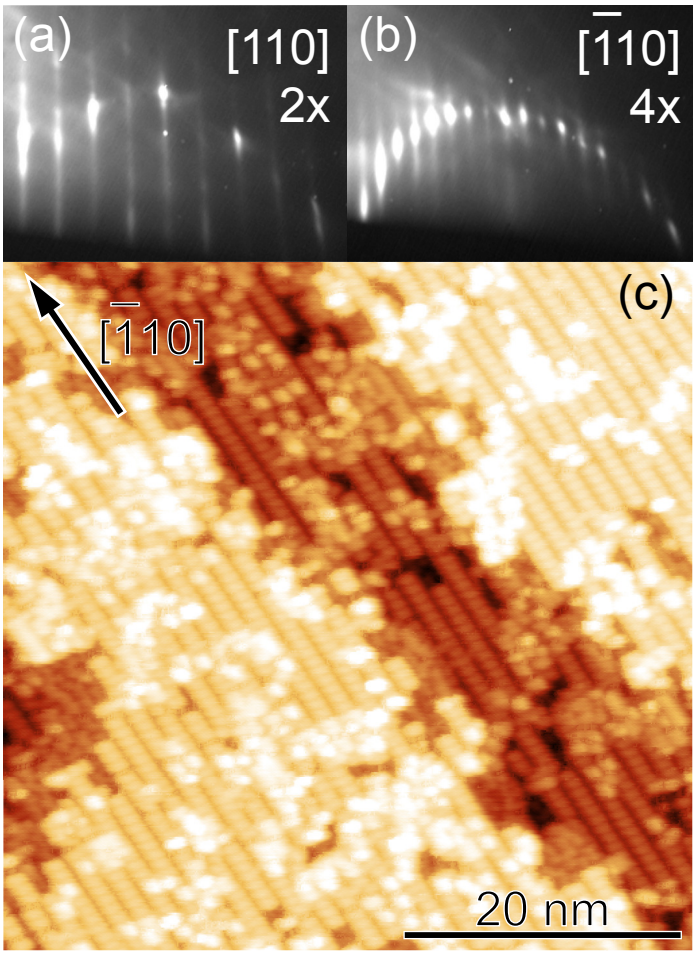

Figure 3.1. (a-b) RHEED patterns and (c) STM (-3.00 V, 0.1 nA) of the Bi-terminated surfaces of the $\beta 2\,(2 \times 4)$ surface prior to Bi deposition.

In another sample Bi was deposited onto the surface in 1 second (1 s) increments up to a total of 7 s at a substrate temperature of 390°C. A number of Bi-induced surface transformations occurred during this process, as seen in the sequence of RHEED images in Fig. 3.2. After depositing Bi for 1 s (≈0.2 ML), the (2×4) pattern (Fig. 3.2(a-b)) is unchanged. A total of 4 s of Bi deposition (≈0.8 ML total) results in the rather fuzzy (2×3) pattern of Fig. 3.2(c-d) indicating a surface transformation has taken place but has not yet completed. Adding yet more Bi, up to 7 s total (≈1.4 ML) results in the (1×3) pattern of Fig. 3.2(e-f). The 1/2 non-principle streak has disappeared in Fig. 3.2e, while the non-principle streaks of the [$\bar{1}$10] zone

axis in Fig. 3.2f is much better defined. One possible explanation for the (2×3) RHEED pattern is it is a distinct reconstruction. Another possibility is suggested by Romanyuk et al. for the (4×3) reconstruction in GaSb.[55] In that work, it was demonstrated with structure factor calculations that shifting of the rows with respect to one another can produce either a (2×3) or (1×3) RHEED pattern depending on the amount of shifting. Thus, one reconstruction could produce both $\times 3$ patterns. A third explanation is the (2×3) pattern represents a mixed reconstruction of $\beta 2\,(2 \times 4)$ rows and the (1×3) reconstruction.

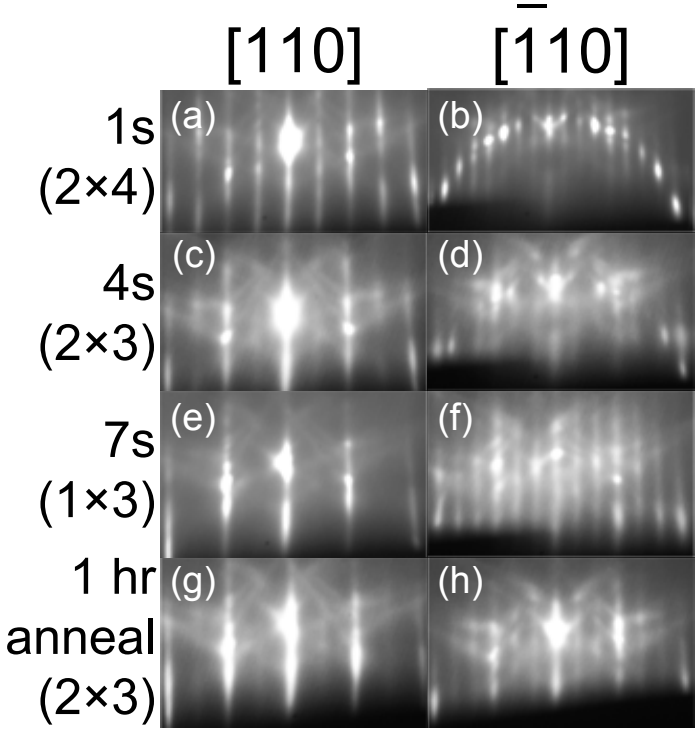

Figure 3.2. RHEED patterns of the GaAs surface after Bi deposition times of (a-b) 1 s, (c-d) 4 s, (e-f) 7 s, and (g-h) 7 s + 1hr annealing.

In order to test these explanations, another sample was annealed for 1 hour after 7 s of Bi deposition to allow for some Bi desorption to occur. In Fig. 3.2g the 1/2 non-principle streaks have returned and the $\times 3$ non-principle streaks have dimmed somewhat in Fig. 3.2h. Having recovered the (2×3) surface to an extent, the sample was quenched and the surface imaged with STM as shown in Fig. 3.3. The surface is

largely dominated by a disordered row reconstruction with individual $\beta 2\,(2 \times 4)$ rows about 3-4 $\beta 2\,(2 \times 4)$ units long interspersed throughout the steps, some of which are circled in Fig. 3.3. Thus, the $2\times$ periodicity measured in Fig. 3.2c cannot originate from a distinct (2×3) reconstruction; the individual reconstruction units are too irregular within each row to produce any periodicity. The appearance of these two reconstructions corroborates the third hypothesis suggesting the (2×3) RHEED pattern of Fig. 3.2(c-d) is a mixture of the $\beta 2\,(2 \times 4)$ and (1×3) reconstructions, although the row shifting explanation could also at least partly contribute to the observed periodicity. It is not possible to isolate these effects with a single sample. However, STM imaging of other samples with (2×3) surfaces consistently show the $\beta 2\,(2 \times 4)$ reconstruction rows appear in tandem with the (2×3) RHEED pattern. Therefore, the mixed surface is likely the primary reason for the (2×3) RHEED pattern.

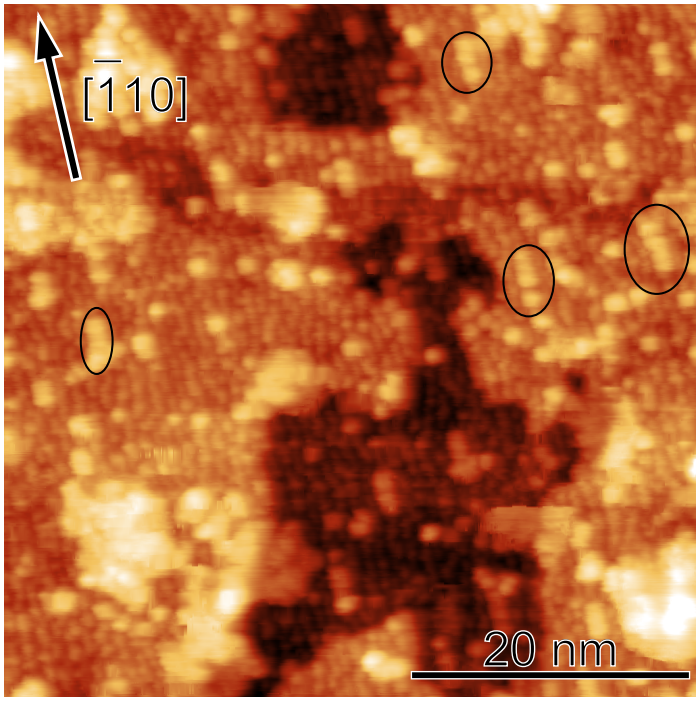

Figure 3.3. STM (-2.50 V, 0.1 nA) of the final (2×3) surface obtained after 7 s of Bi deposition and subsequent 1hr annealing. The surface is comprised mostly of a disordered row reconstruction with individual $\beta 2\,(2 \times 4)$ rows circled in black.

After depositing Bi for 12 s (≈2.4 ML), a (1×3) pattern appeared as seen in Fig. 3.4(a-b). The underlying change in surface reconstruction periodicity is verified in Fig. 3.4(c), where STM reveals the same disordered row reconstruction as seen in Fig. 3.3. The average spacing along the [110] is 1.2 ± 0.1 nm, or 2.9 ± 0.2 times the GaAs surface lattice parameter, corroborating the observed $\times 3$ periodicity in the [110]. As in Fig. 3.3, there are no regular features along the rows parallel to the $[\bar{1}10]$, leaving only the bulk GaAs principle $1\times$ streaks along in Fig. 3.4(a). Hence, the (1×3) RHEED pattern indicates a heavily disordered surface.

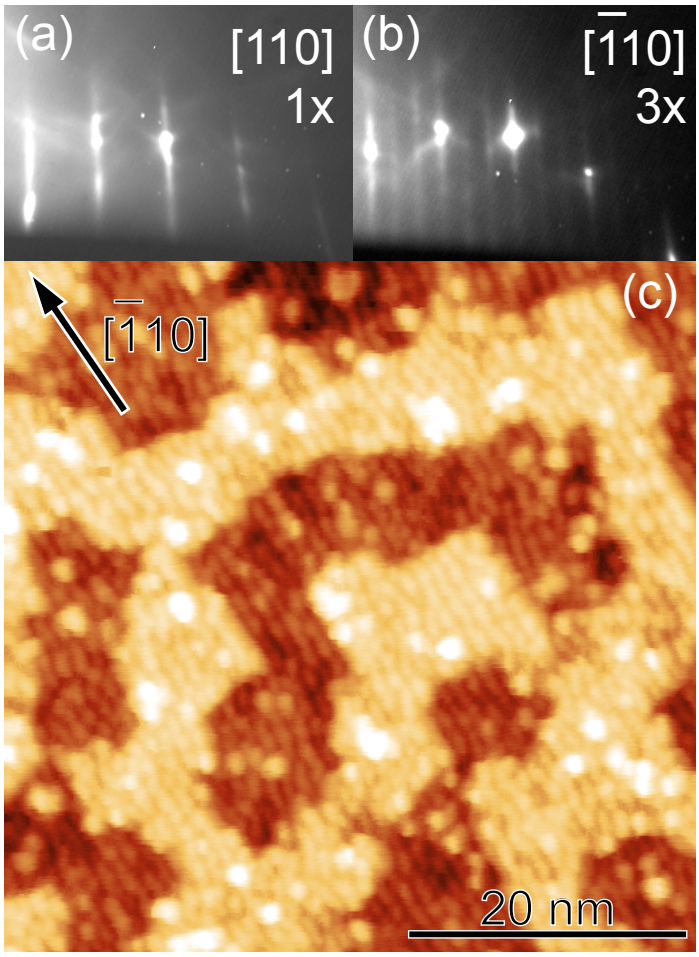

Figure 3.4. (a-b) RHEED and (c) STM (-3.00 V, 0.1 nA) of the Bi-terminated surface after 12 s (or ≈2.4 ML) of Bi deposition.

However, a more ordered surface was produced at 400°C after depositing 30 s (≈6 ML) of Bi under an overpressure As_4/Bi ratio of 0.2. The resulting RHEED

patterns in Figs. 5(a-b) show a (4×3) surface periodicity, indicating an enhancement in ordering compared to the Bi-only sample. STM of this surface after quenching (Fig. 3.5(f)) reveals the same reconstruction as seen in Fig. 3.5(c). That is, there is strong short- and long- range order with a periodicity of 1.2 nm ($3a_0$) along the [110] direction, with some short-range but no measurable long-range order along the $[\bar{1}10]$. Hence, the RHEED pattern has only faint non-principle streaks in Fig. 3.5(a) as the $4\times$ periodicity is only over short distances. The observation via STM of the same reconstruction for both (1×3) and (4×3) RHEED patterns suggests the (4×3) reconstruction is the primitive unit cell present on both surfaces. At this point, it is clear this new row reconstruction has a consistent $3a_0$ spacing between the rows but no consistent spacing between units with the rows for the observed surfaces. Hence, the disordered row reconstruction will be referred to as the $(n \times 3)$ reconstruction, where $n = 1, 2, \text{or } 4$.

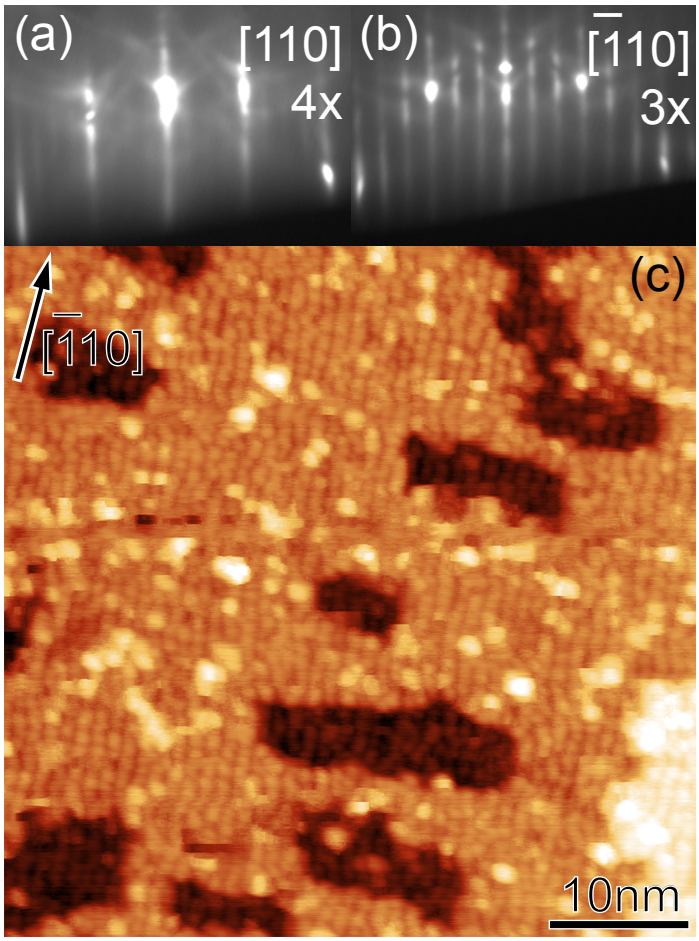

Figure 3.5. (a) 4× and (c) ×3 RHEED patterns indicating a more ordered surface reconstruction after depositing 6 ML of Bi with $Bi/As_4 = 5/1$. (c) STM (V=-6.00 V, I = 0.16 nA) shows the same reconstruction as Fig. (c).

3.3.2 $c(4 \times 4)$ Series

In the second series of samples where Bi was deposited onto the $c(4 \times 4)$ surface, the RHEED patterns and STM corresponding to the starting surface are shown in Fig. 3.6. After annealing for 30 min at 416°C under a small As_4 flux the $c(4 \times 4)\alpha$ reconstruction is obtained. This reconstruction is a variant of the $c(4 \times 4)$ reconstruction that appears under As_4 flux and consists of Ga-As heterodimers as reviewed by Ohtake.[27]

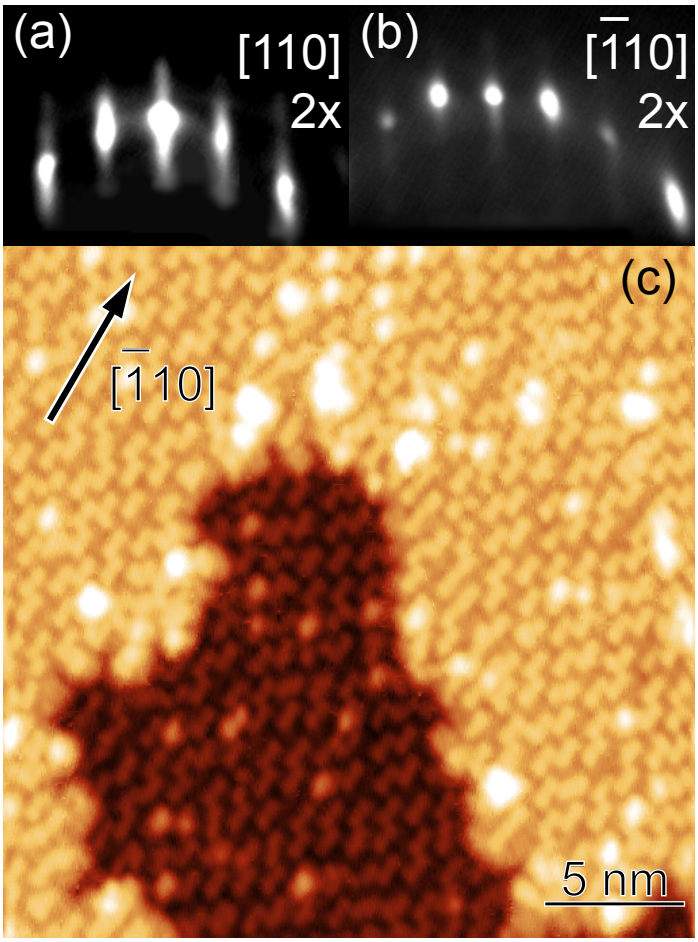

Figure 3.6. RHEED patterns (a-b) and STM (-2.50 V, 0.1 nA) (c) of the GaAs $c\,(4\times4)\,\alpha$ surface after annealing at 416°C for 30 min.

Depositing 3 s of Bi (≈0.6 ML) onto the $c\,(4\times4)\,\alpha$ surface produces the (2×3) RHEED pattern and surface reconstruction seen in Fig. 3.7. As with the (2×3) surface observed in Fig. 3.3, the disordered row reconstruction and $\beta2\,(2\times4)$ reconstruction rows are both present. This reinforces the explanation that the (2×3) RHEED pattern appears from the mixed reconstruction. This also suggests that the $(n\times3)$ reconstruction exists in the more Bi-rich region of phase space above the somewhat As-rich $\beta2\,(2\times4)$ reconstruction and the very As-rich $c\,(4\times4)\,\alpha$ reconstruction. This provides some insight on the $(n\times3)$ reconstruction, that it is stable over a rather wide range of As chemical potential. This will be investigated further in Ch. IV.

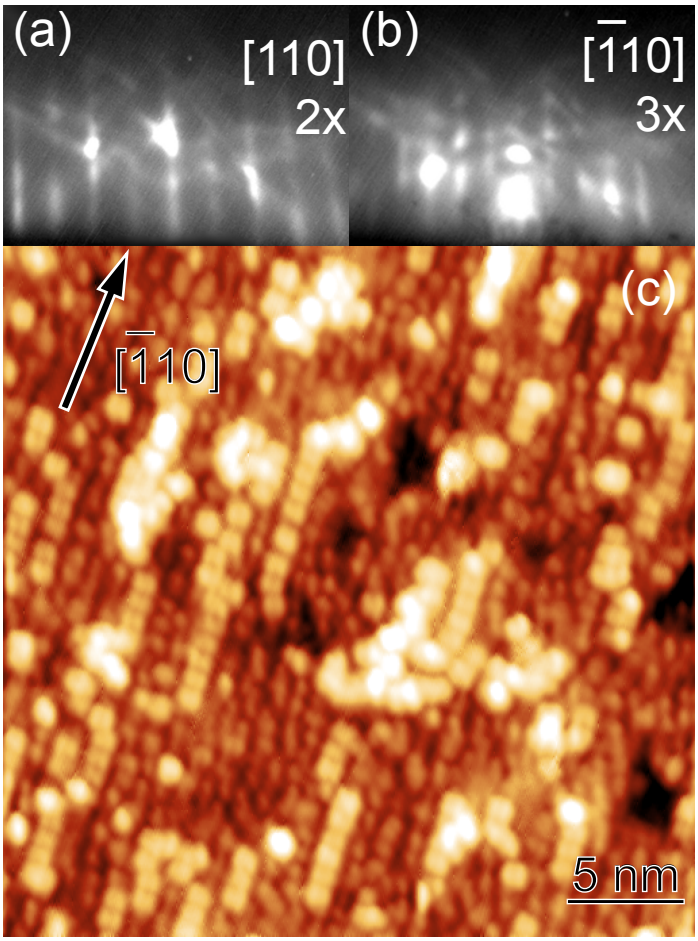

Figure 3.7. RHEED (a-b) and STM (-2.50 V, 0.1 nA) (c) after $\approx$ 0.6 ML of Bi deposition onto the $c\,(4 \times 4)\,\alpha$ surface.

3.4 Step Morphology

The step morphology on the 1μm length scale in both growth series also changed considerably after Bi deposition, consistent with other work on GaAs, InGaAs, GaAsN, InGaAsN, and GaAsBi.[52, 53, 54, 56, 57, 18] In all those studies, surfaces as imaged by AFM were all smoother with Bi deposition than without, regardless of the underlying substrate. Bi is the largest group V element, making it unfavorable to incorporate into all III-V films, but instead segregates to the surface; hence, Bi is a good surfactant for all III-V semiconductor film growth. Despite the observation of this smoothing effect, the mechanism for smoothing is unknown. To that end,

several 2×2 μm^2 AFM images were taken of the Bi-terminated sample surfaces to complement the 50×50 nm^2 STM images of the same surfaces. Several changes to the step morphology were observed on both length scales, providing some insight as to the reason for the smoothing effect.

The 50×50 nm^2 STM image shown in Fig. 3.8(a) of the bare GaAs surface shows large, flat terraces with relatively straight step edges. This is typical for layer-by-layer growth of GaAs. The corresponding 2×2 μm^2 AFM image (Fig. 3.8(b)) shows a rather rough surface, with series of several steps of like direction (either up or down) in series. After depositing 6 s ($\approx$ 2 ML) of Bi, the surface images seen in Fig. 3.8(c-d) show the roughness in the STM image has increased, while the roughness in the AFM one has decreased. Many more step edges and islands are seen in the STM of Fig. 3.8(c), with many unlike steps of opposite direction appearing together. The terraces of Fig. 3.8(d) are much larger and fewer in number than for bare GaAs. After Bi deposition, the large terraces of the bare GaAs give way to smaller terraces with meandering step edges having an average width (as measured by the correlation length) of 71 nm.

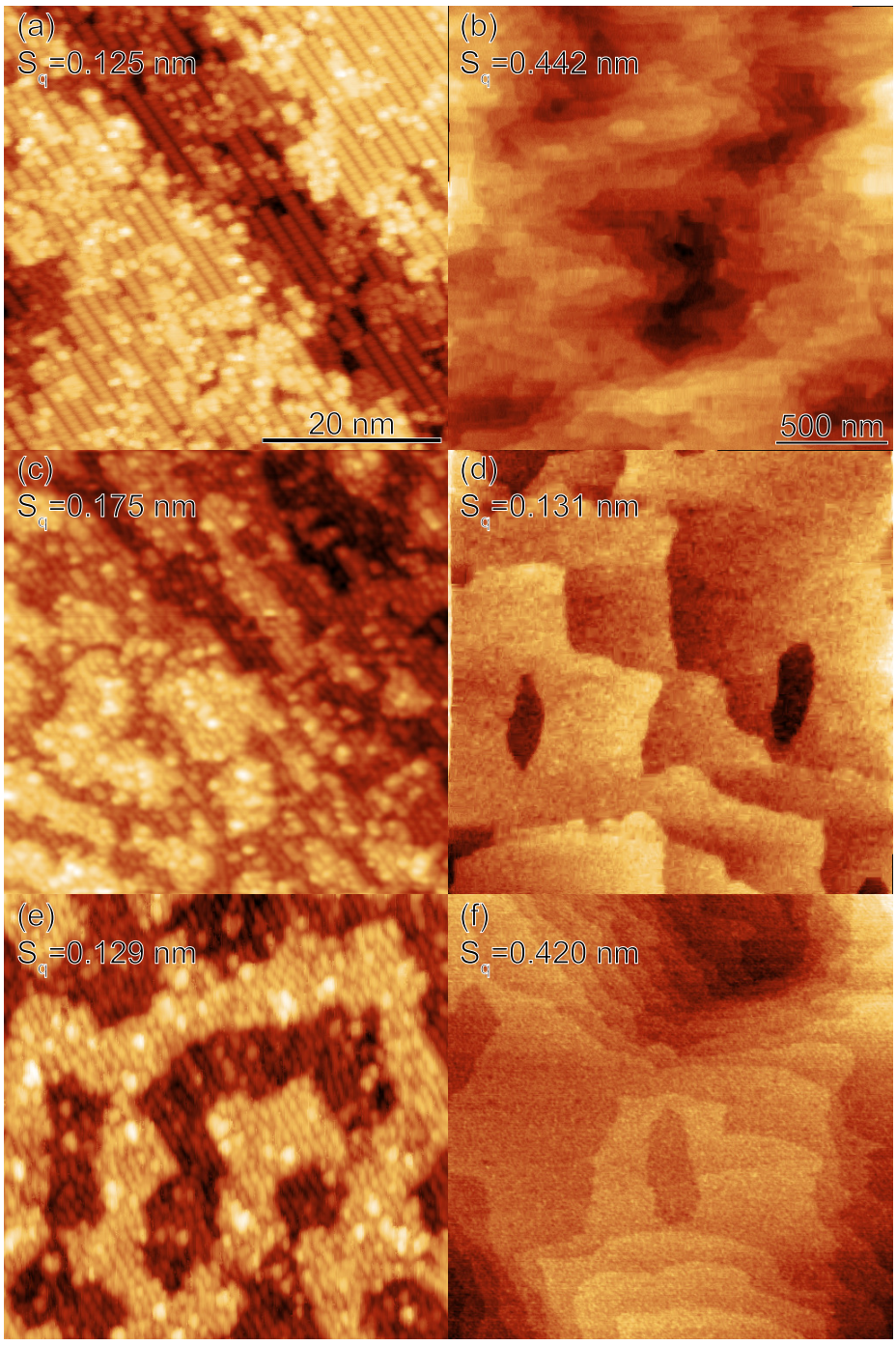

Figure 3.8. Left side: 50×50 nm^2 STM images of (a) bare GaAs, (c) 6 s (≈ 1.2ML) of Bi on GaAs, and (e) (≈ 2.4ML) of Bi on GaAs. Right side: 2×2 μm^2 AFM images (b,d, and f) that correspond to the STM of (a,c, and e), respectively.

These progressions in roughness suggests that adding Bi changes step-edge energies and interactions between step edges to favor the formation of narrowly spaced

ascending-descending step-edge pairs. The refined morphology slightly increases roughness on the NLS, with a RMS roughness increasing from 0.12 nm for the bare GaAs to 0.13 nm for the Bi-terminated GaAs over a 50×50 nm^2 area. This increase in short-scale roughness leads to a reduction in RMS roughness S_q at larger scales. Fig. 3.8(b) has a measured S_q of 0.440 nm, which upon Bi deposition decreases to 0.131 nm and 0.420 nm in Fig. 3.8(d) and (f), respectively. The increase in step density at the 10-nm scale has not been previously reported owing to limits on AFM resolution. It is also worth noting that although there are some step trains in Fig. 3.8(f), the smoothing mechanism is still observed in the large terraces. The step trains are a remnant of the bare GaAs surface grown prior to Bi deposition, which causes the ascending steps to congregate together. It is likely that growing a GaAs layer with a concurrent Bi flux will eliminate these step trains.

Bi incorporation into the GaAs surface reconstruction likely causes an increase in lateral strain owing to the large size of the Bi atoms. In order to alleviate this, the larger Bi atoms may sit on the upper terraces at step edges, allowing greater strain relaxation of the upper terrace out over the lower terraces. Moreover, Bi would tend to segregate away from the center of larger terraces, where Bi-induced strain relaxation is inhibited. Accordingly, Bi atoms will segregate away from the troughs and step centers to the step edges, producing a non-uniform Bi composition and encouraging step edge formation. This variation is similar to morphology-induced lateral composition modulation observed in InGaAs,[58] and may explain the formation of Bi clusters observed in other work.[44] During the growth of a GaAsBi alloy, it is possible that there is an excess of Bi on the surface, producing a surface morphology similar to the ones presented here. As growth continues, the large concentration of Bi atoms at the step edges could incorporate into the lattice, giving rise to the observed clustering.

This proposed model of why step edge density increases at the NLS also explains

why the same density decreases at the MLS. A side-view model of the change in MLS is shown in Fig. 3.9. In the bare GaAs case (Fig. 3.9(a)), the step edge energies are such that formation of adjacent like steps on the NLS is energetically favorable. This in turn results in step trains that form the large mountains seen in the MLS. Conversely, in the Bi-terminated surface shown in Fig. 3.9(b), the favorability of dissimilar steps on the NLS in turn discourages the step trains and mounds over the MLS.

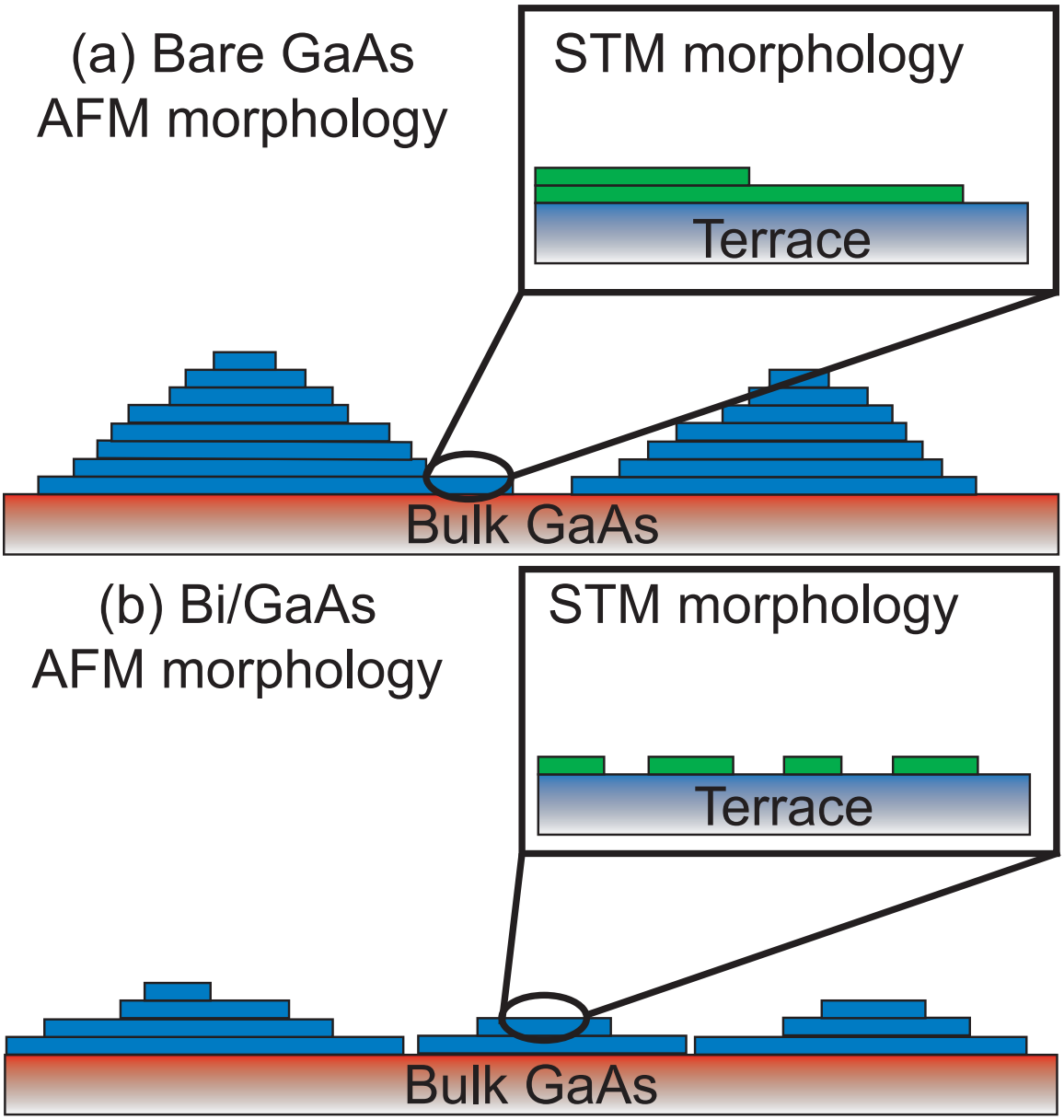

Figure 3.9. Side view of the MLS of the (a) bare GaAs surface and (b) the Bi-terminated GaAs surface. Insets show the corresponding side views of the NLS for each.

3.5 Proposed $(n \times 3)$ reconstruction model

The appearance of a $(n \times 3)$ surface periodicity on Bi-terminated GaAs(001) over a wide variety of conditions at the surface is somewhat unusual. A (2×3) periodicity was observed by Chizhov et al. after slowly reheating a $c\,(4 \times 4)$ reconstruction from 250°C to 350°C.[59] In that work, STM images of the GaAs surfaces suggested a

(4×3) reconstruction caused the observed (2×3) RHEED periodicity. And yet, all of the proposed $(n \times 3)$ structural models are thermodynamically unstable on pure GaAs(001) according to DFT.[60] Nonetheless, a systematic DFT study by Thomas et al. identified a class of (4×3) reconstructions on GaAs (001) that is only ≈25 meV higher in energy than the stable $\beta 2\,(2 \times 4)$ and $c\,(4 \times 4)$ reconstructions over a wide range of As chemical potential.[60] Hence, it is possible the $(n \times 3)$ reconstruction observed in Bi-terminated GaAs is in fact a disordered (4×3) reconstruction, causing several periodicities to appear in the RHEED measurements.

The structural model for this (4×3) reconstruction class, shown in Fig. 3.10(a), was originally proposed by Barvosa-Carter et al. for the GaSb surface. It consists of a chain of dimers along $[\bar{1}10]$, with a kink every fourth dimer, and a trench dimer (outlined in red in Fig. 3.10) perpendicular to the dimer chain.[61] Note the (4×3) reconstruction possesses a double anion layer like the $c\,(4 \times 4)$ reconstruction, where the top level dimers are bonded to anions and not cations underneath them.

The species occupation at each dimer site of the (4×3) is not fixed, producing a range of stable compositions. Three of these configurations tend to be particularly low in energy. The $\alpha\,(4 \times 3)$ (Fig. 3.10(b)) has all III-V heterodimers in the top level with a V-V trench dimer. The $\beta\,(4 \times 3)$ (Fig. 3.10(c)) has a single III-V heterodimer at the kink dimer position, while the $h0\,(4 \times 3)$ (Fig. 3.10(d)) consists entirely of V-V homodimers. The presence of several configurations of this (4×3) reconstruction no more than 25 meV in energy above the $c\,(4 \times 4)$ reconstruction on GaAs suggests that Bi could stabilize the (4×3) reconstruction via substitution at group-V dimer sites.[60]

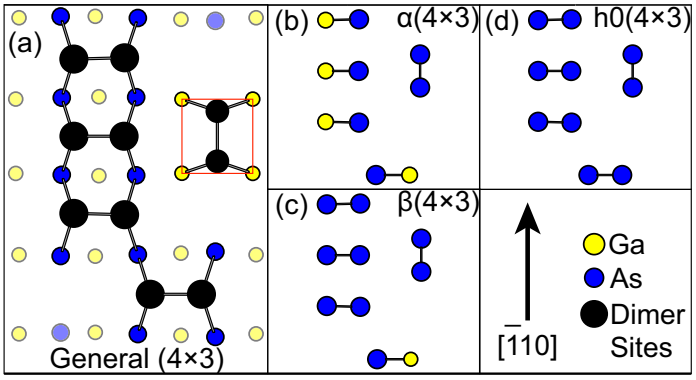

Figure 3.10. Model of the (a) general (4×3) reconstruction proposed for the $(n \times 3)$ reconstruction. The black dimer sites are allowed to vary in species occupancy and the red box is drawn around the trench dimer. The three most common variants of the (4×3) reconstruction are the (b) $\alpha\,(4 \times 3)$, (c) $\beta\,(4 \times 3)$, and $h0\,(4 \times 3)$ reconstructions.

For the Bi-terminated GaAs system, the (4×3) dimer sites could be occupied with Bi atoms in addition to Ga and As atoms. To that end, first principle DFT calculations were done of the $\alpha\,(4 \times 3)$, $\beta\,(4 \times 3)$, and $h0\,(4 \times 3)$ reconstructions, including several configurations with Bi occupying the dimer sites in black in Fig. 3.10(a). These energies were obtained using VASP as mentioned in Ch. II.[37, 62, 63, 64] In particular, configurations were chosen that matched the reconstruction units seen in high resolution STM (Fig. 3.11(a)) of the surface produced from depositing 12 s of Bi onto the $\beta 2\,(2 \times 4)$ reconstruction (the same surface seen in Fig. 3.4) Simulated STM (Fig. 3.11(b)) of these configurations was constructed using the Tersoff-Hamann formalism of calculating STM images and compared to the experimental STM shown in Fig. 3.11(c).[65] One $\beta\,(4 \times 3)$ configuration in particular, where Bi occupies all but one of the anion sites, matches the $\beta\,(4 \times 3)$ units. Moreover, a black box was drawn in Fig. 3.11(c) to the size of the (4×3) unit cell of 1.6 nm $\times$ 1.2 nm, which fits the observed reconstruction units very well.

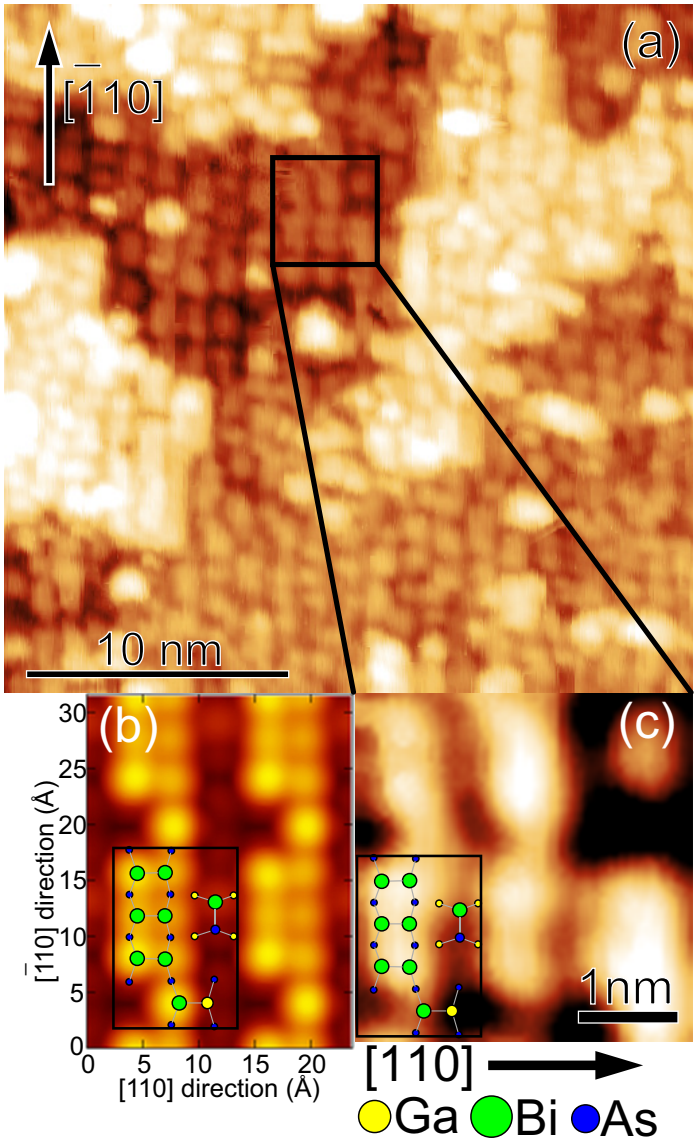

Figure 3.11. (a) 25 nm STM image of a different location on the same surface as shown in Fig. 3.4). (b) Simulated STM of the $\beta\,(4\times3)$ configuration with Bi occupation of several sites, which matches closely the individual reconstruction units shown in (c). The black boxes in (b) and (c) correspond to the (4×3) reconstruction size of 1.2 nm $\times$ 1.6 nm.

Therefore, it is reasonable to conclude the $(n\times3)$ periodicity arises from a disordered (4×3) reconstruction. From inspection of any STM images of the Bi-terminated surfaces presented above, it is clear the $(n\times3)$ reconstruction units are not uniform in appearance. The intensity varies from one to the next, suggesting a difference in composition. Given that the disorder is prevalent enough to destroy the $4\times$

periodicity on most Bi-terminated surfaces, which involves shifting of entire (4×3) rows, it is not altogether surprising that the occupancy is not uniform either. Hence, it is impossible to assign a (4×3) reconstruction model with a specific composition to the entire surface, but rather many configurations of the (4×3) reconstruction exist simultaneously. This will be explored in depth in Ch. IV.

3.6 Conclusions

In conclusion, several GaAs samples were grown with MBE with various amounts of Bi deposited onto the surface. Both the GaAs(001) $\beta2\,(2 \times 4)$ and $c\,(4 \times 4)$ reconstructions were tried as starting surfaces prior to Bi deposition. Both of these surfaces transformed upon Bi deposition into a disordered row reconstruction of $(n \times 3)$ periodicity, where $n = 1, 2, \text{or } 4$, depending on the amount of Bi used and if an As overpressure was also present. The (2×3) RHEED patterns appeared after only ≈0.8 ML of Bi and were indicative of a mixed reconstruction, where $\beta2\,(2 \times 4)$ and $(n \times 3)$ reconstruction rows produced a combined (2×3) periodicity when sampled with RHEED. Adding more Bi, up to ≈1.4 ML caused the $\beta2\,(2 \times 4)$ rows to entirely transform into $(n \times 3)$ rows, eliminating the $2\times$ periodicity. Annealing of this surface for 1 hr caused some Bi desorption, in turn causing a transformation of part of the $(n \times 3)$ reconstruction rows back into $\beta2\,(2 \times 4)$ rows, as indicated by the re-emergence of the (2×3) RHEED pattern and the STM. Finally, the addition of a small amount of As in addition to Bi produced a somewhat more ordered surface, as evidenced by the faint (4×3) RHEED pattern.

A mechanism was proposed for the MLS smoothing effect seen in this and other work. In this model, the large Bi atoms would prefer to sit at terrace edges, permitting relaxation outward over the terrace below. Such a preference causes the observed high density of step edges seen in Bi-terminated GaAs surfaces. This work could be extended by simulation methods, in particular the use of a solid-on-solid

model, where individual (4×3) units are treated as individual blocks on a surface. Step edge energies and surface energies can be varied in order to reproduce the step edge morphology seen in STM, and thus could be used to verify or refute the model proposed for the smoothing mechanism.

Finally, the $(n \times 3)$ reconstruction was proposed to be a disordered (4×3) reconstruction, as suggested by the near stability of the (4×3) reconstruction in GaAs based upon other studies. Simulated STM of the (4×3) reconstruction compares well with high resolution STM of the $(n \times 3)$ reconstruction. This structure will be thoroughly investigated in Ch. IV and its stability relative to other reconstruction calculated using DFT.

CHAPTER IV

Calculated Bi/GaAs Surface Phase Diagram

4.1 Introduction

In Ch. III, several experimental observations of the Bi/GaAs surface were presented. The appearance of the $(n \times 3)$ RHEED patterns and measurements of the reconstruction units observed in STM suggested the $(n \times 3)$ surface consists of a disordered (4×3) reconstruction. A limitation of the experimental approach in accurately characterizing the atomic structure of the Bi/GaAs surface lies in the necessity of considering both its structure and composition. This has been successfully overcome in several systems, including the Mn-doped GaAs (110),[66, 67] the Co_2MnSi/GaAs(001),[68] the InGaAsN,[69] in Si-doped bulk GaAs,[70] and both undoped and Si-doped GaAs nanowire systems.[71] This was possible due to experimental observations in these systems. However, the Bi/GaAs system is too disordered to explain with experiments alone.

Bulk atomic structure is also affected by Bi incorporation, on which some work has already been done. Extended x-ray absorption fine spectra EXAFS,[43] DFT calculations,[72] and transmission electron microscopy results[44] suggest that Bi substitutes for As in $GaAs_{1-x}Bi_x$. This is in contrast to the proposed Bi_{Ga} anti-site defects to explain certain Raman spectroscopy observations[73] and trap states in $GaAs_{1-x}Bi_x$.[74] Bi also exhibits both clustering and ordering in bulk GaAs lattice

depending on the composition. At Bi concentrations of 1-2.5%, Bi atoms preferentially form dimers or tetramers on the group V sublattice.[43] At Bi concentrations of 3-10%, $GaAs_{1-x}Bi_x$ develops $CuPt_B$ ordering,[24] which was attributed to the Bi-rich (2×1) surface reconstruction proposed by Laukkanen *et al.*[19, 20, 21, 50] Above a Bi concentration of 13%, the ordering disappears and coarse phase separation occurs.[24] Bi has been shown to significantly disrupt the $CuPt_B$ ordering in InGaP[75] which was attributed to Bi-induced surface reconstructions. Thus, there is a connection between the atomic surface structure during growth and the final observed bulk atomic structure. Even more so, the change to the step morphology seen in Ch. III can affect final interfacial quality in heterostructure devices in subsequent growth on such a surface.

As such, there is a definite motivation to understanding the atomic structure of the Bi-induced surface reconstructions and for what conditions they are stable. In the Bi/GaAs system, several experimental observations have already been established for some of these reconstructions. There are a number of surface reconstructions that have been observed on this surface. Laukkanen *et al.* have shown the (2×1) reconstruction appears when Bi is deposited on a metal-terminated surface and has been studied extensively using STM and DFT.[19, 20, 21] The same authors have also shown Bi-induced $\alpha 2\,(2 \times 4)$ reconstructions are stable after heating the (2×1) surface.[19, 20, 21, 50, 51] The $(n \times 3)$ set of reconstruction is observed under MBE conditions,[23, 52, 53] where it was proposed in Ch. III the $(n \times 3)$ RHEED patterns emerge from a disordered (4×3) reconstruction. In the case of the $(n \times 3)$ reconstruction these studies are also blind to the surface composition. Moreover, Bi-containing $c\,(4 \times 4)$ and $\beta 2\,(2 \times 4)$ configurations have not been considered fully with DFT and have not been experimentally observed. Thus, a general sense of what conditions stabilize these reconstructions is understood, but a more rigorous study is required to determine these limits precisely.

4.2 Cluster Expansion

The atomic structure of a surface, that is the bonding and arrangement of atoms at the surface to satisfy the dangling bonds, is captured by the surface reconstruction unit cell. This will be referred to in this work as the structural configuration of the surface. Different reconstructions, such as the $\alpha 2\,(2 \times 4)$, $\beta 2\,(2 \times 4)$, and $c\,(4 \times 4)$ reconstructions, all represent different structural configurations. Changes in structural configuration changes the energy on the order of 100 meV/ ((1×1) area) *Within each structural configuration,* the different species (in this case Ga, As, and Bi), can occupy the various sites within the structure. This is known as the compositional configuration, changes of which cause energy changes on the order of 10 meV/ ((1×1) area). The Bi-Bi and Bi-As dimer-containing variants of the (2×1) reconstruction are examples of compositional configurations.[19, 20] Thus, structure is a stronger determinant of surface stability than composition.

4.2.1 Structural Enumeration

All of the desired atomic structures to be compared must be assembled to start constructing the phase diagram. As shown in Ch. III, RHEED and STM provide a wealth of information on the structural configuration, but experimentally discerning details of the species at each atomic site is limited by the STM resolution. Moreover, this is not an exhaustive approach, as many structures and configurations are likely to be overlooked. For instance, Laukkenen *et al.* calculated a Bi/GaAs phase diagram based upon their experimental results at low As overpressure.[19] Their experiments did not show any $(n \times 3)$ periodicities in low-energy electron diffraction, and thus, there was no motivation to take the $(n{\times}3)$ reconstruction into consideration. Nonetheless, experimental observation is useful in guiding the enumeration process to follow.

In this chapter, a fully comprehensive approach is applied to ensure that all pos-

sible structures are considered and enumerated. These structures are constrained to have only known features typical of anion-terminated III-V surfaces, according to the following rules[60]:

1. Only threefold and fourfold coordination is allowed for surface atoms, permitting dimers and backbonds.

2. Lone surface atoms unbounded to other surface atoms are not permitted.

3. Fourfold surface atoms cannot have in-plane bonds, preventing the formation of trimers or lines of surface atoms successively bonded to one another in a chain.

4. Subsurface vacancies are not allowed.

These rules were applied to the (2×4), $c\,(4 \times 4)$, (2×1), and (4×3) unit cell sizes. These were chosen as these sizes are observed experimentally. The lowest energy structures were extracted from the resulting database of structures using the electron counting model.[76] The $\alpha 2\,(2 \times 4)$, $\beta 2\,(2 \times 4)$, and $c\,(4 \times 4)$ reconstructions, shown in Fig. 4.1(a-c), were identified via this method, in agreement with prior experimental work on stable GaAs reconstructions.[27] The Ga-rich $\zeta\,(4 \times 2)$ reconstruction[77] (Fig. 4.1(d)) was included as a cation-rich reference surface; since the Ga-rich reconstructions do not follow the same structural rules given above, exploration of Ga-terminated reconstructions was not possible. Enumeration of (2×1) reconstructions produced only one possibility that obeys the structural rules. This configuration is metallic, and does not obey the electron counting model owing to a deficit of one electron per unit cell. This is in agreement with scanning tunneling spectroscopy results that confirm the metallic nature of the (2×1) surface.[19]

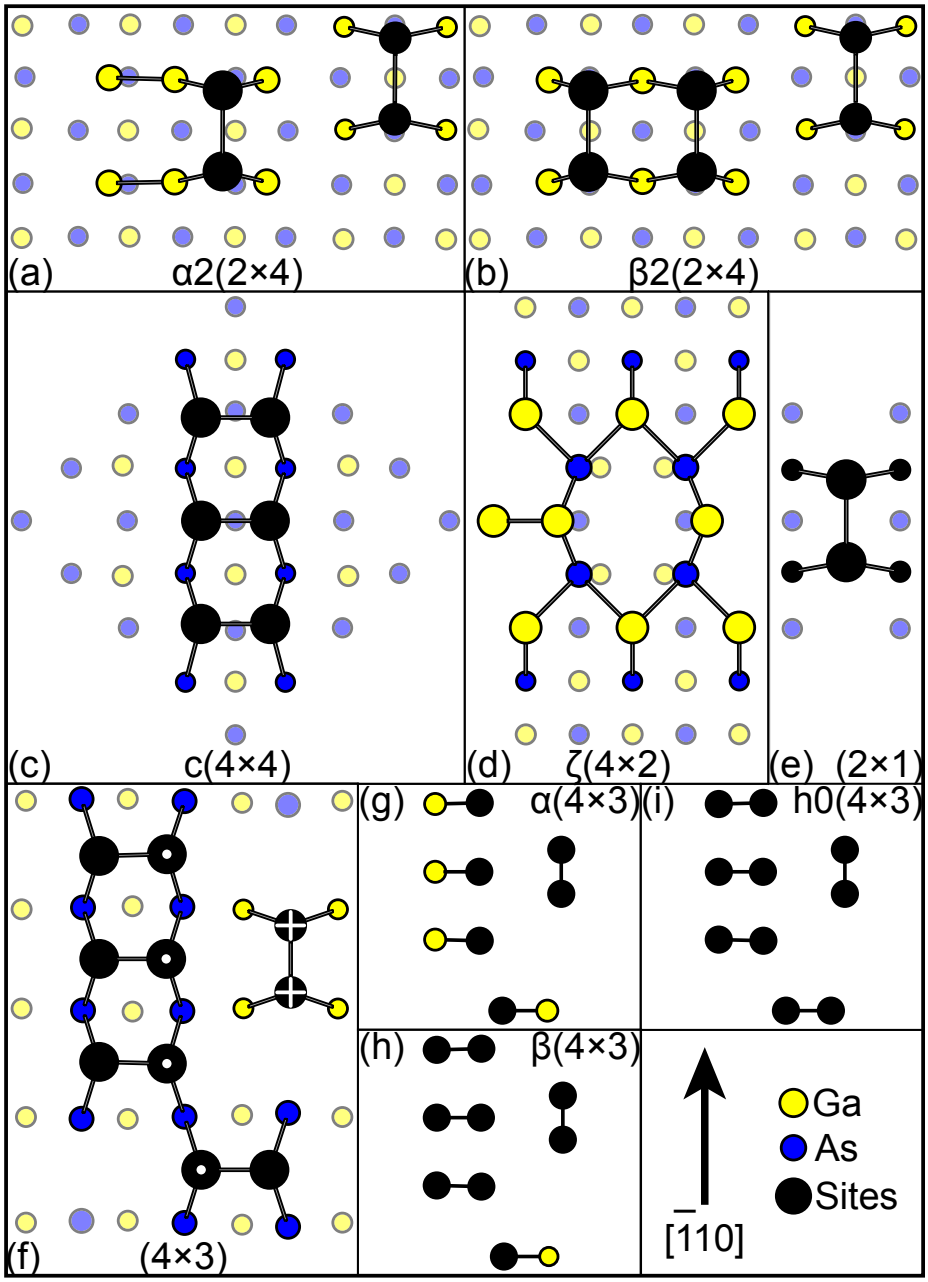

Figure 4.1. Reconstruction models for (a) the $\alpha 2\,(2\times 4)$, (b) $\beta 2\,(2\times 4)$, (c) $c\,(4\times 4)$, (d) $\zeta\,(4\times 2)$, (e) (2×1), and (f) (4×3) reconstructions. In (f), the sites with white dots are restricted to Bi and As occupancy and the sites with white + signs only allow As occupancy when enumerating (4×3) supercell configurations. (g) $\alpha\,(4\times 3)$, (h) $\beta\,(4\times 3)$, and (i) $h0\,(4\times 3)$ variants of the general (4×3) model.

As for the observed (1×3) and (2×3) periodicities,[52, 78, 23, 22] the (4×3) model proposed in Ch. III (Fig. 3.10) was used instead to simulate these surfaces. A (1×3) reconstruction unit cell was not identified as stable as none of those structures obey the structural rules and no surface reconstruction of odd unit area satisfies the electron counting rule.[60] Also, as mentioned in Ch. III, according to structure factor calculations by Romanyuk *et al.*, the (4×3) reconstruction can produce a (1×3) or a (2×3) RHEED periodicity.[55] Finally, Barvosa-Carter *et al.* observed relatively ordered (4×3) reconstructions on AlSb and GaSb even though the RHEED patterns for these surfaces show a (1×3) periodicity.[61]

4.2.2 Compositional Enumeration

With the enumerated structures in hand, the compositional configurations must be enumerated for each structure. A Ga, As, or Bi atom can occupy any threefold coordinated dimer site without affecting the electron counting rule, allowing many valid configurations for a given composition of the surface. For example, there are over 30,000 symmetrically distinct configurations in just the (4×3) structure depicted in Fig. 4.1(f), far too many to test individually with DFT. Instead, the compositional configurations are enumerated using the cluster expansion formalism, which was discussed in Sec. 2.8.2.[39] As applied to the present system, the cluster expansion is used to predict the surface energy depending on the species occupation of the specified sites, as was demonstrated in the InGaAs system.[79] These sites are usually the dimer atoms, although second layer atoms (the atoms the dimers sit on) may be chosen in some cases.[38]

Four separate cluster expansions were constructed, one each for the $c\,(4 \times 4)$, (4×3), and (2×1) reconstructions, and one to describe both the $\alpha 2\,(2 \times 4)$ and $\beta 2\,(2 \times 4)$ reconstructions. Ga, As, or Bi atoms may occupy the black sites in Fig. 4.1, while only As or Bi may occupy the black sites with white dots in Fig. 4.1(f). Note

that the (2×1) cluster expansion permits substitution of the second layer atoms bonded to the dimer atoms. This was allowed to investigate the possibility of Bi_{Ga} anti-sites as proposed by Laukkanen *et al.* to explain the existence of semiconducting (2×1) reconstructions.[19, 20]

Each configuration was constructed in a 5 ML thick GaAs slab with the reconstruction on one face. The partially-filled electronic states of each As atom on the opposite face are passivated by two pseudo-H atoms ($Z = 0.75$). All electronic structure calculations were performed with VASP as mentioned in Sec. 2.8.1.[37] Energies of the various configurations were calculated using DFT under the LDA as implemented in ultrasoft pseudopotentials for Ga, As, Bi, and pseudo-H. The reconstructed surface was relaxed using a $12 \times 12 \times 1$ k-point mesh and a 203-eV plane-wave energy cutoff.

Each of the reconstruction unit cells shown in Fig. 4.1 are all examples of primitive unit cells. Some cluster interactions are long enough and the sites involved close enough that the cluster can span more than one unit cell. Thus, the primitive cell alone is not sufficient to determine all of the ECIs. For all the reconstructions except the (2×1) reconstruction, supercell configurations consisting of two primitive cells (known as a volume 2 supercell configuration) were considered. Given the smaller size of the (2×1) reconstruction, some clusters could potentially span more than two primitive cells; as such, supercell configurations up to three primitive cells (volume 3) were considered.

The (4×3) reconstruction required some limits on the site occupancy in order to successfully enumerate the volume 2 supercell configurations. Allowing all three species on the twenty dimer sites of the volume 2 (4×3) supercells results in $\approx 0.5\,(3^{20}) = 1.74 * 10^9$ configurations, far too many to enumerate even with the cluster expansion. Fortunately, the volume 1 (4×3) cluster expansion predicts the stability of the $\alpha\,(4 \times 3)$, $\beta\,(4 \times 3)$, and $h0\,(4 \times 3)$ variants to the exclusion of all other possible (4×3) configurations. Moreover, Bi and Ga substitution at the trench

dimer sites is unfavorable as those sites were predicted to be the last to accept Bi, and Ga never appeared at those sites at all. Therefore, Ga occupation of sites with white dots and Bi or Ga occupation of the trench dimer sites with white + signs are energetically unfavorable. Eliminating these substitutions reduces the number of possible configurations to $1.26 * 10^6$ configurations, a much more tractable number of configurations that can be enumerated.

4.3 Phase Diagram

All the final groundstate configurations predicted by the cluster expansions were calculated with DFT and compared to produce a phase diagram of stable surface configurations. The first step to constructing the phase diagram involves calculating the surface free energy γ related to the total energy E_{DFT} by the following equation:

$$\gamma = \frac{E_{DFT} - N_{Ga}E_{GaAs} - N_{As}^{XS}\mu_{As} - N_{Bi}^{XS}\mu_{Bi}}{N_A} - \gamma_H \tag{4.1}$$

where N_{Ga} is the number of Ga atoms in the calculated slab, N_A is the number of (1×1) surface unit cells in the surface supercell, N_{As}^{XS} and N_{Bi}^{XS} are the number of excess surface As and Bi atoms, and μ_{As} and μ_{Bi} are the As and Bi chemical potentials. E_{GaAs} is the calculated DFT energy of bulk zinc-blende GaAs, and γ_H is the surface energy per (1×1) surface unit cell of the pseudo-H layer.[80] Because the surface is a chemically open system, μ_{As} and μ_{Bi}, not N_{As}^{XS} and N_{Bi}^{XS}, are the independent variables in the surface energy equation.

Matlab code was used to plot γ, which is included in Appendix A. The γ plot for a single (4×3) configuration is a plane as shown in Fig. 4.2(a). A plot of γ for all the configurations, then, is a series of planes as shown for the (4×3) reconstruction in Fig. 4.2(b). Whichever plane has the lowest γ value at a given (μ_{As}, μ_{Bi}), that configuration will be the most stable. Thus, the underside of all the planes seen when

looking along the arrow in Fig. 4.2(b) is the phase diagram of surface stability, in this case just for the (4×3) reconstruction (Fig. 4.2(c)).

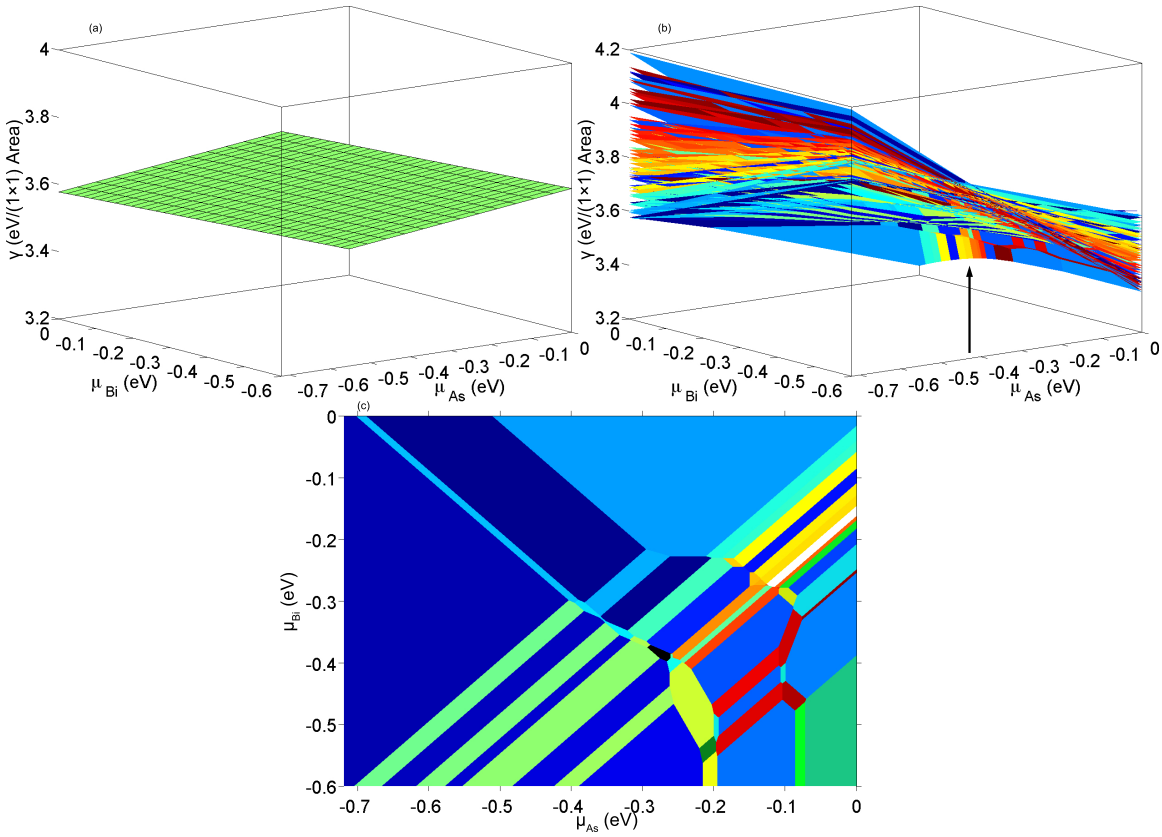

Figure 4.2. (a) γ of a single (4×3) configuration, (b) γ of all the Bi/GaAs (4×3) configurations, (c) 2D view normal to the arrow in (b) showing *only* the lowest energy (4×3) groundstates.

Repeating this process for all the configurations of the above mentioned structures results in the 0K Bi/GaAs surface phase diagram in Fig. 4.3. The chemical potentials are plotted with respect to their values in crystalline bulk reservoirs at 0 K. The limits of surface stability range from $\mu_{As} = \mu_{As}^{(bulk)}$ and $\mu_{Bi} = \mu_{Bi}^{(bulk)}$ at the upper end and $\mu_{As} = \mu_{As}^{(bulk)} - \Delta H_f^{GaAs} = -0.72$ eV/atom at the lower end, where $\mu_{As}^{(bulk)}$ and $\mu_{Bi}^{(bulk)}$ are the chemical potentials of bulk As and Bi, and ΔH_f^{GaAs} is the GaAs formation energy in eV/atom. In other words, at the upper limits, the surface system becomes unstable relative to bulk As and bulk Bi, while at the lower end, the surface system becomes unstable as μ_{As} becomes low enough to cause As desorption and Ga droplet

formation. It is assumed no Bi incorporates into the underlying bulk GaAs; thus, Bi is not involved in the stabilization of bulk GaAs, and the lower limit on μ_{Bi} is arbitrary.

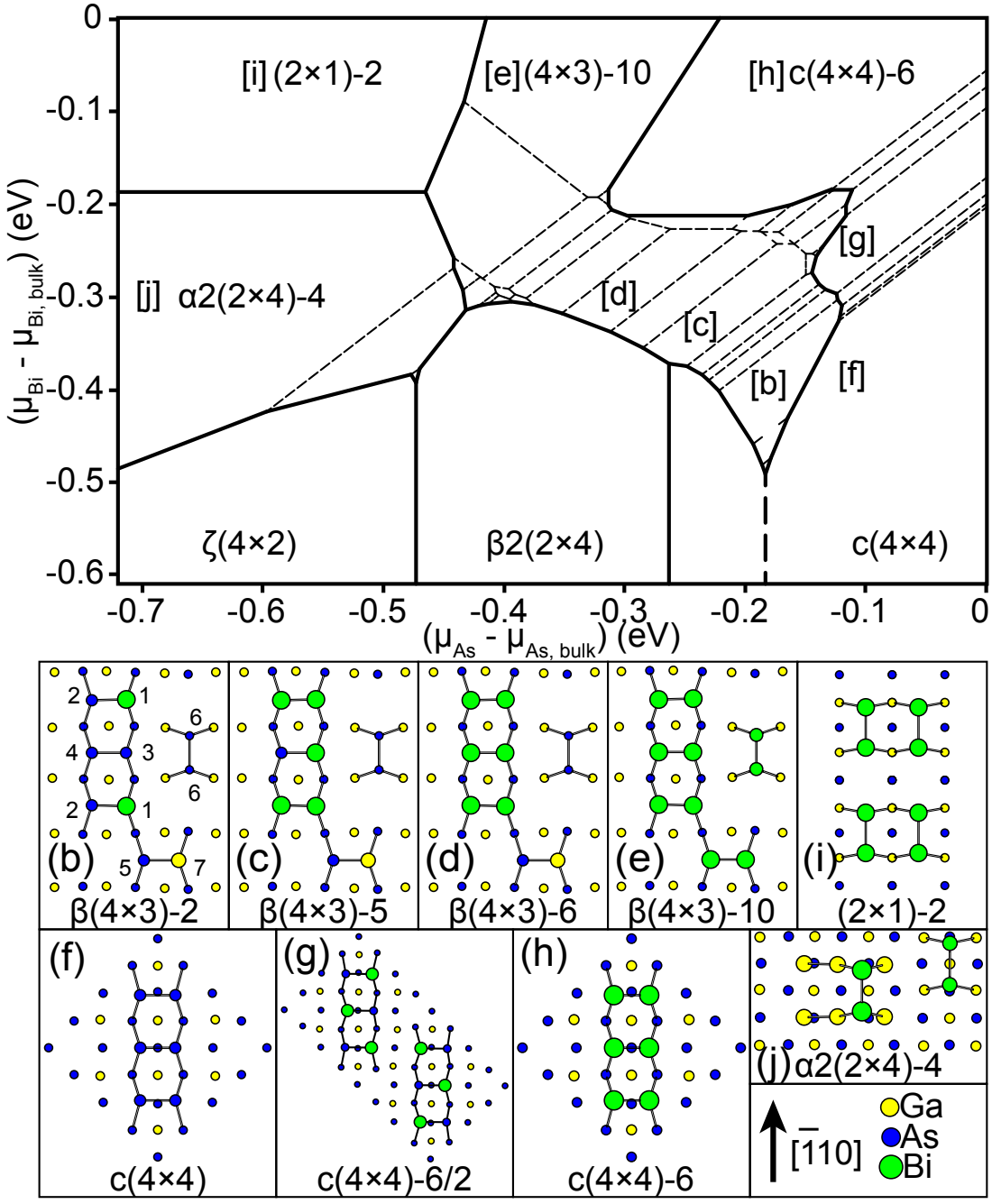

Figure 4.3. Bi/GaAs 0 K phase diagram of DFT energies. Thick lines separate different reconstructions (structural configuration), dashed lines separate different compositions with a reconstruction (compositional configuration). Letters in parenthesis show the stable configurations, which correspond to the regions of stability indicated by the same letters in square brackets.

Figure 4.3 shows many stable configurations. The numerical suffix after the reconstruction designation indicates the number of Bi atoms in the configuration, and

if it is a supercell configuration, it is specified as a fraction as the number of Bi atoms per number of primitive cells. For instance, configuration (g) in Fig. 4.3 has six Bi atoms occupying sites over two $c\,(4 \times 4)$ unit cells, defining this configuration as the $c\,(4 \times 4)$-6/2 configuration. This is not to be considered a $c\,(4 \times 4)$-3 configuration, where Bi atoms would occupy the same three sites in every $c\,(4 \times 4)$ primitive cell. A listing of all the predicted stable configurations in Fig. 4.3 are given in Appendix B.

Figure 4.3 is consistent with all experimental observations. Several of the stable configurations are shown in Fig. 4.3. As expected, the Ga-terminated $\zeta\,(4 \times 2)$ reconstruction appears under Ga-rich, anion-lean conditions (low μ_{As} and μ_{Bi}), while at As-rich conditions (high μ_{As}), the diagram is dominated by the As-rich $c\,(4 \times 4)\,\beta$ reconstruction. The (2×1) reconstruction appears at Bi-rich, As-lean conditions (high μ_{Bi}, low μ_{As}). Finally, the $\alpha 2\,(2 \times 4)$, $\beta 2\,(2 \times 4)$, and (4×3) reconstructions are stable at more intermediate values of (μ_{As}, μ_{Bi}). Properties of all the enumerated reconstructions are discussed in the following sections.

4.3.1 (4×3) Configurations

The (4×3) reconstruction predictions are consistent with the experimental RHEED phase diagram produced by Masnadi-Shirazi *et al.*,[23] where the Bi-rich (2×1) reconstruction is observed using MBE at lower As_2:Ga ratios and higher temperatures. In that work, the RHEED pattern transformed from a (2×1) pattern to a (2×3) pattern and then a (1×3) pattern upon increasing the As overpressure. This is consistent with Fig. 4.3, where the (2×1) reconstruction changes to a (4×3) reconstruction with increasing μ_{As}.

The (4×3) reconstruction (configurations (b-e) in Fig. 4.3) has twenty-nine stable configurations, far more than all other structures combined. This indicates the (4×3) reconstruction accommodates a wide variety of surface Bi concentrations more readily than any other structure, over a wide range of μ_{As}. This is consistent with

the results of Bi deposition on the $\beta 2\,(2\times 4)$ and $c\,(4\times 4)\,\alpha$ in Ch. III. The small size of some of the regions of configurational stability also suggest the (4×3) configurations are close in energy, allowing thermal energy to induce the coexistence of many configurations on a surface. This is consistent with the experimental observations of surface disorder seen in Ch. III. As discussed in Sec. 3.5 and shown in Fig. 3.10, the (4×3) reconstruction has three primary variants: the $\alpha\,(4\times 3)$, $\beta\,(4\times 3)$, and the $h0\,(4\times 3)$. These variants can be thought of as substructure configurations of the general (4×3) structure, which are automatically included in the general (4×3) cluster expansion. As such, there are different compositional configurations, with four, thirteen, and eight stable configurations, respectively, for each. Moreover, four distinct supercell configurations combining either $\alpha\,(4\times 3)$ and $\beta\,(4\times 3)$ or $\beta\,(4\times 3)$ and $h0\,(4\times 3)$ primitive cells are stable. These hybrid configurations exist between the regions where the three individual variants are stable (see Appendix B).

Finally, it is seen that starting from the most As rich $\beta(4\times3)$ configuration, the region of (4×3) reconstruction stability expands as μ_{Bi} is increased, and Bi occupies the anion sites of the $\beta\,(4\times 3)$ in the order indicated by the numbers in Fig. 4.3(b). Thus, it is concluded that adding Bi stabilizes the (4×3) reconstruction, overcoming the $\approx$25 meV energy difference between it and the GaAs $\beta 2\,(2\times 4)$ and $c\,(4\times 4)$ reconstructions.

4.3.2 $c\,(4\times 4)$ Configurations

The $c\,(4\times 4)$ reconstruction possesses nine groundstate configurations (Fig. 4.3(f-h)). Similar to the (4×3) reconstruction, the $c\,(4\times 4)$ reconstruction has two variants, the $c\,(4\times 4)\,\alpha$ and the $c\,(4\times 4)\,\beta$ reconstructions.[27] As with the (4×3) reconstruction variants, these two variants can be considered substructures. The $c\,(4\times 4)\,\alpha$ variant possesses no stable Bi-containing configurations. It is worth noting that the lone stable $c\,(4\times 4)\,\alpha$ configuration is in fact a supercell configuration (see Ap-

pendix B). The Ga-As heterodimers are oriented the same direction within their primitive cell, but the orientation reverses between primitive cells. This behavior is seen in the filled states STM of Fig. 3.6(c) and in other work,[27] indicating the dimer orientation is rather disordered. The stable $c\,(4 \times 4)\,\alpha$ configuration is an attempt to capture this disorder.

As expected, the pure GaAs $c\,(4 \times 4)\,\beta$ configuration consisting of As-As homodimers is stable at high μ_{As} and low μ_{Bi}. As μ_{Bi} increases Bi begins to substitute for As on the dimer sites, until for high μ_{As} and μ_{Bi}, all six of the dimer sites contain Bi, producing the $c\,(4 \times 4)$-6 configuration (Fig. 4.3(h)). Several of the configurations are very close in energy, as indicated by the small regions of stability. The $c\,(4 \times 4)\,\beta$-6/2 configuration possesses a relatively large range of stability. This configuration consists of Bi-As heterodimers that alternate in orientation within its primitive cells, possibly to alleviate the strain of incorporating the large Bi atoms into the dimer sites. The three Bi-containing $c\,(4 \times 4)\,\beta$ configurations before the $c\,(4 \times 4)\,\beta$-6/2 also show this behavior, where Bi atoms occupy sites not directly adjacent to another Bi atom.

4.3.3 (2×4) and (2×1) Configurations

The remaining reconstruction prototypes only possess one or two configurations each. The appearance of Bi-containing $\alpha 2\,(2 \times 4)$ configurations and the lack of a Bi-containing $\beta 2\,(2 \times 4)$ configuration are consistent with the LEED, STM, DFT, and photoemission spectroscopy of the Bi-induced (2×4) surfaces seen by Laukkanen *et al.*[19, 20, 21] In the $\alpha 2(2{\times}4)$ reconstruction (Fig. 4.1(a)), the $\alpha 2\,(2 \times 4)$-4 (Fig. 4.3(j)) and $\alpha 2\,(2 \times 4)$-3 configurations are stable (see Appendix B).

The metallic (2×1)-2 configuration is the only stable (2×1) configuration and consists entirely of Bi-Bi homodimers bound to Ga atoms in the second layer. This structure does not obey the electron counting rule. By allowing second-layer sites to be occupied by Ga, As, or Bi, charge balance may be satisfied, and (2×1) configu-

rations that obey the electron counting rule can be explored through Bi_{Ga} or As_{Ga} anti-sites. No stable configurations were found that exhibit this feature, in contrast to the proposed explanation by Laukkanen *et al.*.[19, 20] It is unknown why these semiconducting regions arise. Neither bulk defects that allow surface charge balance nor kinetic trapping during growth of an Bi_{Ga} anti-site defect suffice as an explanation here. In the experimental work, Bi was deposited at room temperature onto a GaAs substrate, not via MBE. No growth was occurring with a Bi flux, precluding both explanations. Another possibility lies in the known underestimation of the band gap by the LDA, potentially leading a semiconducting (2×1) configuration to be considered artificially metallic and thus artificially high in energy.

4.4 Monte Carlo Simulations

The appearance of several different configurations in the (4×3) reconstruction region on the phase diagram of Fig. 4.3 corroborates the (4×3) reconstruction disorder observed in Ch. III. Likewise, the lack of many configurations in the (2×1) and (2×4) regions, along with the limited number of $c\,(4 \times 4)$ configurations, suggest these reconstructions are more stable and less disordered. Indeed, the STM observed by Laukkanen *et al.* attest to the order seen in the Bi-induced (2×1) and $\alpha 2\,(2 \times 4)$ reconstructions.[19, 20, 21] Figure 4.3 is a 0 K phase diagram, but real experimental systems operate at finite temperature, providing thermal energy to the surface system. This energy may be enough to allow a variety of compositional configurations to coexist with the groundstate.

4.4.1 Monte Carlo Setup

In order to quantify these effects in the Bi/GaAs(001) surface at finite temperature, grand canonical sMC simulations were performed for the (2×1) and (4×3) structures. These two structures represent the extremes of a highly ordered recon-

struction in the (2×1) and a highly disordered reconstruction in the (4×3). The (2×1) reconstruction is simple to simulate, with few sites and configurations to consider, and will be discussed first. To investigate the (4×3) reconstruction, three simulated cooling simulations were run from 530°C (803 K) to -270°C (3 K) in 10°C increments at the fixed (μ_{As}, μ_{Bi}) points depicted as open circles on the phase diagram in Fig. 4.4(a). This range of temperature includes the Bi deposition temperatures of 400-440°C used in the experiments of Ch. III.

As was described in more detail in Sec. 2.8.3 the sMC simulation performs surface site substitution and tracks the average energy, composition, and point cluster correlations of the surface dimer sites. Simulation cells consisted of a 16×16 array of the surface structure in question, for a total of 256 primitive unit cells. At every point in (μ_{As}, μ_{Bi}, T) space, Ga, As, or Bi substitution was attempted at each surface site at total 10000 times on average. The system was allowed to equilibrate for the first 5000 passes were for system equilibration and were not included in the calculation of the ensemble averages, to eliminate any bias from the starting surface. After this the ensemble averages were recorded for the final 5000 passes.

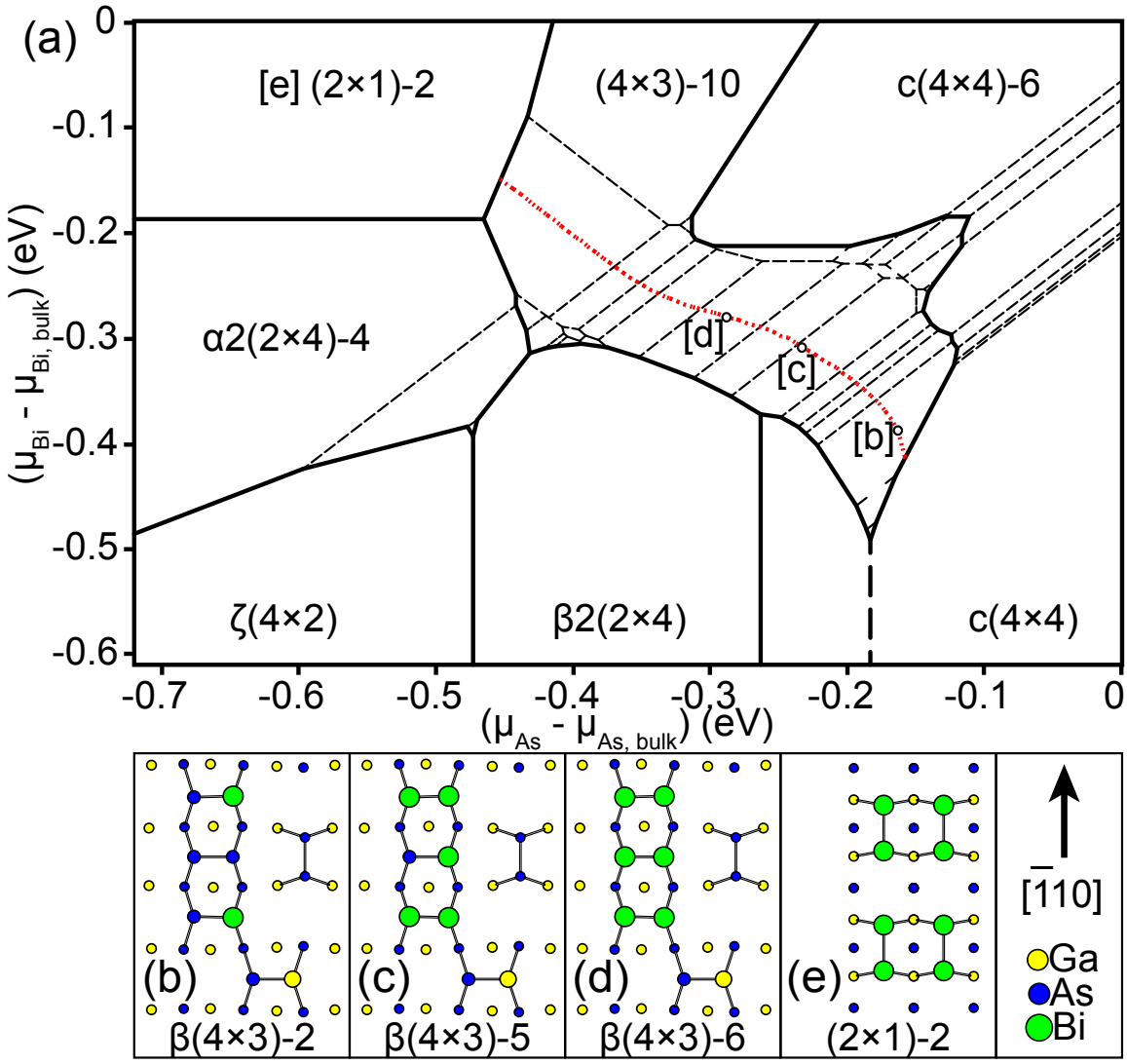

Figure 4.4. (a) The 0 K Bi/GaAs phase diagram. The dotted red line is the contour where the anion fraction of the top-level dimer sites is 7/8, which includes all the $\beta\,(4\times3)$ configurations. (b-d) Models of the (4×3) groundstates in the regions that were simulated using sMC. (e) 2×2 supercell of the lone (2×1) groundstate.

4.4.2 (2×1) and (4×3) Surface Snapshots

Simulated cooling in the (2×1)-2 region of stability shows the (2×1) surface does not change in composition much, even at synthesis temperatures. This is seen in the snapshots of the (2×1) surface shown in Fig. 4.5. For clarity, only a representative portion of the Monte Carlo cell is shown, in this case a 12×8 block of (2×1) primitive cells. In Fig. 4.5(a), the (2×1) surface at -60°C (213 K) shows no appreciable disorder

has occurred. Bi occupies the dimer sites, Ga occupies the second layer sites, matching the (2×1)-2 groundstate throughout the surface. Increasing the temperature to 60°C (333 K) makes no difference as seen in Fig. 4.5(b); the occupation has not changed. Raising the temperature to 440°C (713 K), the surface exhibits occasional Bi-Ga heterodimers, as circled in Fig. 4.5(c). Average site occupation $\langle p \rangle$ is a quantity obtained from the sMC simulation indicating how often, on average, a particular species occupies a given site. Figure 4.5(d) shows the average site occupation of Ga in the second layer sites and Bi in the dimer sites (labelled sites 1 and 2 in the inset of Fig. 4.5(d), respectively) and the insensitivity of both to temperature. Over the simulated temperature range, there is no Bi occupation of the second layer sites and $< 5\%$ Ga occupation of the dimer sites at typical growth temperatures.

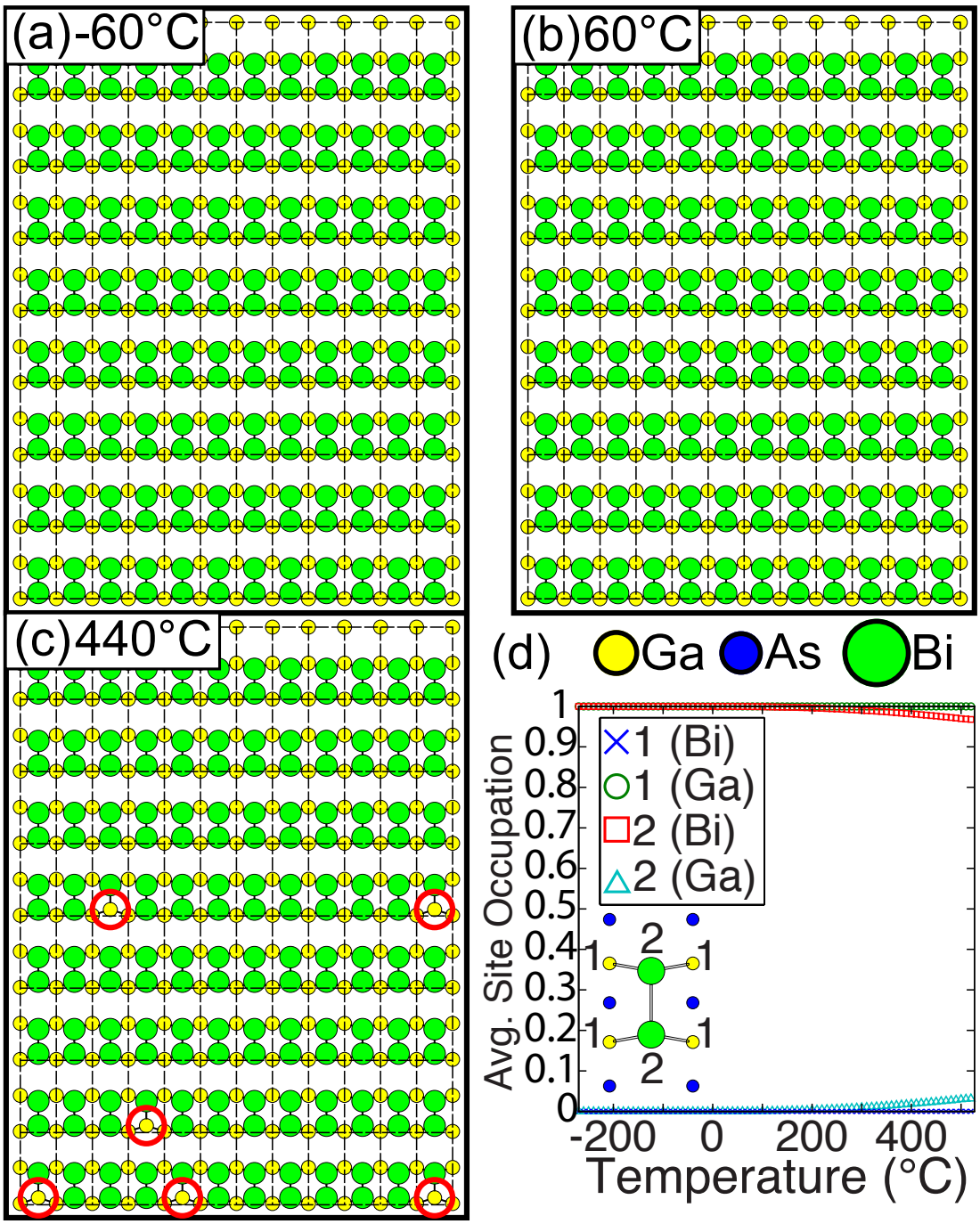

Figure 4.5. Snapshots of the (2×1) surface at (a) -60°C, (b) 60°C, and (c) 440°C. (d) Average site occupation $\langle p \rangle$ of Bi and Ga in the (2×1) reconstruction as a function of temperature. Inset labels the sites in the (2×1) reconstruction.

A similar analysis of the (4×3) surface is shown in Fig. 4.6. The $\beta\,(4 \times 3)$ variant occupies the vast majority of the (4×3) reconstruction region of stability and is directly adjacent to the bare GaAs $\beta 2\,(2 \times 4)$ and $c\,(4 \times 4)\,\alpha$ reconstructions. It is

the most likely (4×3) variant to emerge when depositing Bi; hence, the analysis will focus on these configurations. Figure 4.6 shows the simulated surface at -60°C, 60°C, and 440°C at the (μ_{As}, μ_{Bi}) corresponding to the open circle labeled [b] in the $\beta\,(4 \times 3)$-2 region on the phase diagram in Fig. 4.4(a). At -60°C, the surface snapshot of Fig. 4.6(a) shows most of the unit cells match the $\beta(4\times3)$-2 groundstate and is thus a rather ordered surface. Unlike the (2×1) surface, the (4×3) surface disorders quickly with temperature, until only a handful of unit cells match the groundstate unit cell at 60°C (Fig. 4.6(b)). However, some sites are more resistant to disorder than others, as is deduced by the consistency of Ga-As heterodimers in the kink dimer site and the lack of Ga occupation in sites 2 and 4 (see Fig. 4.3(b) for site labels). At a temperature of 440°C typical of MBE, the surface is largely disordered(Fig. 4c), with substitution now occurring on the kink sites and Ga substitution on the dimer chain sites. This corroborates the experimentally observed $(n \times 3)$ reconstruction configurational disorder seen in Ch. III.

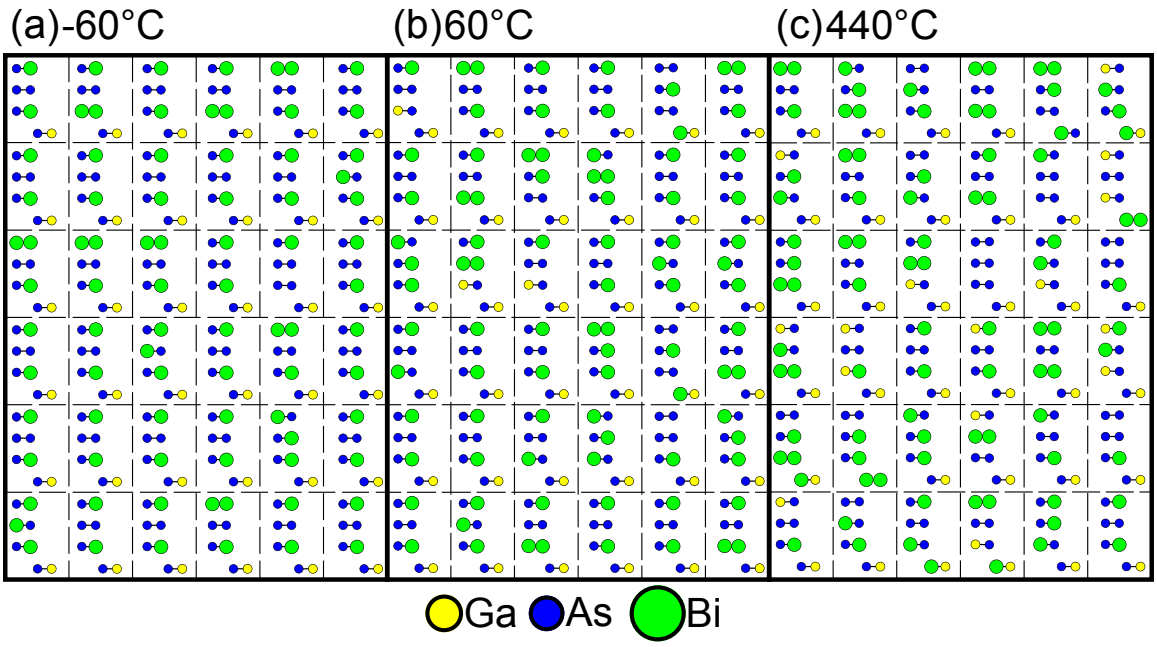

Figure 4.6. Monte Carlo surface snapshots of the $\beta\,(4 \times 3)$-2 surface at (a) -60°C, (b) 60°C, and (c) 440°C.

Finally, a plot like Fig. 4.5(d) of $\langle p \rangle$ is not straightforward for the (4×3) surface.

In the (2×1) surface case, As was not present in the sites, effectively rendering $\langle p \rangle$ a function of (x_{Bi}), where x_{Bi} is average Bi concentration. Moreover, x_{Bi} changes rather smoothly with temperature, making $\langle p \rangle$ a simple parameter to plot. On the (4×3) surface, $\langle p \rangle$ is a function of (x_{As}, x_{Bi}) and $\langle p \rangle$ is not a simple function of temperature. A more effective approach for the (4×3) surface is to define an order parameter to track the site disorder.

4.4.3 Order Parameter η

The order parameter η_i is desired as a measure of the order for a particular symmetrically distinct site i in the primitive unit cell. If all the sites corresponding to site i match the groundstate site i, then $\eta_i = 1$. For a random (that is, uncorrelated) occupation of the surface sites, $\eta_i = 0$.

Since each site i can accommodate multiple species, $\langle p \rangle$ is tracked for each species m on each site i, defined as $\langle p_i^m \rangle$. If $\langle p_i^m \rangle = 0$, sites of type i never contain species m, meaning that species occupation is energetically unfavorable and is anti-correlated at site i. If $\langle p_i^m \rangle = 1$, sites of type i always contain species m, that is, the site is always correlated. As temperature increases, the surface becomes more randomized. Physically, this is the thermal energy gradually overcoming the energy barrier to species substitution on site i. For a system prone to disorder, the energy barrier will be low, while for an ordered system, these barriers are higher. At high temperature, there is no preference for a particular species to occupy a given site, and the average site occupancy $\langle p_i^m \rangle$ asymptotically approach the average concentration x_m, regardless of the initial value of $\langle p_i^m \rangle$. Thus, for η_i^m (the order parameter at site i for species m) to be zero at high temperatures, the following correction to $\langle p_i^m \rangle$ must be included:

$$\eta_i^m = \langle p_i^m \rangle - x_m \tag{4.2}$$

Furthermore, as temperature approaches 0 K, the surface will be highly ordered,

and $\langle p_i^m \rangle \sim 1$ for the species on site i in the groundstate and $\langle p_i^m \rangle \sim 0$ for all other species. After the correction in Eq. 4.2, $\langle p_i^m \rangle$ no longer approaches these limits, and thus η_i must be renormalized by the distance between the ordered ($\langle p_i^m \rangle = 1$) and disordered ($\langle p_i^m \rangle = x_m$) limits, that is, $1 - x_m$:

$$\eta_i^m = \frac{\langle p_i^m \rangle - x_m}{1 - x_m} \tag{4.3}$$

Whenever the referring to η_i^m for the species m that matches the groundstate at site i, the m superscript is dropped:

$$\eta_i = \frac{\langle p_i \rangle - x_m}{1 - x_m} \tag{4.4}$$

It is plots of η_i that are of the most interest, as these measure the breakdown in site correlation with temperature, and thus provide a useful means of determining which sites are most prone to disorder in a given configuration. The order parameters η_i are plotted in Fig. 4.7 for all surface sites of the $\beta\,(4 \times 3)$-2, -5, and -6 groundstates. At temperatures near 0 K, η_i for all the sites approach 1. The surface system is ordered, and the sites on the Monte Carlo surface match the corresponding groundstate sites. With increasing temperature, η_i monotonically decreases, indicating a continuous trend toward surface disorder. The order parameter of each distinct site can be compared to the average order parameter for all sites of the unit cell, which is indicated by dashed lines in Fig. 4.7. This indicates which sites become more disordered first.

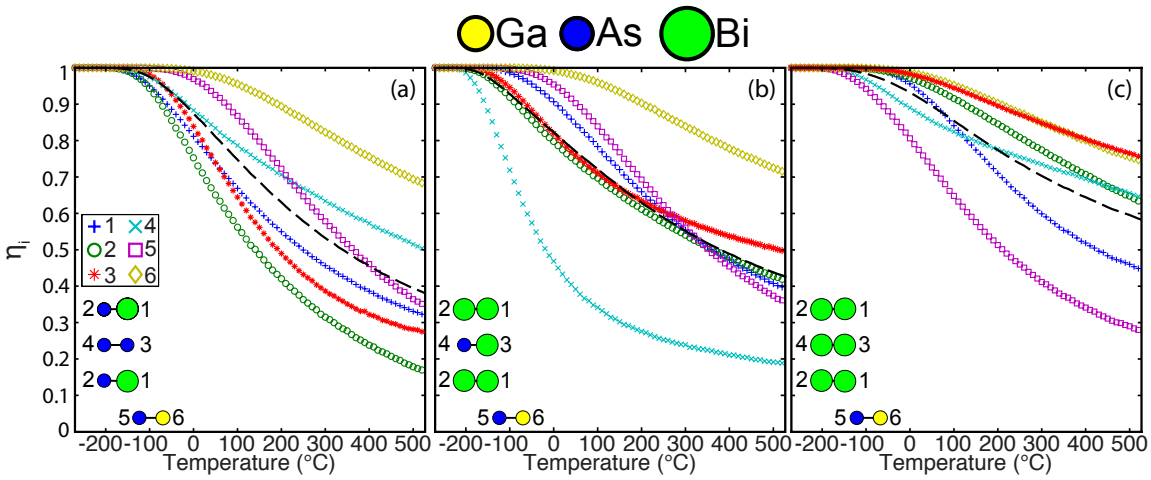

Figure 4.7. Plots of η_i for the (a) $\beta\,(4\times3)$-2, (b) $\beta\,(4\times3)$-5, and $\beta\,(4\times3)$-6 configurations. An average of all η_i values is plotted as a dashed line for each configuration. These plots are for the (μ_{As}, μ_{Bi}) values circled in Fig. 4.4(a).

In all the configurations, η_6 decreases the least with temperature. Thus, site 6 is the least disordered, indicating a strong preference for Ga occupation at that site. In Fig. 4.7(a), η_2 decreases the most readily, indicating a weak favorability of As and Bi in the anion-anion heterodimer. In all three cases, the system shows a preference for substitution on the As sites in the heterodimers, especially the As-Bi heterodimers. Finally, in the $\beta\,(4\times3)$-6 configuration (Fig. 4.7(c)), sites 2 and 3 have only Bi atoms as nearest neighbors, hence η_2 and η_3 are rather invariant with temperature, in contrast with the same sites in the $\beta\,(4\times3)$-2 configuration (Fig. 4.7(a)), where those sites are the most volatile. Moreover, site 1 is more volatile now since a Bi atom there can switch with the As atom in site 5. These trends in η_i underscore how surface diffusion can be altered by the surface reconstruction through the limiting of available sites for adatom migration. When most of the surface anion sites are occupied with either As or Bi, substituting more of the dominant species into the dimer sites becomes energetically more costly. As such, configurations of intermediate composition will likely have the highest surface diffusion coefficients.

4.4.4 (4×3) Surface Entropy

While η_i provides useful insight as to the specifics of site disorder, it is rather limited in predicting overall disorder. The plots of Fig. 4.7 only a gradual transition from an ordered surface at low temperatures to a disordered one at high temperatures. The surface snapshots of Fig. 4.6 have the same problem, making a clear identification of a point of onset for disorder difficult to identify. A more quantitative method of measuring overall disorder is to compare the entropy of the correlated surface to the entropy of an ideal surface with no correlation between species. While the transition from an ordered surface to a disordered one is likely a continuous transformation, the entropy comparison can help narrow down over what temperature range this occurs.

The surface excess entropy s^{XS} can be calculated in the same way as done for the InGaAs surface by Thomas *et al.*.[79] This is obtained from the finite-temperature surface free energy $\gamma(\mu_{As}, \mu_{Bi}, T)$ and its derivative:

$$\gamma(\mu_{As}, \mu_{Bi}, T) = E - TS - \mu_{As}N_{As} - \mu_{Bi}N_{Bi} \tag{4.5}$$

$$d\gamma(\mu_{As}, \mu_{Bi}, T) = SdT - N_{As}d\mu_{As} - N_{Bi}d\mu_{Bi} \tag{4.6}$$

γ is known when all sites are occupied by a single species, as the configurational entropy is 0. The other quantities E, N_{As}, and N_{Bi} are calculated by the sMC simulation, and (μ_{As}, μ_{Bi}) are the control variables. Thus, these can be used as reference states with a known γ. Integrating $d\gamma$ from the reference state to any value of (μ_{As}, μ_{Bi}) at constant T yields γ for any surface where S is not 0. Solving Eq. 4.5 for s^{XS}, the relation $s^{XS} = (\Omega - \gamma)/T$ is obtained, where Ω is the generalized surface enthalpy:

$$\Omega = (\langle E^{XS} \rangle - \mu_{As}\langle N_{As}^{XS} \rangle - \mu_{Bi}\langle N_{Bi}^{XS} \rangle)/N_A. \tag{4.7}$$

E^{XS} denotes the surface excess internal energy, and the terms enclosed by angle brackets indicate ensemble-average quantities obtained from the Monte Carlo simulation. N_A is the number of (1×1) surface area units.

To examine the behavior of anion ordering at finite temperature, s^{XS} was calculated along the dotted red line in Fig. 4.4(a). This contour represents where only one Ga atom per (4×3) primitive cell is present, which includes the set of $\beta\,(4 \times 3)$ configurations, although other configurations where Ga occupies sites colored black in Fig. 4.1(f) (labelled 2, 4, and 7 in Fig. 4.3(b)) are included as well. The seven remaining substitutional sites can contain either As or Bi, and the fraction of these containing Bi is denoted as X_{Bi}. Figure 4.8 shows s^{XS} plotted as a function of X_{Bi} at -60°C, 60°C, and 440°C. The ideal configurational entropy along this contour is shown for reference as the dashed line in Fig. 4.8. Note that the ideal surface entropy does not go to zero at X_{Bi}=0 or 1. This is a consequence of the other configurations with Ga occupancy in sites 2 and 4; hence, there is still some Ga configurational entropy allowed even when the anion sites are all occupied with either As or Bi. The surface consists predominantly of $\beta\,(4 \times 3)$ unit cells, and thus the surface system does not form an ideal ternary mixture, but the Bi and As atoms do act as an ideal binary mixture at this temperature.

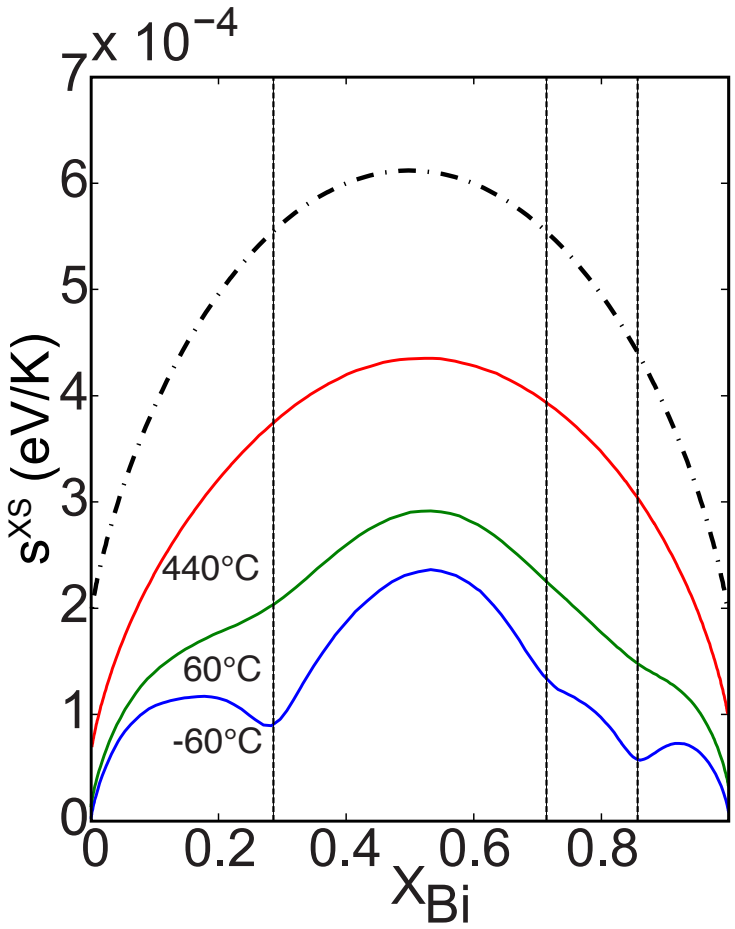

Figure 4.8. Surface excess entropy vs. X_{Bi} as plotted along the contour in Fig. 4.4(a). The surface ideal mixing entropy is plotted as the dash-dotted line.

At -60°C, the entropy of the $\beta\,(4 \times 3)$ reconstruction is well below that of the noninteracting system, with inflection points where 2, 5, and 6 of the 7 anion sites are occupied with Bi (X_{Bi}=0.286, 0.714, and 0.857) corresponding to the $\beta\,(4 \times 3)$-2, -5, and -6 groundstates. Thus at -60°C, the surface is ordered, with much of the Monte Carlo surface matching the groundstate primitive cell, while the configurational ordering in the surface sites produces the observed deviation from the entropy of ideal mixing. At 60°C, the inflection points are much less pronounced, indicating a more random filling of sites. A slight amount of ordering from the $\beta\,(4 \times 3)$-2 and -6 configurations still exists, but the $\beta\,(4 \times 3)$-5 configuration has virtually disappeared. Hence, it can be concluded that the surface disorder has set in well below typical ex-

perimental MBE temperatures. At 440°C, the corresponding entropy approaches but is still well below that of ideal mixing. This difference occurs because the temperature is not infinite and residual correlation between sites preventing random occupancy. From this we can conclude the $\beta\,(4\times3)$ reconstruction has a strong tendency for compositional fluctuations on the anion sublattice, with a breakdown in order occurring below ≈100°C. Thus, a well-ordered experimental STM image of the (4×3) surface is unlikely.

4.5 Comparisons to Experiment

The simulation results help explain the experimentally observed surfaces of Ch. III. Deposition of Bi onto either the $\beta2\,(2\times4)$ or $c\,(4\times4)\,\alpha$ surface resulted in a $(n\times3)$ surface. From the phase diagram of Fig. 4.3(a), it is clear why this occurs. The (4×3) reconstruction is stable over both GaAs starting surfaces as μ_{Bi} rises upon depositing Bi. Especially in the $c\,(4\times4)\,\alpha$ case, Bi deposition also accompanies a reduction in μ_{As} from discontinuing the low As_4 flux used to maintain that reconstruction. These observations are consistent with the observed ×3 periodicity on the Bi/GaAs surface. Given the ease with which compositional disorder is seen in the Monte Carlo results, it is reasonable that a breakdown of long range order in the [110] can also occur, eliminating the 4× periodicity in RHEED.

Other predictions of the structures and configurations of the surface phase diagram give important insight into the bulk configuration. One of the most troublesome challenges in growing GaAsBi alloys is the incorporation of Bi. Experiments suggest that the highest incorporation of Bi can be obtained by growing on the (2×1) surface.[23] This is consistent with these results, as the (2×1)-2 has a surface concentration of Bi of unity (2 Bi/2 (1×1) surface area, or $N_{Bi}^{XS}/N_A=1$), higher than even the highest Bi concentration on the (4×3) surface (10 Bi/12 (1×1) area, or $N_{Bi}^{XS}/N_A=0.833$). The (2×1) surface reconstruction therefore enables more Bi incorporation, as more

Bi is present on the growth front.

Surface structure also has an effect on not only the amount, but the distribution of Bi atoms in the bulk structure. At extremes in chemical potential, either one species dominates the surface, which is comprised of a single structure and configuration, suggesting a small degree of compositional fluctuations under these conditions. For instance, the Bi rich (2×1)-2 reconstruction maintains long range compositional uniformity even at high temperature according to the Monte Carlo results. Norman *et al.* showed that $GaAs_{1-x}Bi_x$ possesses bulk $CuPt_B$ ordering with a Bi content of up to $x = 0.10$,[24] which was attributed to surface atom dimerization.[81] This is consistent with our results as the (2×1)-2 reconstruction shows long range order and largely unbroken series of Bi-Bi dimers at typical growth conditions. Such a surface is necessary for appreciable bulk ordering to be detected, since different growth conditions result in a fine scale composition modulation has been attributed to the lack of the (2×1) reconstruction during growth.[24]

At intermediate μ_{As} and μ_{Bi}, the (4×3) reconstruction is stable, with many configurations and structures are close in energy. The resulting disorder demonstrated with Monte Carlo simulations leads to a high susceptibility to composition fluctuations and disrupted long range compositional uniformity, making it unlikely that significant bulk ordering could be observed for films grown on these surfaces. The dimers are simply not consistent enough across the surface. Furthermore, the double anion layer termination of the (4×3) reconstruction is not conducive to bulk ordering; the anion dimers must be moved during growth and replaced with cations in order to match the bulk zinc-blende structure. Thus, the more random distribution of As and Bi on the surface at MBE growth temperatures results in less uniform Bi incorporation in the bulk structure as growth continues.

Moreover, non-uniform Bi incorporation has been observed in GaAsBi in the form of Bi clusters.[43, 44] The phase diagram and Monte Carlo results suggest that the

(4×3) reconstruction can induce such clustering. At lower Bi contents ($0.01 < x < 0.019$), Bi next-nearest neighbors (NNN) pairs are observed,[43] consistent with the preferential occupancy of sites 1 and 2 in the $\beta\,(4 \times 3)$ reconstruction. Incoming Ga atoms can bond to the two Bi atoms and form the NNN pairs. Tetramers can develop in the case where there is a non-negligible probability that Bi-Bi dimers form in the next layer. Because the (4×3) surface has a high susceptibility for compositional fluctuations across the surface, this type of clustering is likely.

4.6 Conclusions

Bi/GaAs(001) was investigated using first principles statistical mechanical methods, establishing the phase diagram of the (2×1), $\beta 2\,(2 \times 4)$, $\alpha 2\,(2 \times 4)$, $c\,(4 \times 4)$, and (4×3) reconstructions and their compositional configurations. The (4×3) reconstruction was seen to stabilize on GaAs in the presence of Bi, taking on many groundstate configurations over a wide range of (μ_{As}, μ_{Bi}). The large number of (4×3) configurations is indicative of a disorder-prone reconstruction. Monte Carlo simulations show that the (2×1) reconstruction possesses strong compositional ordering even at typical growth temperatures, indicating strong surface site correlation. In contrast, the disorder in the (4×3) configurations indicates a weakly correlated surface, as evidenced by individual site disordering behavior with increasing temperature.

The predictions of this phase diagram are consistent with the experimentally identified configurations both in Ch. III and previous work. The phase diagram (Fig. 4.3(a)) shows how the (4×3) reconstruction can appear (in a disordered form) upon Bi deposition on either the $\beta 2\,(2 \times 4)$ or $c\,(4 \times 4)\,\alpha$ surfaces. The details of the surface reconstructions, and the configuration of Bi atoms on the surface has several implications for the growth of GaAsBi alloys and may explain the origins of bulk CuPt_B ordering and clustering observed in these systems.

CHAPTER V

Surfaces of GaSbBi(As)/GaSb Films

5.1 Introduction

A number of benefits have been observed when growing III-V-Bi semiconductors with Bi, including smoothing,[52, 53, 56, 57] bandgap reduction,[3, 4, 5, 6, 7, 8, 9] spin-orbit coupling,[15, 16] and preserved electron mobility at the expense of hole mobility.[10, 11, 12, 13, 14] Such properties are promising for creating long wavelength based optoelectronic devices or novel spintronic devices. However, Bi does not readily incorporate into III-V alloys owing to its large size. This has necessitated low growth temperatures and growth rates to achieve appreciable incorporation.[18, 57, 82, 83, 84, 85]

One potential method of alleviating this difficulty is to use a III-V substrate with a larger lattice constant, such as GaSb which has a lattice constant of 6.096 Å. Such GaSbBi alloys grown by liquid phase epitaxy exhibit a bandgap reduction of 40 meV for a $GaSb_{0.996}Bi_{0.004}$ alloy.[17] Given that GaSb already has a smaller bandgap than GaAs, these two factors make GaSbBi a stronger candidate for long wavelength devices than GaAsBi. To date, very little work has been done on increasing Bi incorporation into GaSb. As with GaAs, the tendency of Bi towards surface segregation necessitates low growth temperatures to achieve appreciable incorporation.[86] In that work, the presence of droplets or lack thereof depended on the flux ratios of Ga, Sb,

and Bi. Bi concentrations of 0.2-0.6% were also reported for flat, droplet-free films according to secondary ion mass spectroscopy (SIMS) and RBS.

This chapter is a study of Bi incorporation in GaSbBi as well as the formation and structure of surface droplets as a function of growth conditions. Droplet morphologies and phase segregation are explained in terms of the Ga-Bi phase diagram. Flux ratios of Ga:Sb:Bi are seen to be the controlling parameter in determining the various droplet morphologies and features that are observed. AFM, SEM, and EDS establish the droplet sizes, morphologies, and compositions, with features such as droplet etching, faceting, sub-droplet formation, and phase separation into Ga- and Bi-rich regions. while RBS and XRD were used to determine the Bi concentrations and amount of relaxation in the underlying films. Bi concentrations of up to 12% are observed. It is seen As incorporation is occurring from residual As in the growth chamber. From these measurements, correlations showing Bi and As incorporation are directly related from a strain compensation effect. Thus, these films will be referred to as GaSbBi(As) films in this chapter, where (As) indicates As incorporation from residual background sources.

5.2 Background and Methods

All GaSbBi(As) films were grown on GaSb(001) substrates using MBE. Ga and Bi fluxes were produced as detailed above, while a mixed flux of atomic Sb (Sb_1) and dimeric Sb (Sb_2) was produced from operating the Sb cracker at 900°C.[31] Sample surface oxide desorption was carried out at 520°C according to the pyrometer. 200 nm thick GaSb buffer layers were grown at a temperature of 485°C with Ga and Sb rates of 0.55 ML/s and 0.84 ML/s, respectively, yielding a flat surface with a streaky (1×3) RHEED pattern. Samples were then cooled at 20°C/min to 300°C as measured by the pyrometer, with the Sb flux shut off at ≈425°C in order to preserve the (1×3) RHEED pattern. Otherwise, cooling under an Sb flux results in a (1×5) RHEED

Table 5.1. GaSbBi(As) growth conditions. All samples consist of a 300 nm GaSbBi(As) film grown at a substrate temperature of 300°C on a 200 nm GaSb buffer (except for B-HT, which does not have the 300 nm low temperature film).

Sample Name	Rate (ML/s)			Ga:Sb:Bi Ratio	BEP (10^{-7} torr)			Ga:Sb:Bi Ratio
	Ga	Sb	Bi		Ga	Sb	Bi	
B-HT	0.56	0.83	0	1:1.48:0	3.71	3.63	0	1:0.98:0
B-LT	0.60	0.60	0	1:1:0	4.09	3.63	0	1:0.89:0
AGR-1	0.20	0.20	0.20	1:1:1	1.28	0.43	1.49	1:0.34:1.16
AGR-2	0.80	0.80	0.80	1:1:1	5.38	3.61	4.04	1:0.67:0.75
AGR-3	1.00	1.00	1.00	1:1:1	6.42	4.27	5.55	1:0.67:0.86
BGR-1	0.60	0.60	0.20	1:1:0.33	4.40	2.25	1.54	1:0.51:0.35
BGR-2	0.60	0.60	0.60	1:1:1	4.13	2.30	2.29	1:0.56:0.55
BGR-3	0.60	0.60	1.00	1:1:1.67	4.40	2.25	5.28	1:0.51:1.20

pattern. Further temperature decrease sees a disappearance of the streaky RHEED pattern, giving way to droplets (spotty or no RHEED pattern) or polycrystalline Sb (rings in RHEED pattern). Upon reaching 300°C, 300 nm GaSbBi(As) films were grown in two different series of experiments, with the experimental conditions for each sample given in Table 5.1 and the resulting droplet coverages, Bi and As concentrations, and percentage of film relaxation given in Table 5.2.

The first series was a comparison of growth rates (absolute growth rate (AGR) series), with films grown at 0.2, 0.8, and 1.0 ML/s while maintaining a constant estimated ratio of Ga:Sb:Bi growth rates at 1:1:1 ML/s, where the growth rate is Ga-limited. Ga and Sb rates were determined via RHEED oscillations, while Bi rates were estimated according to the desorption method outlined in Sec. 3.2. The second series of samples were a comparison of flux ratios (Bi relative growth rate (BGR) series), grown at a constant rate of 0.6 ML/s, with Sb and Ga flux held constant; only Bi flux was varied. In all samples, the Sb flux was set to be less than the Ga flux, reducing Sb availability in order to promote Bi incorporation. All films were nominally 300 nm thick, after which the sample was quenched under no overpressure

Table 5.2. Ga and Bi droplet coverages (θ_{Ga}, θ_{Bi}), Bi and As concentrations (as measured by RBS and XRD, respectively), and % relaxation of the GaSbBi(As) films.

Sample Name	Coverage		% Bi (RBS)	% As (XRD)	% Relax
	θ_{Ga}	θ_{Bi}			
B-HT	0	0	0	9.0	19
B-LT	0.34	0	0	4.3	58
AGR-1	0.42	0.26	6.0	4.2	58
AGR-2	0.14	0.15	2.0	2.3	89
AGR-3	0.03	0.22	8.0	7.6	62
BGR-1	0.03	0.02	10.0	8.9	62
BGR-2	0	0.11	10.0	7.7	44
BGR-3	0.02	0.38	12.0	9.3	54

and removed from the vacuum system. AFM, SEM, and EDS of each sample was done to determine surface morphology and composition maps, from which droplet coverage and height information were established. RBS measurements were done to determine Bi concentration in the GaSbBi(As) film with 2 MeV He^{++} ions at a normal incidence ($\alpha = 0°$), with a reflection angle of $\beta = 20°$ and a scattering angle of $\theta = 160°$ (see Fig. 2.8 for the angle definitions). The simulation program SimNRA was used to simulate the RBS spectra.[33, 34] Residual As concentration was not resolvable in RBS owing to its similar mass to Ga; instead, HRXRD rocking curves were taken for the (004) and (224) reflection of each sample at azimuthal angles of 0°, 90°, and 180°. Using the Bi concentration obtained with RBS, As concentration and film relaxation were calculated using Bragg's Law and the rule of mixtures (Sec. 2.5.1, Eqs. 2.1 and 2.2) based on the film peak positions in the samples. This was implemented in the PeakSplit program of the Bede D1 HRXRD system.

5.3 Results

5.3.1 Bare GaSb growths

Two GaSb(As) buffers were grown for comparison to the GaSbBi(As) films. The B-HT sample was grown to obtain the 200 nm high temperature buffer layer surface morphology before the GaSbBi(As) films were grown. The AFM of the surface (Fig. 5.1(a) reveals a typical layer-by-layer surface with terraces, with some surface cracks that suggest the film is strained in tension. The second GaSb(As) sample (B-LT) had an additional 300 nm of GaSb(As) grown at 300°C and with Ga and Sb rates of 0.6 ML/s each for comparison with the same films grown with a Bi flux. AFM of the surface shown in Fig. 5.1(b) reveals the surface is covered by droplets that formed during the low temperature film growth, as corroborated by the disappearance of the (1×3) RHEED pattern. EDS of the droplets confirms these droplets are completely composed of Ga and cover 34% of the GaSb(As) surface.

HRXRD (Fig. 5.1(c) of the B-HT sample shows a broad diffraction peak at 148.5 arcsecs higher than the substrate peak, indicating a lattice parameter contraction of the film compared to that of the substrate, causing a tensile strain on the film and in turn the observed cracking. This is attributed to residual As incorporation from background sources in the MBE chamber, with the As concentration of this film calculated to be 0.9%. XRD of the B-LT film (Fig. 5.1(c) shows two high angle peaks, one of which is at the same position as the B-HT peak, and a higher angle peak at 524.0 arcsecs. In this case, the As concentration increases to 4.3% owing to the lower Sb flux and lower temperature conditions used in growing the B-LT film, which result in reduced site competition with Sb and reduced As desorption. RBS (Fig. 5.1(d)) of the B-HT sample with sharp Ga and Sb leading edges and flat energy plateaus, typical of well-behaved RBS. In contrast, RBS of the B-LT sample is not well behaved as indicated in the rounded Sb plateau and lack of a distinct leading

edge; this is attributed to the Ga droplets on the surface and the effect this has on the incoming He^{++} ions. As modeled in the inset of Fig. 5.1(d), some of these ions are incident on the bare film, resulting in the dashed spectrum in Fig. 5.1(d). The rest will impinge on the Ga droplets prior to penetrating into the underlying film, which are round and thus of non-uniform thickness.

This results in a distribution of He^{++} energy losses, and thus a distribution of He^{++} energies from the droplets and the underlying film. The RBS spectrum of the droplets is computed using Matlab code (recorded in Appendix C) to sum the coverage-weighted RBS spectra of a pure Ga slab at many thicknesses, which are determined from the height information of the AFM data. Accordingly, the RBS spectra of the underlying film shifts towards a lower backscattered ion energy, the magnitude of which depends on where the ion is incident on the Ga droplet. Adding the droplet and underlying film spectra results in the dash-dotted green line denoted as Ga/GaSb(As) in Fig. 5.1(d). The total spectrum (solid gray line in Fig. 5.1(d)), then, is the summation of the bare GaSb(As) and Ga/GaSb(As) spectra. Again, the residual As does not appear in either spectra as the mass resolution is insufficient to distinguish the As and Ga signals.

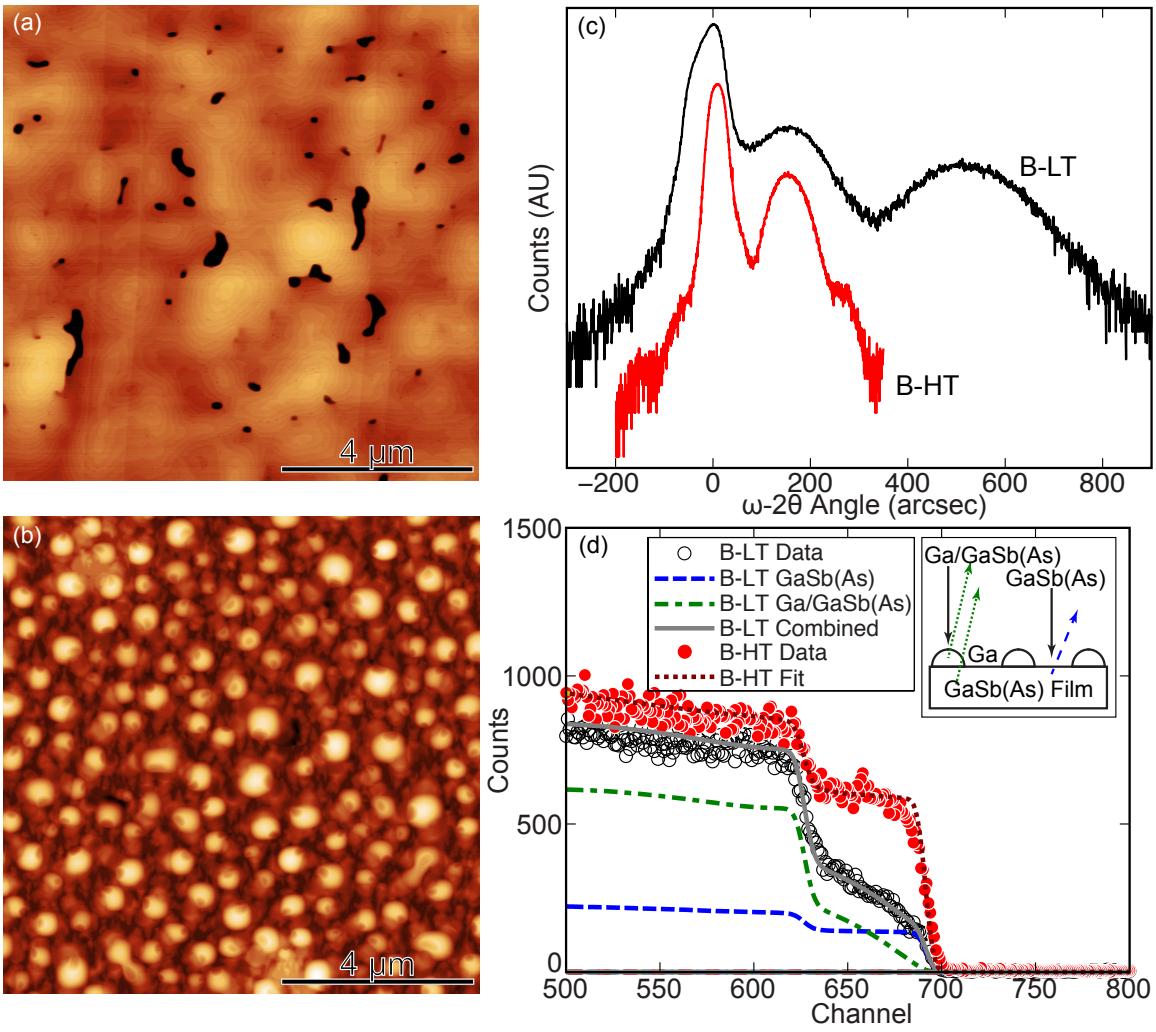

Figure 5.1. AFM of the reference GaSb(As) films (a) after 200 nm of growth at (485°C) (B-HT) and (b) after 300 nm of low temperature (300°C) growth (B-LT). (c) HRXRD of the GaSb(As) samples, where high angle peaks are caused by As concentrations of 0.9% in the GaSb buffer (148.5 arcsecs) and 4.3% in the low temperature layer (524.0 arcsecs). (d) Experimentally observed and simulated fits of the RBS spectra of the GaSb(As) films. Inset in (d) is a model of the He^{++} ion backscattering.

5.3.2 Absolute Growth Rate (AGR) Series

Turning now to the GaSbBi(As) samples, the AGR series will be discussed first. The SEM image of Fig. 5.2(a) shows the surface of a 300 nm GaSbBi(As) film grown at 0.2 ML/s (AGR-1). Several droplets are seen, and are of an irregular shape. Regions of distinct contrast are also seen, with clearly delineated boundaries, suggesting the droplets consist of more than one phase. Moreover, many small sub-droplets on the

larger droplets are visible, which appear as brighter regions in the secondary electron image. Increasing the absolute growth rate of all species to 0.8 ML/s (AGR-2) results in GaSbBi(As) film with large ($> 1\mu$m in diameter), biphasic, hemispherical droplets with clear delineation of phase boundaries as seen in Fig. 5.2(b). No sub-droplets or faceting are observed. The same GaSbBi(As) film grown at 1.0 ML/s for all species (AGR-3, Fig. 5.2(c)) has a surface similar to AGR-1 in Fig. 5.2(a), except only the larger droplets are seen, and no distinct phase separation is seen.

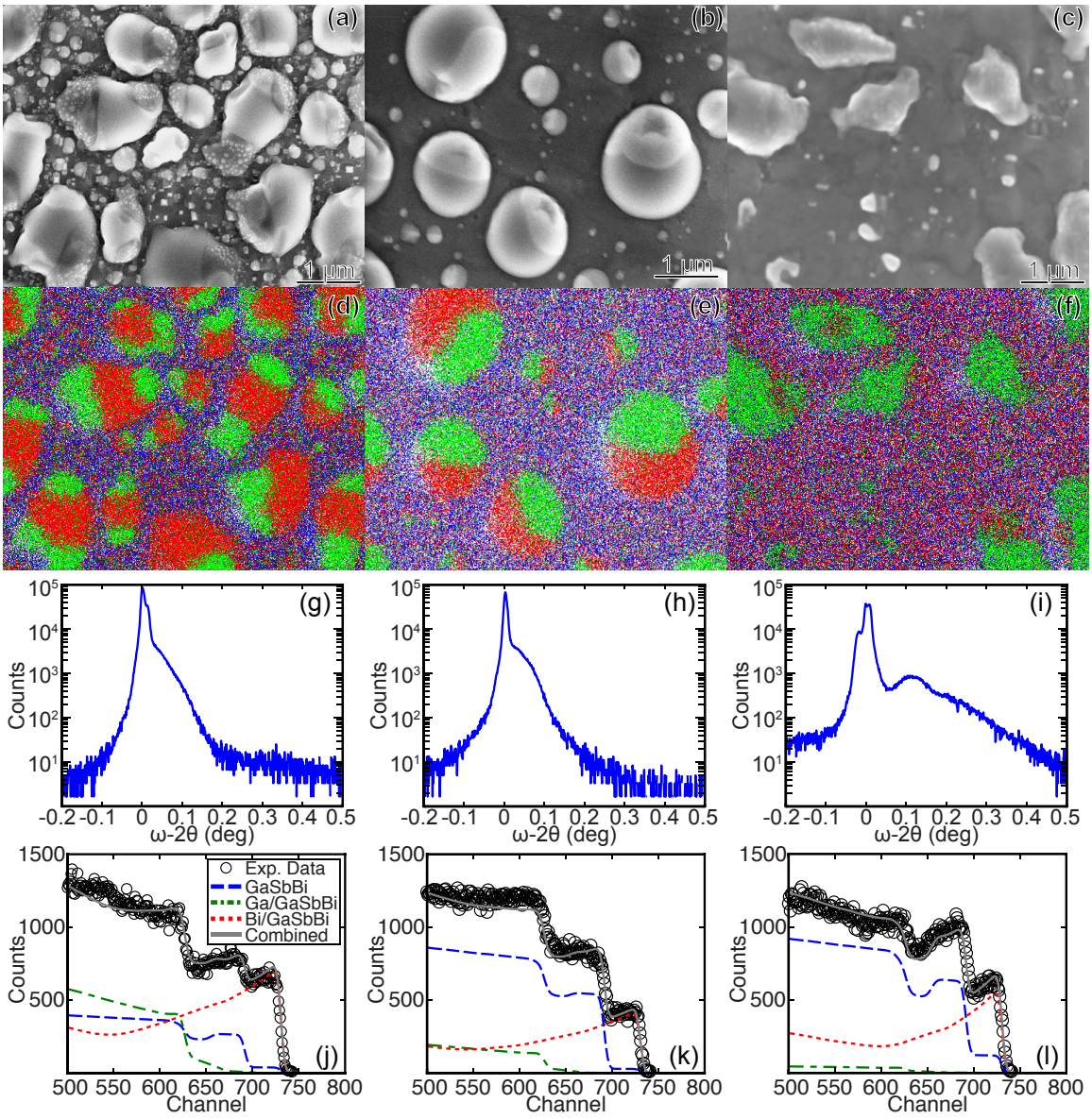

Figure 5.2. SEM (a-c) and EDS (d-f) of the AGR sample surfaces. In the EDS, Ga (red) and Bi (green) are concentrated in the droplets, while Sb (blue) is only in the film. XRD (g-i) and RBS (j-l) of these films.

Plan-view EDS measurements of all three surfaces (Fig. 5.2(d-f)) show the droplets consist of Ga (red) and Bi (green), but no Sb (blue), consistent with the lack of As in similar droplets observed on GaAsBi surfaces.[87, 88] This phase separation arises during quenching, as seen in the Ga-Bi phase diagram constructed by Girard *et al.*,[89] which shows Ga and Bi are miscible liquids at the growth temperature of 300°C. In

the case of Bi-rich droplets, as the sample cools below the melting point of Bi of 271°C, Bi will solidify first into its rhombohedral structure, causing Ga-rich liquid to segregate out from the crystallization front. As cooling continues, the rejected liquid becomes more Ga rich, and will eventually reach the eutectic point at ≈55% Bi and 193°C. Below that point, the system enters another liquid + orthorhombic two phase region, causing the solidifying Bi to reject out much more Ga, which in turn causes the liquid phase Bi concentration to drop from ≈55% to ≈12%. In the final stage of solidification, the liquid becomes more Ga-rich as it approaches the eutectic point at 30°C, whereupon the almost entirely Ga liquid finally solidifies into the orthorhombic crystal structure. Below this eutectic point, orthorhombic Ga and rhombohedral Bi have no mutual solubility.

At more intermediate droplet compositions (≈12-55% Bi on the Ga-Bi phase diagram), the droplet system is above the miscibility gap, which causes two liquid phases L1 (Ga-rich) and L2 (Bi-rich) to form during the initial stages of quenching. As cooling progresses, the L2 phase becomes more rich in Bi, until it reaches the same eutectic composition and temperature (55% at 193°C) as above, whereupon the same sudden rejection of large amounts of Ga into the liquid phase occurs as before, when the system enters the liquid + rhombohedral two phase region. During all of these L2 related phase transformations, the L1 phase simply becomes increasingly Ga-rich, until it becomes the sole liquid phase below 193°C. The droplet system then follows the same solidification process as above.

Thus, regardless of how Bi-rich the droplets are during growth, the same phase separation will occur upon cooling into the liquid + rhombohedral two phase region. This is due to the lack of liquid Ga and solid Bi solubility, which causes the liquid to become almost entirely Ga during the cooling process, and the low Ga melting point, which always forces Ga to solidify only after the segregation is complete. The distinct phase boundaries are likely a product of the sharp increase in Ga concentration in

the liquid phase when the droplet system enters the liquid + rhombohedral two phase region. This results in a sudden change in the solidifying material, which is clearly distinguished in the SEM. However, the sample is only quenched to 200°C in the MBE chamber, just above the eutectic point at 193°C, meaning the Ga-rich regions of the droplets are still liquid before removal from the MBE chamber, and the phase transitions and solidification occurs *after* the sample is removed from the chamber. This transfer time also allows for the remaining liquid to homogenize, reducing or eliminating any composition gradients that might exist at the solidification front.

With the analysis of the Ga-Bi phase diagram in hand, the implications of the EDS is clearer. In AGR-1, droplets cover a total of 68% of the surface, where Ga and Bi in the droplets cover 42% and 26% of the surface, respectively. Bi segregates to opposite ends of the droplets, and the small sub-droplets are too small to be resolved in the EDS map. Since there is more Ga than Bi in the droplets, the droplets likely entered the L1 + L2 region. The Bi solidified below 193°C, Ga was suddenly ejected from the solid Bi, which formed the sub-droplets in an effort to accommodate the rapid change in composition. It should also be noted the large undercooling creates a large thermodynamic driving force for nucleation of smaller Bi or Ga droplets to accomplish segregation more quickly. In AGR-2, surface droplets cover a total of 29% of the surface area, where Ga and Bi comprise 14% and 15% of the surface coverage, respectively, placing the droplet system near the eutectic composition of liquid Ga-Bi. As such, the droplets did not form either the L1+L2 miscibility gap or in the liquid+rhombohedral two phase regions. Thus, the droplet formation solidified in a similar manner to the L2 phase in sample AGR-1, that is, the Bi solidified well before the Ga, causing the observed clear phase segregation. Finally, in AGR-3, the droplet total areal coverage is 25%, with Ga and Bi covering 3% and 22% of the surface area, respectively. Since these droplets were almost entirely liquid Bi during growth, the solidification followed the first case given above, and the Ga segregation occurs, but

the boundaries are not very distinct simply because there is little Ga in the droplets to form a clear contrast between the two phases.

Now the faceting can be explained with the SEM and EDS data. One potential explanation is that upon cooling to room temperature, the liquid Ga solidifies into its solid orthorhombic crystal structure, which may create a large strain mismatch between the solid Ga and Bi regions in each droplet, in turn creating the driving force for the observed facets to relieve the strain. Another explanation is that pure Bi forms facets in its solid form. Both of these mechanisms may be operating simultaneously, but it is possible to determine which is predominant. Figure 5.3 is a high resolution SEM scan of the same area of AGR-3 shown in Fig. 5.2(c) with several facets pointed out with arrows. With only 3% of the area covered with Ga, and such that these Ga-rich regions are not near the facets, this rules out the first explanation. Thus, the facets arise from the tendency of Bi to form facets upon solidifying, not from strain. Moreover, the sub-droplets are more easily seen in Fig. 5.3, which are usually on some but not all of the droplet surface. This suggests the regions with the sub-droplets solidify *after* the ones without. Since the sub-droplets appear when cooling below 193°C, any Bi in the droplet that has already solidified before this will be free of sub-droplets.

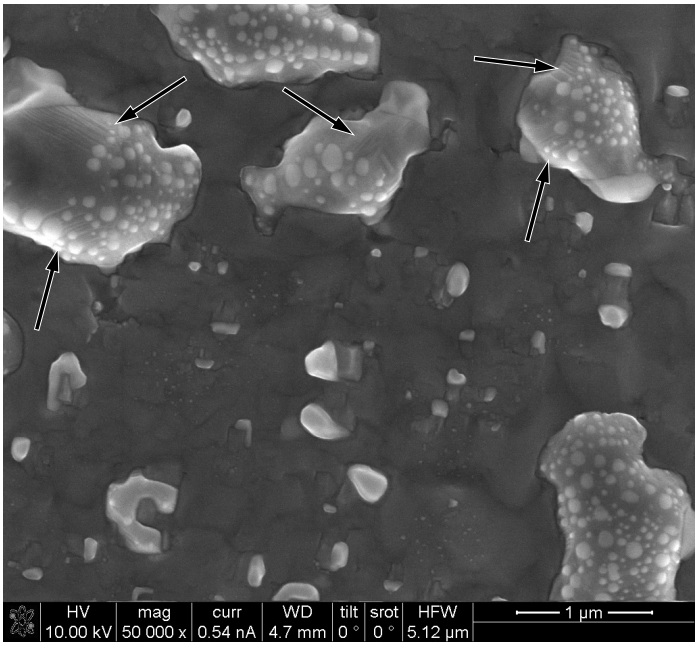

Figure 5.3. High resolution SEM image of the surface area of AGR-3 shown in Fig. 5.2(c). Facets are indicated with arrows, and do not correspond to the Ga rich regions seen in Fig. 5.2(f).

A cross-sectional SEM view (Fig. 5.4) of a AGR-2 droplet reveals that the droplets etch the substrate, similar to that of Ga into GaAs.[90, 91] This is consistent with the large amount of Ga coverage measured with EDS in Fig. 5.2(e), as pure Bi droplets have not been observed to etch GaAs at these temperatures.[92] The etched region has a smooth interface with the underlying GaSbBi(As) film, indicating the droplet was uniform in composition to effect uniform etching, then phase separated during quenching. From this it is seen the phase separation persists throughout the entire droplet, wherein the two phases form a vertical boundary within the droplet, minimizing the interfacial area between the two phases. This suggests a high interfacial energy between the orthorhombic Ga and rhombohedral Bi solid phases. Moreover, the difference in convexity of the droplet phases at the solid vapor interface are visible, with the Ga-rich phase having a convex surface and the Bi-rich phase having a concave surface. This behavior can be explained from the difference in density between Ga, Bi, and GaSb (5.91, 9.81, and 5.61 g/cm^3, respectively). The denser Bi-rich

phase is held in tension at the interface with the Ga-rich phase and by the underlying GaSbBi(As) film. The droplet buckles inward at these regions to try and relieve the strain. Conversely, the Ga-rich phase is largely unaffected, given the similar densities of Ga and GaSb.

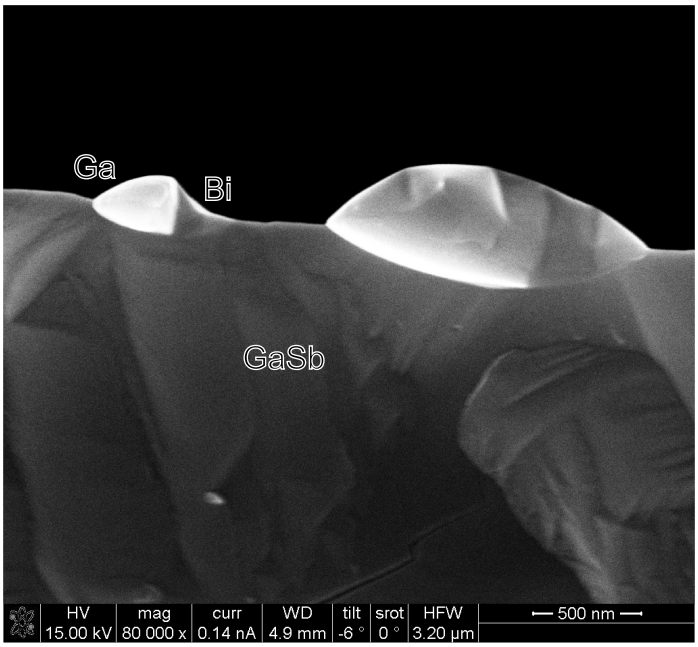

Figure 5.4. Cross-sectional view of AGR-2 droplet etching.

Overall, while the total absolute flux is increasing to achieve the faster growth rate, the droplet coverage on the surface is decreasing, primarily in the reduction of the amount of Ga in the droplets. This is attributed to the increased Sb:Ga and Bi:Ga flux ratios needed to maintain the 1:1:1 ratio of growth rates. This suggests Ga is more likely to form surface droplets on the films, while Bi is more likely to desorb and is less likely to form droplets on it own without Ga. It also appears the droplet morphology can change depending on the relative amounts of Bi and Ga present in them. When one is much more prevalent than the other, the irregular shaped morphology occurs, but when the ratio is $\approx$1, then the rounded morphology exists. The smaller droplets are also eliminated in favor of fewer, large droplets as growth rate increases.

In these samples, the XRD shows that the film possesses a lattice parameter less than that of the substrate. This counterintuitive result has been reported in work on GaSbBi by Song *et al.* and is attributed to Bi-induced vacancy formation in GaSb.[86, 93] However, XRD and RBS analysis show that there is a significant As concentration in these films from the background of the MBE chamber. This would explain the reduction in lattice parameter as GaAs has a smaller lattice constant than GaSb. Neither the Bi nor the As concentrations can be determined from XRD alone, and the effects of film relaxation are also unknown. Therefore, RBS characterization of these films is needed and is shown in Fig. 5.2(j-l).

In AGR-3, the Sb and Bi plateaus show an increase in counts with increasing channel, which cannot be explained with standard RBS simulation with flat films. As with the GaSb reference films above, fitting these spectra requires accounting for the effects of the surface droplets in order to establish the underlying GaSbBi(As) film concentration of Bi independently of As concentration and film relaxation. In this case, the total film spectra is a weighted summation of three components: bare GaSbBi(As), Ga/GaSbBi(As), and Bi/GaSbBi(As). Assuming the nominal GaSbBi(As) thickness of 300 nm, the thickness for the RBS simulations are estimated from height profiles of the droplets taken from AFM and the estimated etching depth. For instance, Fig. 5.4 shows that the droplet etch depth is ≈75% of the height of the droplet above the surface, although this may vary from one droplet to the next. The area coverage of the Ga and Bi droplets measured with EDS above determines the weighting. The agreement between the composite simulated spectra (solid gray lines Fig. 5.2(j-l)) and the experimental data is very good. From the individual Bi/GaSbBi(As) spectra, the contribution from the Bi parts of the droplets govern the slope observed in the Sb and Bi plateaus; steeper slopes are caused by shorter droplets, shallow slopes originate from taller droplets.

With the bare GaSbBi(As), Ga/GaSbBi(As), and Bi/GaSbBi(As) spectra known,

the effects of the droplets can be subtracted out of the composite spectrum, leaving only the underlying film spectrum. From this, the Bi concentration in the underlying GaSbBi(As) film is determined, as recorded in Table 5.2. Despite the steadily increasing absolute flux and growth rate, the amount of incorporated Bi starts at 6% for AGR-1, falls to 2% for AGR-2, then rises back to 8% for AGR-3. The other properties that follows this trend is the amount of Bi in the surface droplets and the Bi:Sb flux ratio (see Table 5.1). From this it is again seen the relative growth rate is a stronger determinant of the final film Bi concentration than the absolute growth rate.

Turning again to the XRD data in Fig. 5.2(g-i) with the Bi incorporation obtained from the RBS simulations, the percentage of relaxation and As incorporation can be calculated (see Table 5.2) using a combination of Bragg's Law and the rule of mixtures (Eq. 2.1 and Eq. 2.2, respectively). From these calculations the As concentration is 4.2%, 2.3%, and 7.6% vs. the Bi concentrations of 6.0%, 2.0%, and 8.0% for AGR-1, AGR-2, and AGR-3, respectively. It appears from these numbers the As and Bi concentrations are directly related. Note also the As concentration increases from 2.3% in AGR-2 to 4.2% in AGR-1 for an increase of Bi concentration from 2.0% to 6.0%. AGR-1 was grown right before AGR-2 on the same day, when both samples should have been exposed to roughly the same amount of background As. Thus, the higher As concentration cannot be due solely to an increase in residual As over time from growing As-containing samples. Instead, Bi encourages As incorporation, likely from a strain auto-compensation effect that improves lattice matching to the GaSb substrate and relieves the mismatch strain.

5.3.3 Relative Bi Growth Rate (BGR) Series

The trends in the AGR series suggest the relative growth rates are a stronger determinant of the droplet morphology and film concentrations. Three GaSbBi(As)

films were grown at fixed Ga and Sb rates of 0.6 ML/s as a function of relative Bi growth rates of 0.2 ML/s, 0.6 ML/s, and 1.0 ML/s, labeled BGR-1, BGR-2, and BGR-3 respectively, in Tables 5.1 and 5.2. SEM of these surfaces are shown in Fig. 5.5(a-c), where the droplet density is much lower than for the AGR series, except for BGR-3. In all three cases, several droplets dot the surface, whose sizes vary solely according to the relative Bi:Ga flux. In BGR-1, several small droplets ≤ 1 μm are present (Fig. 5.5(a)). Upon increasing the Bi rate in BGR-2, fewer, larger droplets form (Fig. 5.5(b)). As the Bi rate is increased further to 1.0 ML/s (BGR-3), large irregularly shaped droplets 2-3 μm in size cover the majority of the surface area, and sub-droplets are observed (Fig. 5.5(c)). Fig. 5.5(d-f) shows EDS maps of the same three surfaces, and as with the AGR-1 and AGR-3, the droplets are primarily composed of Bi with smaller amounts of Ga present.

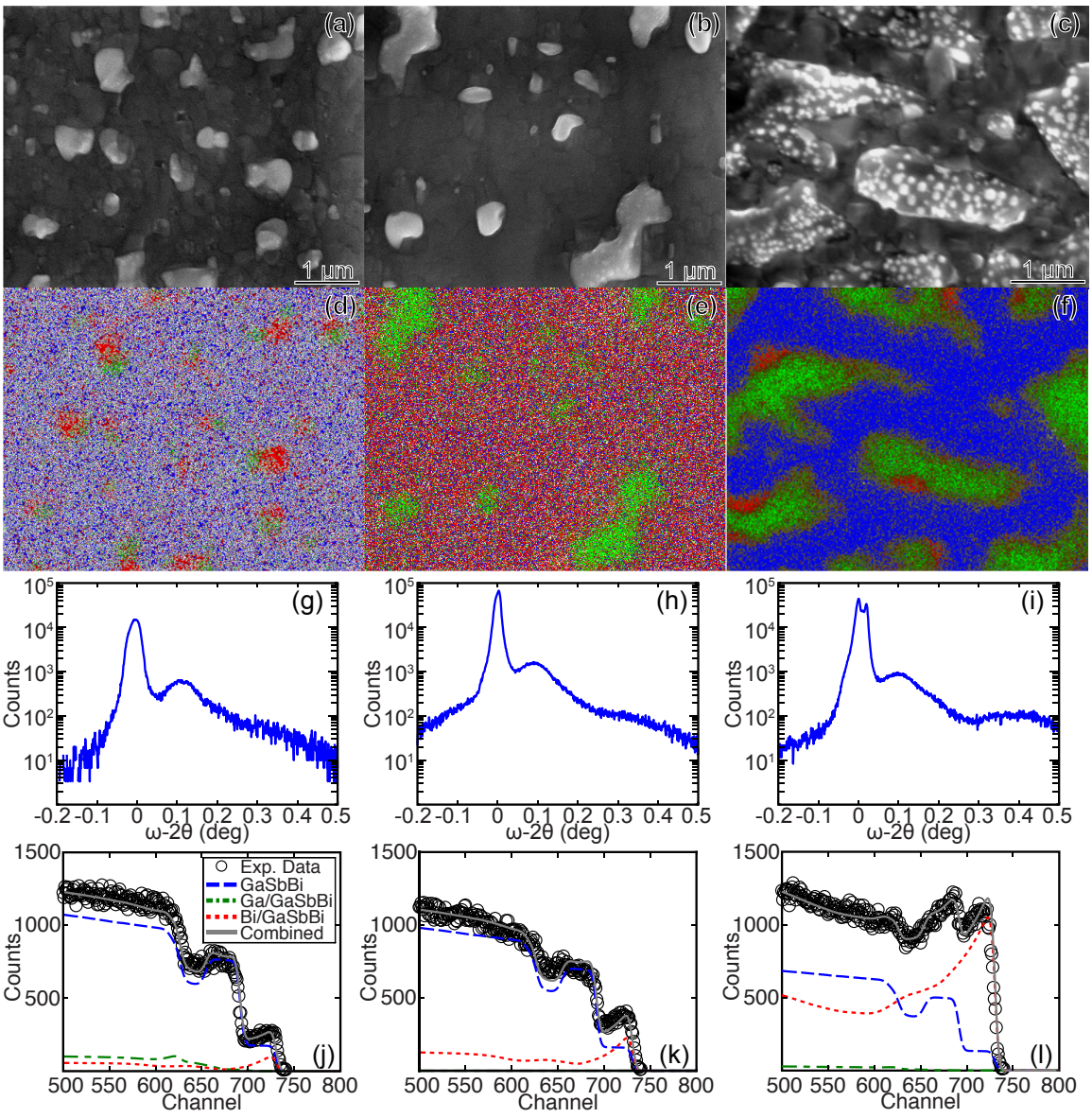

Figure 5.5. SEM (a-c), EDS (d-f), XRD (g-i), and RBS (j-l) of the BGR surfaces.

HRXRD $\omega - 2\theta$ scans of each sample (Fig. 5.5(g-i)) show high angle peaks for each BGR sample, indicating a film lattice contraction as before. Thus, concentrations are determined again with a combination of HRXRD and RBS. RBS spectra of the BGR series of growths are shown in Fig. 5.5(j-l). In BGR-1 (Fig. 5.5(j)) and BGR-2 (Fig. 5.5(k)), the Sb plateau has two tiers within the plateau, a lower one at lower energy and a higher one at higher energies. In BGR-3 (Fig. 5.5(l)), the Sb and Bi plateaus show the same behavior as shown in the AGR series, each increasing in counts

with increasing channel. In BGR-1, the area coverage θ_{Bi} is the lowest of the BGR series at only 2% of the surface area. Likewise, the RBS signal of just the Bi droplets (not the whole Bi/GaSbBi(As) spectrum) is lowest for BGR-1 (Fig. 5.5(j)) and does not extend into the energy range of the Sb plateau. Thus, the higher tier seen in the Sb plateau arises from the Bi signal from the bare GaSbBi(As) film (dashed blue line in Fig. 5.5(j)), where the Bi concentration is calculated to be about 10%. Sample BGR-2 (Fig. 5.5(k)) shows a similar two-tiered Sb plateau; Bi concentration is also 10%. In the BGR-3 sample (Fig. 5.5(l)), the droplets are much larger, covering 38% of the surface, somewhat masking the second Sb tier in the RBS spectra, but after accounting for the droplets, the Bi concentration of the underlying GaSbBi(As) film is 12%. Qualitatively, it is clear increasing the relative Bi growth rate for these Ga and Sb rates (0.6 ML/s) increases Bi concentration until a certain saturation point is reached, after which the excess Bi simply forms into bigger droplets.

This trend is also supported by the AGR series. The increase in Bi:Sb and Bi:Ga flux ratio between AGR-2 and AGR-3 corresponds to a 6% increase in Bi concentration but only a 7% increase in θ_{Bi}. A plot of θ_{Bi} as a function of flux ratios for all the GaSbBi(As) films is shown Fig. 5.6. Changes in the Sb:Ga ratio have little effect on θ_{Bi}. On the other hand, Ga droplet coverage is rather low in all the GaSbBi(As) samples studied here, with two notable exceptions. The first, AGR-1, has a Ga coverage of 42%, which can be explained by looking at the measured fluxes. Even though Ga and Sb have a rate of 0.2 ML/s, the Sb flux (0.43×10^{-7} torr) is much less than the Ga flux (1.28×10^{-7} torr) for this sample than any other presented here. This Sb starvation prevented Ga atoms from incorporating into the film, causing the excess Ga to form into droplets. The second outlier, AGR-2, has a Ga coverage of 14%, but had much more incoming Sb relative to Ga during growth than AGR-1, eliminating Sb starvation as a possible cause, but the appearance of a round, hemispherical morphology and the low Bi concentration in the film suggest the flux ratio was such that

the final ratio of Bi:Ga on the surface was ∼1, as evidenced by the near equality of Ga and Bi droplet coverages. This combination seems to favor accumulation of Ga and Bi into the droplets, preventing these atoms from incorporating into the film.

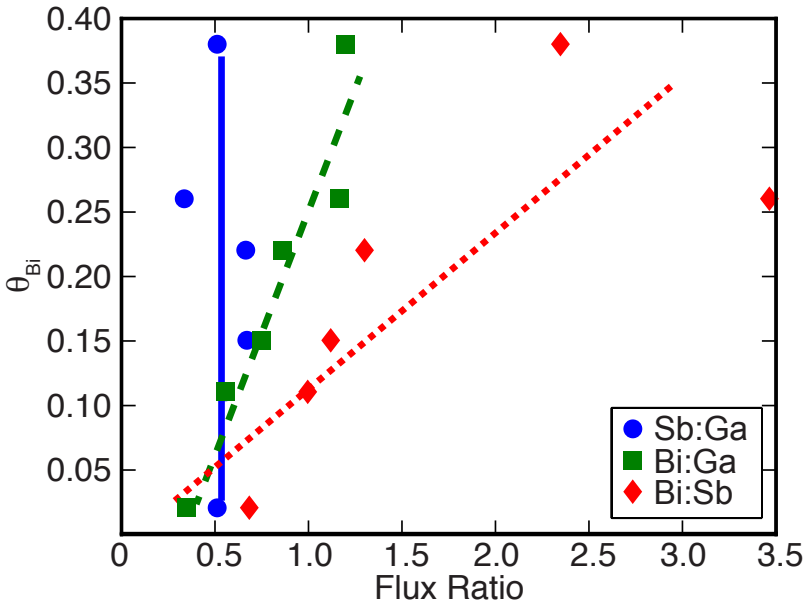

Figure 5.6. θ_{Bi} vs. measured BFM flux ratios for all the GaSbBi(As) films grown in this study. Lines drawn for each series are only guides for the eye.

Now the As concentration and percent strain relaxation (listed in Table 5.2) in the GaSbBi(As) films may be determined from the HRXRD data shown in Fig. 5.5(g-i). Fig. 5.7 shows a plot of the Bi concentration as a function of As concentration for all of the samples studied here, and shows that there is a strong correlation between the Bi and As concentrations independent of the growth conditions. In related work, Song et al. present SIMS measurements that also show a concurrent increase in As and Bi incorporation in their GaSbBi films,[86] in agreement with Fig. 5.7. Moreover, as the Bi/As concentration ratio increases, the amount of film relaxation decreases, as also plotted in Fig. 5.7. These results indicate that the lattice contraction observed via the HRXRD measurements, as well as in the work of Song et al.,[86] is a result of As incorporation and the strain auto-compensation effect, not the creation of vacancies.

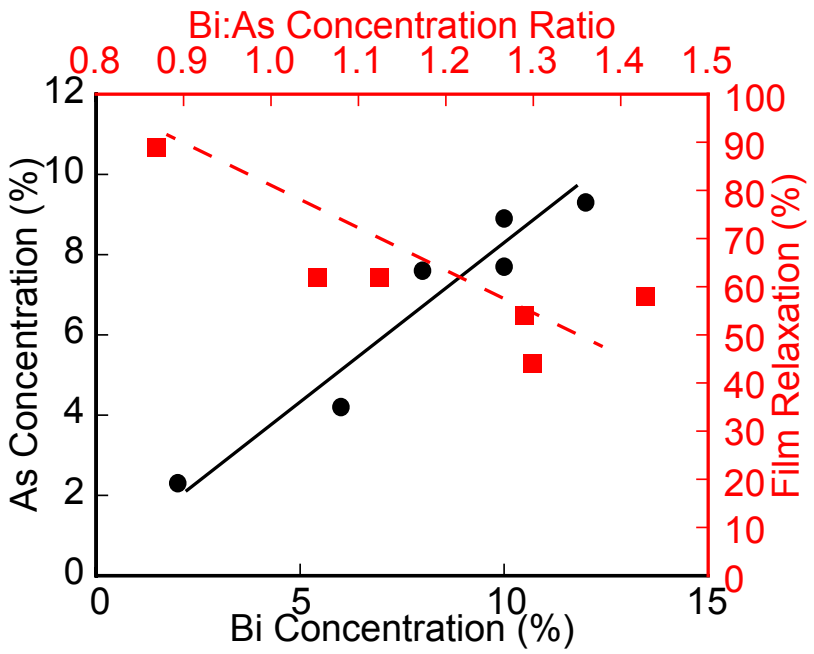

Figure 5.7. As concentration as a function of Bi concentration (black circles, left/bottom axes) and percent relaxation as a function of Bi:As concentration ratio (red squares, right/top axes). Lines are only guides for the eye.

5.4 Conclusion

In this work, several GaSbBi(As) films were grown on GaSb substrates, where controlling relative Bi growth rate appears more desirable for obtaining high Bi concentration films and lower droplet coverages. SEM, AFM, and EDS of the surfaces of these films show droplet formation, with other features such as phase separation, sub-droplet formation, faceting, and etching into the film. EDS shows the droplets are comprised of Bi and Ga regions, with sharply defined interfaces, caused by the phase separation during solidification as indicated on the Ga-Bi phase diagram. Small sub-droplets form during this process as well, from rejection of Ga out of the Bi regions during quenching. The observed facets appear because of the natural tendency of Bi to form facets, not because of strain effects.

Bi concentration of up to 12% was measured with RBS. High angle peaks in the HRXRD measurements suggest a lattice contraction, contrary to the expected

lattice expansion. These peaks were also observed in GaSb films grown without Bi, suggesting As incorporation from background sources. Using the Bi concentration determined from RBS, As concentration and percentage of film relaxation were measured with HRXRD. Bi and As concentrations show a direct relationship in Fig. 5.7, indicative of a strain auto-compensation occurring from the simultaneous incorporation of lattice-expanding Bi and lattice-contracting As. This is also seen in Fig. 5.7, where strain relaxation decreases as the Bi:As concentration ratio increases. This is contrary to the explanation that Bi causes a lattice contraction from increased vacancy formation.[86, 93] Finally, higher temperature growth of these films eliminates of surface droplets on the film, but also reduces Bi concentration as well. It is also possible the higher Sb overpressures used in these samples prevented Bi incorporation

CHAPTER VI

Calculated GaSb and Bi/GaSb Phase Diagrams

6.1 Introduction

The (4×3) reconstruction family,[61] the (2×4),[94, 95, 96] the (2×8),[97] the $c\,(2 \times 6)$,[29, 98] and the c(2×10) [29] reconstructions have all been proposed to explain STM observations on GaSb. It is reasonable to consider these reconstructions for the GaSbBi surface as well. However, the $c\,(2 \times 6)$ and $c\,(2 \times 10)$ reconstructions have not been shown to be stable on GaSb, often attributed to the violation of the electron counting model (ECM).[28, 29, 98] In those studies, various compositional configurations were tested where Ga was substituted for Sb on second layer Sb sites in an effort to satisfy the ECM. Some of these configurations were energetically more favorable, but not enough to stabilize these reconstructions relative to the (4×3) reconstruction.

Other work by Whitman *et al.* suggests the $c\,(2 \times 10)$ reconstruction is metallic, proposing the $c\,(2 \times 10)$ reconstruction surface energy is low enough to compensate for the violation of the ECM.[30] To date, no rigorous search for the lowest energy configuration of the c(2×10) has been carried out, and a comprehensive map of the stable GaSb surface reconstructions is lacking. Such a deficit must be remedied in order to understand the GaSbBi surface reconstructions. Once the GaSb reconstructions are better understood, the same computational methods can be used to

provide insight to the GaSbBi surface reconstruction, providing useful details on the growth front and possibly suggesting desirable conditions for growing high quality, droplet-free films.

As mentioned in Ch. V, GaSbBi is of interest in fabricating infrared optoelectronic devices owing to its low bandgap. Making higher-quality heterostructure devices requires a sharper interface between successive layers of material. Interfacial sharpness in turn depends upon surface flatness and the reconstruction of the surface atoms during growth, but as seen in Ch. V, such conditions are difficult to accomplish owing to surface droplets. These droplets also mask the underlying surface reconstruction. In order to better understand and optimize GaSbBi growth for potential device usage, the reconstructions must be investigated computationally.

This chapter addresses these two questions by using the cluster expansion formalism to enumerate all the possible configurations of the GaSb reconstructions listed above and predict the groundstates of each. The 0 K phase diagram can then be constructed from this information, and the stability of the GaSb reconstructions relative to one another determined. Once this is established, the various reconstructions can be enumerated to allow for Bi occupancy. The GaSbBi surface phase diagram requires enumerating all the possible Bi_{Sb} site occupations within the slab, vastly increasing the number of configurations needed to do the cluster expansion; hence, the Bi/GaSb surface system is done as a more tractable approximation.

6.2 DFT Simulations

All of the reconstructions named above are considered in this work and are shown in Fig. 6.1. The (2×1) reconstruction is also considered, as it appears in several Bi-terminated III-V surface systems, and will need to be considered for the Bi/GaSb system.[19, 20, 21, 45, 46, 47] Within each of these reconstructions, Ga or Sb can potentially occupy any of the various dimer sites, and in the case of the $c\,(2 \times 6)$

and c(2×10) reconstructions, the second layer sites as well. Again, the distinction between structural and compositional configuration must be clear; the former refers to different reconstructions, while the latter refers to different compositions within each reconstruction. The number of possible configurations with three species scales as 3^N, where N is the number of sites permitted to vary in species occupancy. As such, the number of compositional configurations can get very large. As pointed out in Ch. IV, there are ∼30,000 symmetrically unique configurations exist for just the volume 1 (4×3) reconstruction alone. As with the Bi/GaAs surface system, the cluster expansion formalism must be applied to the present Bi/GaSb surface system.

The cluster expansions were constructed to allow Ga, Sb, and Bi species occupancy in all the sites colored in black in Fig. 6.1, except for the $c\,(2 \times 6)$ and $c\,(2 \times 10)$ reconstructions, which had to be investigated in stages. These two reconstructions were enumerated for Ga and Sb substitution only to establish the bare GaSb groundstates. Then Bi and Sb substitution could be considered separately in the anion sites of these groundstate configurations. When considering both the dimer sites and the second layer sites, the large number of sites for the $c\,(2 \times 10)$ reconstruction results in a large number of configurations, about $2^{18} = 2.62 \times 10^5$. However, volume 2 supercell configurations are needed to obtain $c\,(2 \times 10)$ configurations that satisfy the ECM, vastly increasing the number of configurations to $2^{36} = 6.87 \times 10^{10}$. Hence, the cluster expansion was limited to the second layer sites only in the $c\,(2 \times 10)$ reconstruction, reducing the number of configurations to $2^{16} = 6.55 \times 10^4$. Experimental filled state STM imaging by Whitman *et al.* shows no variation in intensity of the $c\,(2 \times 10)$ reconstruction dimer rows, suggesting no Ga occupation of surface dimer sites, consistent with this cluster expansion setup.[30]

For bare GaSb, both the $c\,(2 \times 6)$ and $c\,(2 \times 10)$ reconstructions have Sb occupying every site in the first and second layers at Sb site fraction x_{Sb}=1, forming a double anion layer. These layers in turn sit on the third layer, which is comprised of Ga atoms.

Therefore, at x_{Sb}=0, the top three layers of these reconstructions consist entirely of Ga atoms, forming a triple cation layer. It is unlikely the cation-rich configurations will be seen; thus, only the $c\,(2 \times 6)$ configurations with $x_{Sb} > 0.6$ and the $c\,(2 \times 10)$ configurations with $x_{Sb} > 0.91667$ were considered. This limits the number of Ga atoms in any $c\,(2 \times 6)$ and $c\,(2 \times 10)$ configuration to a maximum of eight and three, respectively. This was done not so much to pare down the number of configurations as it was to produce a better fit of the semiconducting groundstate configurations. After determining the groundstates for the bare GaSb cases, new cluster expansions were constructed from the groundstates, allowing Bi and Sb occupancy on the anion sites. By restricting the composition in this manner, the GaSb groundstates of the $c\,(2 \times 6)$ and $c\,(2 \times 10)$ reconstructions could be determined that still satisfy the ECM.

The cluster expansion method was again automated using the CASM package.[40, 99] Newer fitting code featuring a direct minimization technique for determining the ECI was used in conjunction with the previous genetic algorithm fitting method to acquire the groundstate configurations.[100] A cluster expansion for each reconstruction shown in Fig. 6.1 was constructed to enumerate all the possible compositional configurations. All DFT relaxations were carried out using the VASP under the LDA with a $12 \times 12 \times 1$ k-point grid and a 200 eV cutoff energy.[37] Slabs were constructed to be 5 ML thick, with the surface reconstruction terminating one face of the slab and a layer of Sb atoms passivated with pseudo-H atoms of 0.75 charge on the other face. Ultrasoft pseudopotentials were used for Ga, Sb, Bi, and pseudo-H.[62]

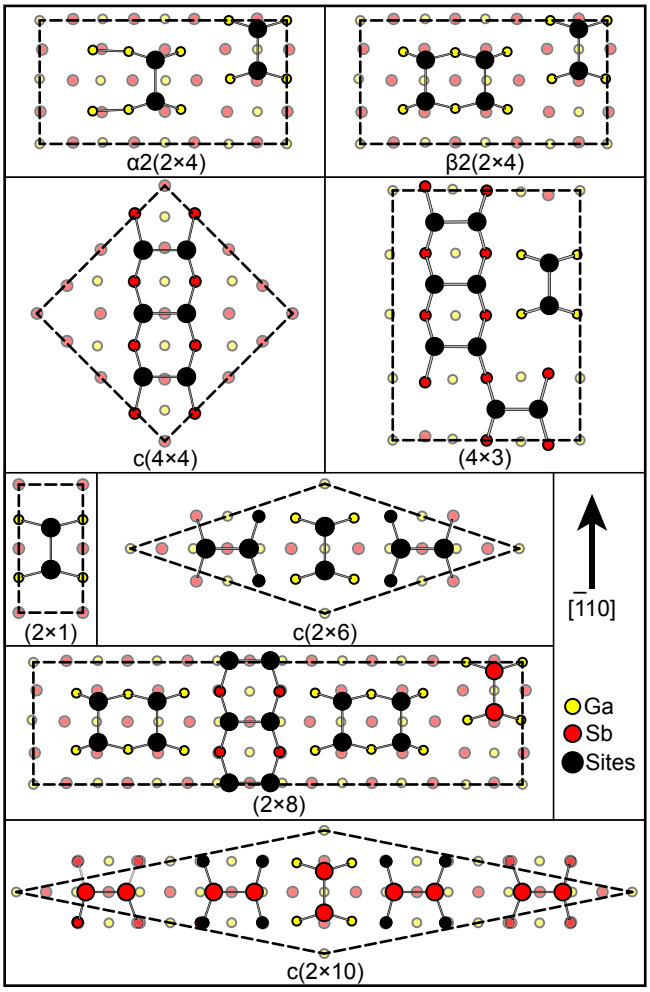

Figure 6.1. Atomic surface structure and arrangement of the surface reconstructions considered. Sites in black indicate where Ga or Sb occupation was allowed.

6.3 Results

6.3.1 GaSb Phase Diagram

The GaSb surface phase diagram is shown in Fig. 6.2. After comparing the energies of the (4×3) configurations with those of the $c\,(2 \times 10)$ reconstruction, it is clear no semiconducting $c\,(2 \times 10)$ configuration is stable, even at high μ_{Sb}. The most stable $c\,(2 \times 10)$ configuration is shown in Fig. 6.3(b), with three Ga_{Sb} anti-site defects present over two $c\,(2 \times 10)$ primitive unit cells, and is denoted as the $c\,(2 \times 10)$-3/2. This configuration satisfies the ECM, but is still ~20 meV/(1×1) area higher

in energy than the $\beta\,(4\times3)$ and $h0\,(4\times3)$ configurations. A single GaSb (2×1) configuration, denoted as the $\alpha\,(2\times1)$ is stable at the Ga-rich side of the diagram, and will be discussed later in light of the Bi/GaSb results. Some of the enumerated $c\,(4\times4)$ and $c\,(2\times6)$ configurations appear within the energy range, but these are higher in energy than the (4×3) configurations by $\sim$20 meV/(1×1) area or more. All of the $\beta2\,(2\times4)$, $\alpha2\,(2\times4)$, (2×8) configurations have much higher surface energies. Interestingly enough, a $c\,(4\times4)$ configuration is closer to stability than the $c\,(2\times10)$-3/2 at $\mu_{Sb}-\mu_{Sb}^{bulk}>-0.07eV$, which is a volume 2 supercell configuration with one Ga atom occupying one of the twelve dimer sites in that configuration. This suggests a semiconducting $c\,(2\times10)$ reconstruction is unlikely, as a semiconducting $c\,(4\times4)$ configuration, which is known not to appear on GaSb,[30] is more stable.

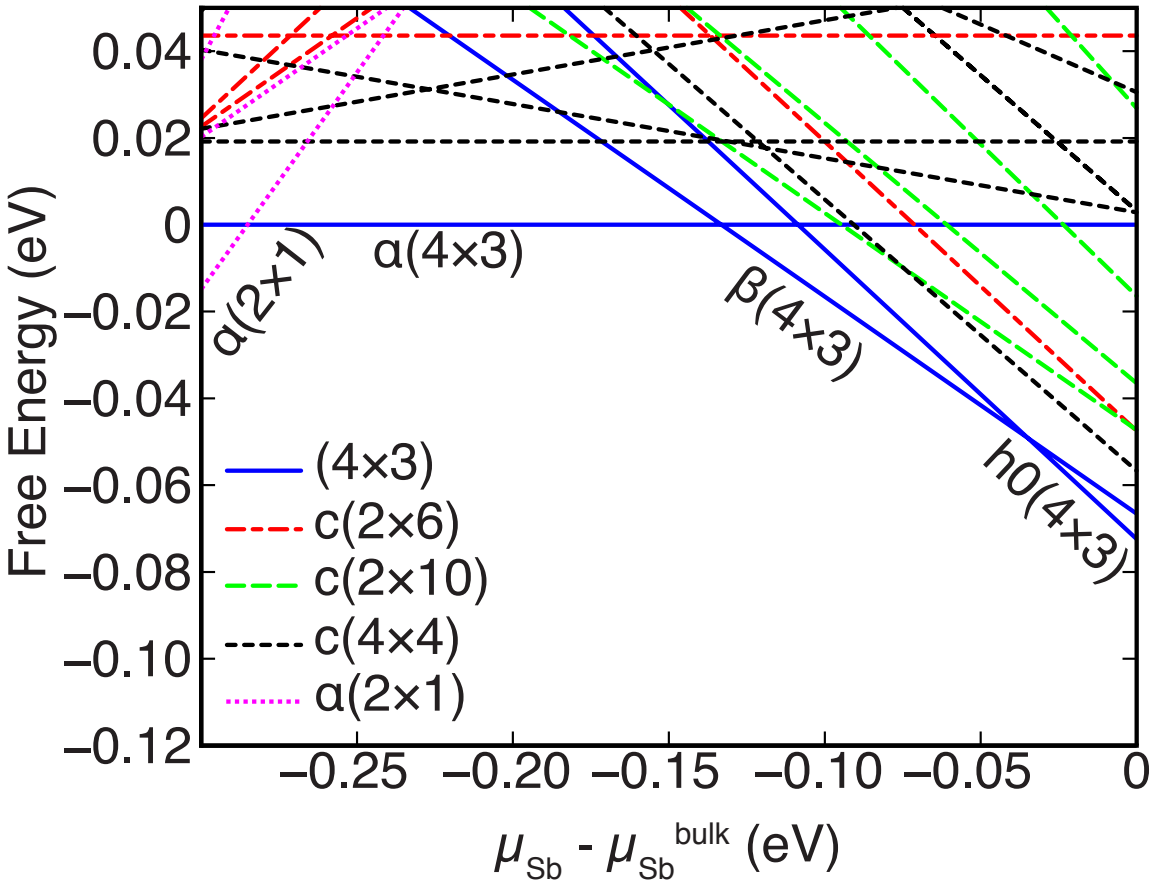

Figure 6.2. GaSb phase diagram of the $c\,(4\times4)$, $c\,(2\times6)$, $c\,(2\times10)$, (4×3), and (2×1) reconstructions. The $\beta2\,(2\times4)$, $\alpha2\,(2\times4)$, and (2×8) reconstructions were not observed within the energy range plotted here.

The $c\,(2\times10)$ configuration shown in Fig. 6.3 shows some similarities with the $c\,(2\times10)$-s1a configuration proposed in other work.[28, 29] That configuration has two Ga_{Sb} anti-site defects over two $c\,(2\times10)$ primitive unit cells, resulting in a two electron surplus and thus does not satisfy the ECM. These anti-site defects are located in the same position as two of the anti-site defects in the $c\,(2\times10)$-3/2 configuration. It is worth noting all the Ga_{Sb} anti-site defects are in a staggered arrangement on the sites between the dimer rows. This can be explained when looking at this arrangement from the side view (Fig. 6.4). At equilibrium, the Ga_{Sb} anti-site defects pull the underlying Ga atoms upwards. As such, the staggered arrangement of the Ga_{Sb} anti-site defects reduces the overall height undulation from this effect. The Ga_{Sb} anti-site

defects cause the charge on that site to become more positive, forming a dipole with the Sb atom in the site across the dimer chain gap. The staggered arrangement tends to balance these dipoles.

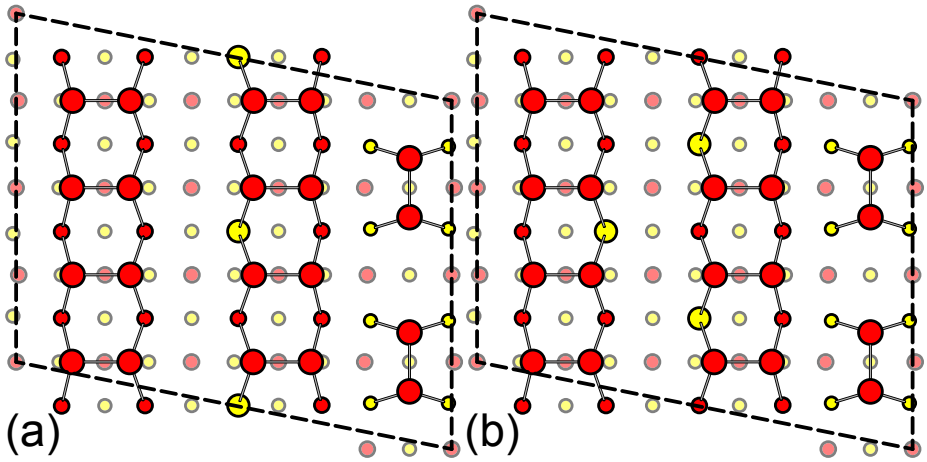

Figure 6.3. (a) Model of the $c\,(2 \times 10)$-s1a configuration. (b) Model of the $c\,(2 \times 10)$-3/2 configuration.

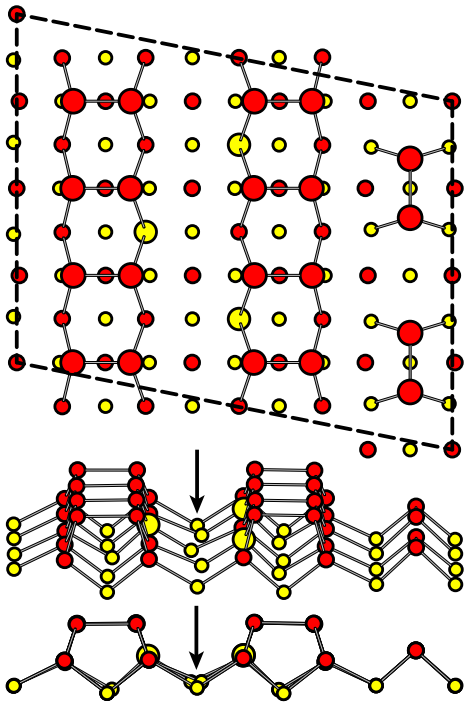

Figure 6.4. Side views of the $c\,(2 \times 10)$-3/2 configuration. Arrows indicate where the underlying Ga atoms the reconstruction sits on are displaced in an alternating fashion within the (001) plane and upwards out of the same plane.

One potential explanation to consider is the $c\,(2 \times 10)$ reconstruction stability might be observed experimentally due to finite temperature entropy effects. If the entropy per (1×1) unit area is high enough, the $c\,(2 \times 10)$ configuration shown in Fig. 6.3(b) may become stable. As a first approximation, the maximum entropy possible is the ideal mixing equation for three Ga_{Sb} over sixteen potential second layer Sb sites,

$$S^{(1\times1)}_{c(2\times10)} = -k_B T \frac{[(3/16)\,log\,(3/16) + (1-3/16)\,log\,(1-3/16)]}{20} \tag{6.1}$$

where k_B is the Boltzmann Constant and T is absolute temperature. The entropy per (1×1) unit area of the $c\,(2 \times 10)$-3/2 configuration at 450°C (723 K), approximately where the $(4 \times 3) \rightarrow c\,(2 \times 10)$ transition occurs,[101] is 1.5 meV, far less than the predicted ∼20 meV difference between the $h0\,(4 \times 3)$ and $c\,(2 \times 10)$ configurations. Moreover, that entropy is for ideal mixing, and will likely be lower for the actual $c\,(2 \times 10)$-3/2 system, making stabilization via thermal effects unlikely. The equivalent entropy calculation for the $c\,(4 \times 4)$ configuration identified in Fig. 6.2 gives 1.1 meV/(1×1) unit area, also too low to stabilize that configuration. Hence, it is possible a metallic $c\,(2 \times 10)$ reconstruction is stable over both of these configurations, in agreement with work by Whitman *et al.*[30] The $c\,(2 \times 10)$ reconstruction becomes metallic again past three Ga_{Sb} anti-site defects over two primitive unit cells, only with an electron deficit instead of a surplus from potentially more Ga_{Sb} anti-site defects than could be enumerated with present methods. Instead, it is shown here from the cluster expansion focused on the semiconducting $c\,(2 \times 10)$ configurations that these configurations are not stable.

6.3.2 Bi/GaSb Phase Diagram

With the stability of the $c\,(2 \times 10)$ reconstruction addressed for the bare GaSb surface, the Bi/GaSb surface system is now considered. While the $c\,(2 \times 10)$ recon-

struction is not stable for bare GaSb, it is within ∼20 meV of the (4×3) reconstruction, about the same energy difference between the (4×3) reconstruction and the (2×4) and $c\,(4 \times 4)$ reconstructions in GaAs.[60]. It is possible Bi may stabilize the $c\,(2 \times 10)$-3/2 configuration via $\mathrm{Bi_{Sb}}$ substitution.

A new set of cluster expansions were constructed for the same reconstructions as in Fig. 6.1. For the (2×4), $c\,(4 \times 4)$, and (4×3) reconstructions, the site substitution is the same as for the GaSb system. The $c\,(2 \times 6)$ reconstruction was eliminated from consideration owing to its instability relative to the $c\,(2 \times 10)$-3/2 configuration and the large number of possible Bi-containing volume 2 supercell configurations. The (2×8) reconstruction was still considered despite its instability, as only primitive cell configurations were needed, and volume 2 supercell configurations were not needed to satisfy the ECM. Finally, a cluster expansion was constructed upon the GaSb $c\,(2 \times 10)$-3/2 configuration as shown in Fig. 6.5. Since that configuration is a volume 2 supercell configuration, all the Bi-containing $c\,(2 \times 10)$ configurations considered here are as well. As such, there are twenty dimer sites. Thus, only Bi and Sb substitution was allowed on the black sites of Fig. 6.5, in order to keep the enumeration tractable. Moreover, the thirteen second layer sites were not considered for substitution for the same reason, where Bi substitution is unlikely owing to the strain effects of inserting a large Bi atom at those sites.

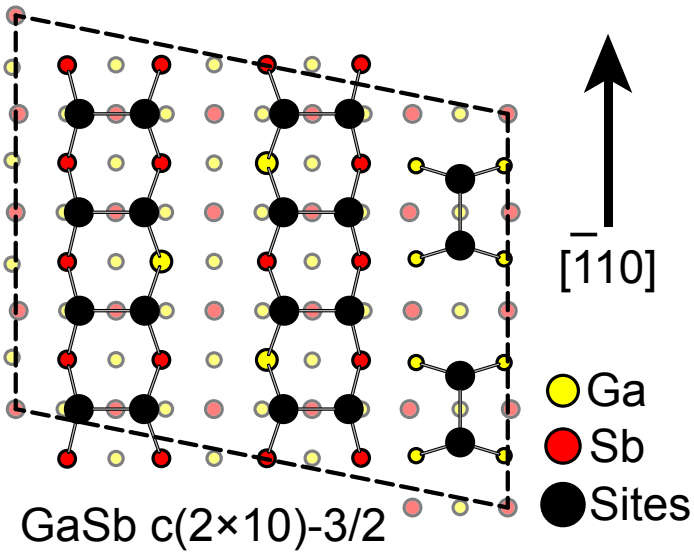

Figure 6.5. Cluster expansion sites of the GaSb c(2 × 10)-3/2 configuration.

The 0 K DFT phase diagram of this system is shown in Fig. 6.6. As with the bare GaSb surface system, only the (4 × 3) reconstruction is stable over most of chemical potential space. A few (2 × 1) configurations are stable in the Bi-rich, Sb-lean corner of the diagram, with the Bi-Bi homodimer configuration having the widest region of stability. This is consistent with the metallic (2 × 1) configuration observed in the Bi/GaAs system.[19, 20, 21, 38] The lone stable bare GaSb (2 × 1) configuration is in the Ga-rich corner, although it is doubtful this configuration is stable since any Ga-rich GaSb surface reconstructions are poorly characterized and could not be included in a cluster expansion. All the stable (4 × 3) configurations are shown in Appendix D.

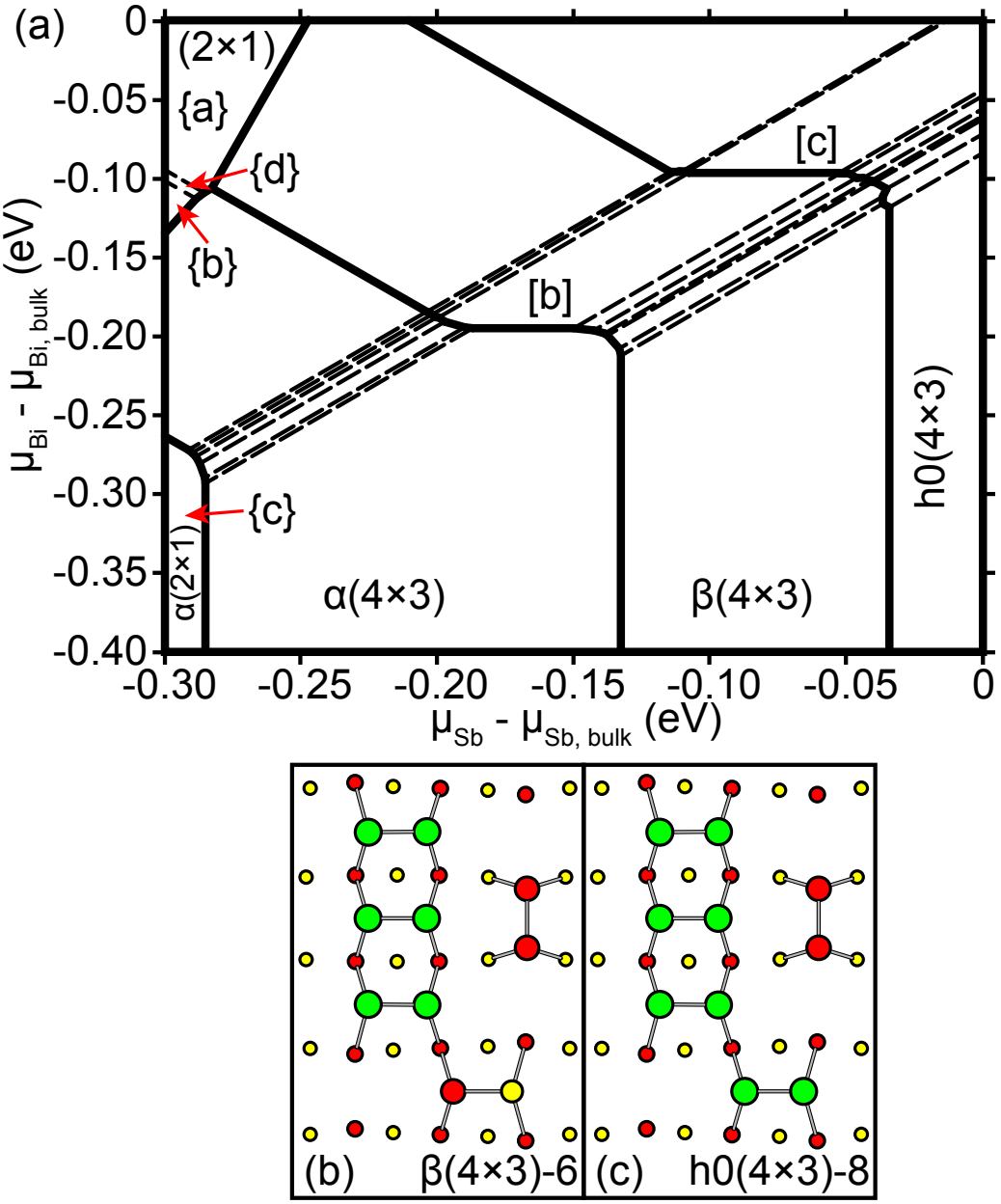

Figure 6.6. (a) Calculated 0 K surface phase diagram of the Bi/GaSb system. (b) $\beta\,(4\times3)$-6 and (c) $h0\,(4\times3)$-8 configurations, both of which have large regions of stability as indicated by [b] and [c]. Letters in curled braces correspond to (2×1) configurations shown in Fig. 6.7.

6.3.3 (2×1) Reconstruction Stability

The (2×1) reconstruction will be discussed first. To date, the (2×1) reconstruction has not been observed for GaSbBi. All the stable configurations are shown

in Fig. 6.7. Its appearance parallels that of the Bi/GaAs system, where work by Laukkanen *et al.* shows this reconstruction often contains Bi-Bi homodimers or Bi-Ga heterodimers.[19, 20, 21] The former configuration results in a metallic surface while the latter results in a semiconducting surface, according to their STS measurements. Often, these two configurations coexisted on the same surface. It is likely that experimental characterization of the Bi/GaSb (2×1) reconstruction would parallel that of the Bi/GaAs (2×1) reconstruction, with separate regions of metallic and semiconducting (2×1) configurations, rather than interspersed as suggested by the cluster expansion.

The appearance of several (2×1) configurations with Bi-Ga heterodimers suggest the cluster expansion is attempting to capture this behavior, although this was not observed on the 0 K Bi/GaAs phase diagram. This can be explained from the difference in strain relief caused by Bi-Bi homodimers and Bi-Ga heterodimers. Laukkanen *et al.* showed Bi-Bi homodimers cause the largest strain relaxation in the (2×1) reconstruction on GaAs than As-As or Sb-Sb dimers.[19] It is possible the Bi-Ga heterodimers did not provide the necessary strain relief to become stable in the Bi/GaAs system, but may have done so for the Bi/GaSb system owing to the larger substrate lattice constant.

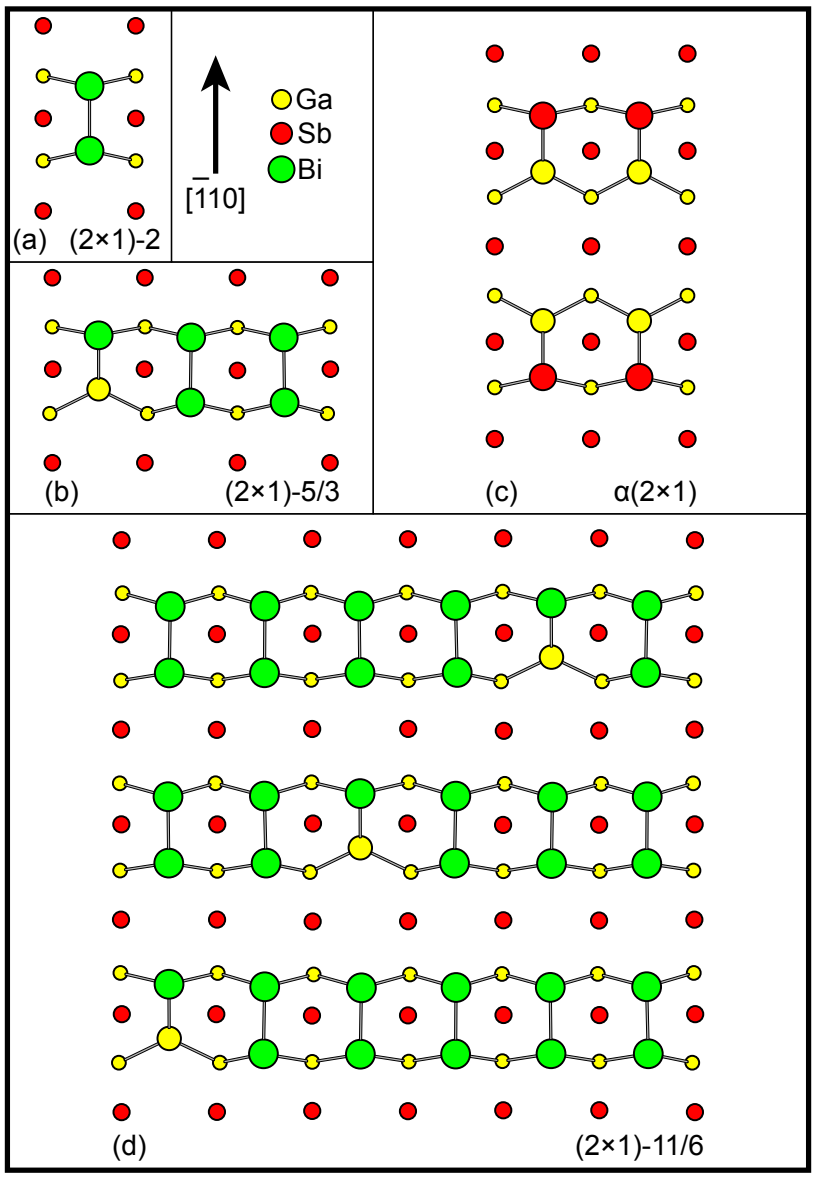

Figure 6.7. Stable (2×1) configurations of the Bi/GaSb phase diagram as denoted by curled braces in Fig. 6.6(a).

6.3.4 (4×3) Reconstruction Stability

Pertaining to the (4×3) configurations, this phase diagram shares several similarities with the Bi/GaAs DFT phase diagram shown in Fig. 4.3. The present Bi/GaSb system tends to have the same preference for site filling order as the Bi/GaAs system, particularly for the $\beta\,(4 \times 3)$ variant, as is seen in Fig. 6.8. The $\alpha\,(4 \times 3)$ and $h0\,(4 \times 3)$ variants are also more prominent than in the Bi/GaAs phase diagram.

Numbers next to the sites in Fig. 6.8 indicate the order of Bi occupancy, with symmetrically equivalent sites possessing the same number, all of which are occupied with Bi before the next site number is filled. Sites with two numbers revert back to Sb as Bi surface concentration increases, owing to the increased strain of neighboring Bi atoms rendering Sb occupation of such sites more energetically favorable. The second number indicates when Bi re-occupies the site as the concentration rises further. Such behavior was not observed in the Bi/GaAs system in Ch. IV as the configurations of the $\alpha\,(4\times3)$ and $h0\,(4\times3)$ variants where this would have occurred were not stable relative to other reconstructions.

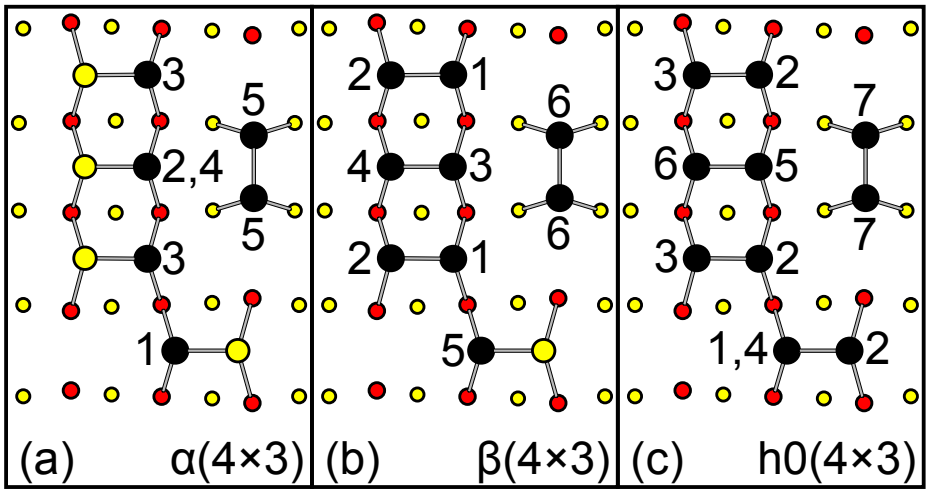

Figure 6.8. Order of Bi site replacement of Sb for the (a) $\alpha\,(4\times3)$, (b) $\beta\,(4\times3)$, and (c) $h0\,(4\times3)$ reconstructions. Sites with the same number must all be filled before the next numbered site may be filled. Sites with more than one number indicate where Sb re-occupancy occurs even as Bi concentration increases.

The spacing of the regions of stability in Fig. 6.6(a) also suggest less surface disorder on the Bi/GaSb surface than for the Bi/GaAs surface. Many of the configurations are very closely spaced, indicating surfaces under these conditions will be highly disordered from thermal effects. Until the three chain dimers are filled in the $\beta\,(4\times3)$-6, the surface concentration fluctuates rapidly with μ_{Bi}. This suggests the chain dimer sites are most preferential for Bi occupation, with only slight preference for Bi occupation between one chain dimer site and the next. Kink dimer sites are the next

most favorable for Bi occupation after the chain dimer sites, with the trench dimer sites being the least favorable for Bi occupancy.

As for the $h0\,(4\times3)$-8, the Bi occupancy preferences are different. The kink dimer sites are energetically more favorable for Bi occupancy than some of the chain dimer sites, filling with Bi atoms before the chain dimer sites do so; all Bi-containing $h0\,(4\times3)$ configurations have a Bi atom in one or both kink dimer sites. In contrast, the $\alpha\,(4\times3)$ configurations are largely unstable at intermediate Bi concentrations, with the order of Bi occupancy suggesting the backbone anion sites are only slightly favorable for Bi occupation more so than the trench dimers.

6.4 Conclusion

Cluster expansions of the $\alpha2\,(2\times4)$, $\beta2\,(2\times4)$, $c\,(4\times4)$, (4×3), (2×1), $c\,(2\times6)$, (2×8), and $c\,(2\times10)$ reconstructions were carried out to determine the most stable configurations for the GaSb and Bi/GaSb surface systems. The $c\,(2\times6)$ and $c\,(2\times10)$ reconstructions were enumerated to volume 2 supercell configurations to allow for full satisfaction of the ECM via $\mathrm{Ga_{Sb}}$ anti-site defects in the second anion layer. DFT simulation of the groundstate configurations shows the (4×3) reconstruction is stable under all conditions of μ_{Sb}, with no stable semiconducting $c\,(2\times10)$ configuration as searched for in other work.[28, 29, 98] The most stable $c\,(2\times10)$ configuration, the $c\,(2\times10)$-3/2, was $\sim$20 meV/(1×1) area higher in energy than the (4×3) configurations. Entropic effects on the surface free energy are insufficient to overcome this difference, suggesting the experimentally observed $c\,(2\times10)$ surface is metallic.

Comparison of the Bi-containing (4×3) and $c\,(2\times10)$-3/2 configurations reveal that Bi occupation does not stabilize the $c\,(2\times10)$ reconstruction. The (4×3) reconstruction is stable over all of μ_{Sb} and μ_{Bi} space, with the exception of high μ_{Bi} and low μ_{Sb}, where the hitherto unreported (2×1) reconstruction is stable. The

(2×1)-2 configuration with Bi-Bi homodimers is the most stable, consistent with the Bi/GaAs phase diagram of Ch. IV. Unlike the Bi/GaAs system, several configurations containing a mixture of Bi-Ga heterodimers and Bi-Bi homodimers are stable. This suggests the Bi/GaSb system may have semiconducting (2×1) reconstruction regions as experimentally observed in the Bi/GaAs system.[19, 20, 21]

CHAPTER VII

Conclusions

In this dissertation, Bi has been shown to accomplish several effects on the surfaces of GaAs and GaSb. The large size of the Bi atoms relative to the constituent Ga, As, and Sb atoms causes strong surface segregation of Bi to the surface with little incorporation, making Bi a strong surfactant on these two alloys. On the other hand, appreciable Bi concentration has been shown in GaAs when growing at low temperatures, low growth rates, and As:Ga ratios of ∼1.[18, 23, 85] In either case, whether Bi is on the surface only or incorporated into the film, the surface morphology and atomic structure are affected.[102, 103] The first two studies focused on using Bi as a surfactant in GaAs. The second two studies focused on experimental Bi incorporation into GaSb on the micron scale surface morphology and the atomic surface structure through DFT simulations.

7.1 Bi/GaAs Surfaces

Bi (BEP of $\sim 1.5 \times 10^{-7}$torr was deposited onto GaAs using MBE at substrate temperatures of 400-445°C with no Ga or As overpressure. A number of effects were observed on the micron length scale (MLS) and nanometer length scale (NLS) using AFM and STM. After 12s of Bi deposition, the surfaces became smoother with wider terraces on the MLS, consistent with previous work.[53, 52] Imaging of the same

surface with STM shows two transformations of the GaAs surface.

The first NLS transformation is the step edge density has increased dramatically, with the flat terraces in bare GaAs giving way to a gnarled step morphology. Moreover, the type of steps has changed. In bare GaAs, adjacent steps are similar, that is, the steps edges increase or decrease in height. In Bi/GaAs, the steps are opposite, meaning a step that increases the height is bordered by other step edges that decrease the height. Thus, the NLS morphology is rougher owing to this oscillation in height. From this, it is proposed the smoothing on the MLS occurs because of the formation of opposite steps on the NLS suppressing the train of similar steps necessary to form a rougher surface on the MLS. High resolution STM imaging shows the second NLS transformation is the surface reconstruction change, where the regular $\beta 2\,(2\times 4)$ rows of the bare GaAs surface are replaced by a disordered $(n\times 3)$ reconstruction. The images also reveal the individual reconstruction units are not of uniform appearance, suggesting composition modulation as Ga, As, and Bi compete for the surface dimer sites. Size measurements suggest the reconstruction is a disordered (4×3) reconstruction, which according to work by Romanyuk *et al.*,[55] is capable of producing the (1×3) and (2×3) RHEED patterns observed in this work and elsewhere.[23, 22, 52]

7.2 Bi/GaAs Phase Diagram

The STM imaging of the first study (Ch. III) suggest a (4×3) reconstruction for the observed $(n\times 3)$ RHEED patterns. Resolution was not sufficient to determine the composition of the reconstruction. Instead, cluster expansions for the $\beta 2\,(2\times 4)$, $c\,(4\times 4)$, (4×3), and (2×1) reconstructions were constructed and several compositional configurations of each relaxed with DFT simulation. Comparison of the free energies of each configuration as a function of chemical potential produces the 0 K phase diagram (Fig. 4.3) of the Bi/GaAs surface.

From Fig. 4.3, it is seen the (4×3) reconstruction becomes stable relative to the common GaAs(001) $\beta 2\,(2 \times 4)$ and $c\,(4 \times 4)$ reconstructions as μ_{Bi} increases. Some reconstructions, such as the (2×4) and (2×1) reconstructions, do not accommodate Bi readily, as evidenced by the low number of stable configurations. The (4×3) reconstruction has the most stable configurations, with these subdivided into the $\alpha\,(4 \times 3)$, $\beta\,(4 \times 3)$, and $h0\,(4 \times 3)$ variants. Several of the (4×3) configurations are similar in energy, as evidenced by the close spacing of the boundaries. This suggests a high degree of compositional disorder in the (4×3) configurations, as corroborated by the experimental STM observations of Ch. III.

To simulate this disorder, statistical Monte Carlo simulations were performed on the (4×3) reconstructed surface. Surface snapshots of simulated cooling runs through typical MBE substrate temperatures all the way to 0 K show a breakdown in the groundstate configuration even at 60°C. Calculation of the entropy as a quantitative measure of overall disorder for the $\beta\,(4 \times 3)$ configurations confirms this. The order parameter η was calculated to determine the individual site disorder, which showed the compositional disorder in the (4×3) reconstruction tends to concentrate in the 3 anion-anion surface dimers. Therefore, from these methods, it is clear an ordered (4×3) reconstruction is likely not possible in the Bi/GaAs system.

7.3 GaSbBi(As)/GaSb Growths

Several nominally GaSbBi films were grown on GaSb substrates at low (330 °C) substrate temperatures. Images of the 200 nm buffer grown at 485 °C shows a flat, terraced surface morphology with cracks. XRD analysis of the buffer only film shows residual As incorporation, with the subsequent lattice contraction and tensile film strain causing the cracks to form. Low temperature growth of GaSb analogous to the GaSbBi growths show the formation of several Ga droplets from film growth and increased As concentration. RBS characterization of this sample shows a rounded

step for the Sb signal owing to the droplets.

Similarly, the GaSbBi films show droplets form and residual As incorporation occurs during growth. The droplets exhibited several new features over the analogous GaSb film, such as phase separation, sub-droplets, and faceting. Droplet etching was also observed. The Ga-Bi phase diagram shows that at growth temperatures, the droplets were uniformly mixed, causing the Ga in the droplets to etch evenly into the films. During cooling, the Ga and Bi separated owing to the vastly different solid crystal structures, resulting in the distinct phases and sub-droplets. Faceting was due to the tendency of solid Bi to form facets, as these appeared even in droplets that had almost no Ga.

Bi concentration was measured with RBS, which revealed Bi concentrations of up to 12 %. Subsequent XRD calculations yielded the % strain relaxation and the As concentration. It was clearly seen that Bi and As concentration were directly related, suggesting a strain auto-compensation effect between lattice-expanding Bi and lattice-contracting As incorporation into GaSb. As more evidence of this effect, the trend of percentage strain relaxation vs. Bi/As concentration ratio showed an increase in film strain as the two concentrations diverged.

7.4 GaSb and Bi/GaSb Phase Diagrams

A cluster expansion and DFT investigation was carried out on the GaSb surface system in an effort to resolve the unresolved debate of why the $c\,(2 \times 10)$ reconstruction is stable. All the possible Ga_{Sb} anti-site possibilities of the second Sb layer were enumerated up to the point where the ECM is satisfied (three Ga_{Sb} defects over two primitive unit cells). Cluster expansions of the (4×3), $\alpha 2\,(2 \times 4)$, $\beta 2\,(2 \times 4)$, $c\,(4 \times 4)$, $c\,(2 \times 6)$, and (2×8) reconstructions were considered as well. For the bare GaSb surface system, no $c\,(2 \times 10)$ reconstruction was stable; the most energetically favorable was the $c\,(2 \times 10)$-3/2 configuration, which was $\sim$20 meV/(1×1)

area higher in energy than the (4×3) reconstruction.

A phase diagram of the Bi/GaSb surface system was also constructed by enumerating all of the Bi_{Sb} site possibilities for the above mentioned reconstructions. The $c\,(2 \times 10)$-3/2 configuration was used for the $c\,(2 \times 10)$ reconstruction cluster expansion, to see if Bi stabilizes this semiconducting configuration. The (2×1) reconstruction was considered as well, owing to its appearance in other III-V surface systems. The phase diagram shows the (4×3) reconstruction is still stable over all $c\,(2 \times 10)$ configurations calculated. The (2×1) reconstruction is stable under high μ_{Bi}, low μ_{Sb} conditions, with the (2×1)-2 configuration having a large region of stability. Other (2×1) configurations with Bi-Ga heterodimers were present, suggesting the Bi/GaSb surface system may have exhibit the same semiconducting (2×1) regions as observed for GaAs.[19, 20, 21]

7.5 Comparison of the Surface Phase Diagrams

With the Bi/GaAs and Bi/GaSb phase diagrams in hand (Figs. 4.3 and 6.6), some comparisons of these two systems can be made. The Bi/GaAs system exhibits a larger number of stable reconstructions, such as the (2×4) reconstructions that are only observed under strain in GaSb.[94, 95] In both systems, reconstructions with double anion layers (i.e., the (4×3) and $c\,(4 \times 4)$ reconstructions) have many stable Bi-containing configurations, while the single anion layer reconstructions (i.e., the (2×4) and (2×1) reconstructions) have only a few Bi-containing configurations. Such behavior can be explained by bond strengths between Ga, As, Sb, and Bi.

The low number of configurations in the Bi/GaAs single anion layer reconstructions suggests the Ga-Bi bonds are stronger than As-Bi bonds in these reconstructions, resulting in a strong preference for Bi occupation in the dimer sites in the (2×1) and $\alpha 2\,(2 \times 4)$. In contrast, the (4×3) and $c\,(4 \times 4)$ reconstructions have many configurations, and the observed disorder on the Bi/GaAs (4×3) surface all point to weaker

site preference for Bi occupation owing to the weaker As-Bi bonds. Hence, thermal effects are enough to break the As-Bi bonds but not the Ga-Bi bonds, explaining the disorder in the (4×3) reconstruction and the order in the (2×1) reconstruction.

The situation is different for the Bi/GaSb system. The (4×3) reconstruction is stable over a wide range of conditions with less disorder, although the Sb-Bi bond is weaker than the As-Bi bond. This discrepancy can be explained by the larger lattice constant of the underlying GaSb substrate. The appearance of a GaSb (2×4) when constrained to the GaAs lattice constant [94, 95] and the strain relieving properties of the Bi/GaAs (2×1) reconstruction [19, 47] suggest these reconstructions are energetically favorable with smaller substrate lattice constants. Conversely, the (4×3) reconstruction appears to favor larger lattice constants with less strain, consistent with its appearance on the bare GaSb and InAs systems.[26, 61] Moreover, the size mismatch between Sb and Bi is smaller than that between As and Bi. This lowers the strain effects of Bi incorporation into the dimer sites. These two factors contribute to the greater stability of the (4×3) reconstruction and the lack of disorder in the Bi/GaSb system.

Therefore, the reconstruction stability is determined according to the following factors:

1. Strain on the reconstruction from the underlying substrate largely determines which reconstructions appear, with smaller lattice constants seeming to favor single anion layer reconstructions.

2. Bi-V bond strength then determines the amount of disorder in the (4×3) reconstruction and the number of configurations in double anion layer reconstructions.

3. The Ga-Bi bonds discourage surface disorder in the single anion layer reconstructions.

CHAPTER VIII

Future Work

All of the work presented in this dissertation has focused on the effects of Bi on III-V surfaces. Based on the evidence, a number of future studies are proposed below to further the understanding gained here. Also, suggestions for crystal growers are given as to the ideal growth conditions for surfaces conducive to high quality GaAsBi and GaSbBi. Finally, some long-term suggestions on the possible lattice-matched heterostructures that can be produced are given.

8.1 Bi/GaAs Surfaces

The work done in Ch. III is promising for obtaining consistently sharper interfaces and high quality device growth even at low temperatures, but some other behavior needs to be more clearly understood. The appearance of the gnarled step morphology suggest the incorporated Bi atoms in the surface reconstruction produce a large lateral strain. A higher step edge density permits a larger amount of strain relaxation in upper terraces as the edges of the terrace extend outward over the terrace beneath. As such, it is possible Bi preferentially occupies sites in the upper terraces. As the composition of the surface reconstruction was not determinable from the STM imaging presented in this work, it is unlikely this question can be resolved with experimental STM. One possible alternative is to use STS to determine the I-V curves

of various reconstruction units near step edges to characterize which has more or less Bi. However, all the (4×3) reconstructions obey the ECM,[28] and Bi substitution will not affect the charge balance of the surface. Thus, changes may be difficult to detect in STS. The other alternative is to use a solid-on-solid (SOS), where the surface is treated as individual, discreet blocks that represent individual reconstruction units. The energy of interaction between them governs whether what reconstruction units will neighbor a given unit, much like the kinetic Monte Carlo treatment of GaAs etching.[90] The composition, strain, and step edges near each block would affect the interaction energies, and from such a simulation it would be possible to determine a preference in Bi surface occupation.

8.2 Bi/GaAs Phase Diagram

The phase diagram of Fig. 4.3 provides a useful map of growth conditions and suggest how to achieve the desired surfaces in MBE growth. In future work, the Bi/GaAs phase diagram could be expanded upon to included finite temperature effects using the same sMC methods. This would be done by simulating the surface at fixed temperature at various points of (μ_{As}, μ_{Bi}) that span the entire range of chemical potential in the phase diagram. This could be done for any fixed temperature, but would have to be done for all the structures considered to get an accurate comparison of finite temperature stability. A reference state can be obtained by simulated heating of the 0 K reference states to the temperature in question. The calculated energies at each (μ_{As}, μ_{Bi}) point could be substituted for the 0 K DFT energies and the same integration of γ from the reference state used above to calculate a finite temperature phase diagram. Thus, certain groundstates observed at 0 K might disappear when considering the effects of temperature. Given the disorder of the (4×3) surface, it is possible that structure may have no stable configurations and will be a single disordered region on such a phase diagram.

Another avenue of further exploration is to allow Bi substitution into the slab underlying the surface reconstruction. However, this would require far more enumerated structures. An alternative to this is to change the lateral GaAs lattice constant to mimic the effect of Bi incorporation. The strain resulting from such a change may induce different stabilities in the reconstructions and their configurations, as has been seen in GaSb.[94, 95] This can also be used to investigate the effects of strain on the reconstruction stability, as was done with Sb on GaAs by Bickel *et al.*[94, 95, 96, 97]

Another study to be done is to explain why the (2×1) reconstruction does not have any second layer Bi_{Ga} anti-site defects as proposed to explain observed semiconducting (2×1) configurations.[19, 20, 21] One possible explanation is the formation of vacancies near the surface that act as a means of satisfying the ECM. To investigate this, a cluster expansion of the (2×1) reconstruction can be constructed to accommodate vacancies at various sites in the DFT slab. The configurations can then be compared as before to determine if these are stable.

8.3 GaSbBi(As)/GaSb Growths

Strain auto-compensation via the simultaneous incorporation of Bi and As is potentially very useful in the growth of lattice-matched, unstrained heterostructure devices. However, the films of Ch. V tend to show a net lattice contraction, owing to the lattice parameter differences of GaAs, GaSb, and GaBi. The difference between the GaAs and GaSb lattice parameters is $6.096\text{Å} - 5.654\text{Å} = 0.442\text{Å}$, while the difference between the GaBi and GaSb lattice parameters is $6.324\text{Å} - 6.096\text{Å} = 0.228\text{Å}$. Thus, GaAs formation has a stronger effect on the lattice parameter than GaBi formation, requiring more Bi than As to achieve lattice matching with the GaSb substrate. Despite this, the fact that the strain relaxation decreases with increasing Bi/As concentration ratio in these films may suggest that the residual As overpressure is too low for complete auto-compensation of a Bi concentration of >12%. Therefore, growth

of these films with a deliberate As flux would be of interest for future studies.

The GaSbBiAs alloy has significant potential for use in device growth. The strain auto-compensation mechanism allows for easier lattice-matched films to be grown. Such an effect would be harder to accomplish in GaAsBi, as elements smaller than As (N and P) would be needed to counter balance the Bi-induced lattice expansion. Both N and P require specialized sources, but As is readily available on many MBE chambers. Moreover, GaSbBiAs films could potentially be lattice-matched to any substrate between GaAs and GaSb, including InP and InAs. The ability to fabricate films of low bandgap on a variety of substrates opens up new possibilities in high-quality, low defect density long wavelength and infrared optoelectronic devices.

It also remains to be seen what effect the simultaneous incorporation of Bi and As has on the GaSb bandgap. Both elements reduce the bandgap of GaSb individually, but the combination of the two may not have the same effect. To date, it has been shown that simultaneous N and Bi incorporation into GaAs cause a combined bandgap reduction greater than the individual N and Bi reductions.[6] Photoluminescence measurements of GaSbBiAs films would be of interest, as these would be easier to grow and have greater potential for long wavelength devices than GaAsNBi.

The means of growing GaSbBi films proposed by Song *et al.*,[86], with the Sb flux set to 10% higher than the Ga flux to prevent droplet formation, merits further optimization. In their work, the Bi concentration was reported as <1%, suggesting the excess Sb overpressure suppressed Bi incorporation. The low droplet coverage observed in BGR-1 suggests the excess Sb and low growth rate used in that work are unnecessary to achieve a flat, droplet-free film with higher Bi concentration. Thus, another avenue to explore is the optimization of flux ratios and substrate temperature to achieve a reasonable growth rate and the desired surface, which the present work suggests is possible.

8.4 GaSb and Bi/GaSb Phase Diagrams

Like for the Bi/GaAs phase diagram, the Bi/GaSb phase diagram (Fig. 6.6) provides useful suggestions on what surface reconstruction will be obtained under which conditions. There are many ways to build upon the Bi/GaSb work presented in Ch. VI. The first is to consider As incorporation into the surface. According to the results of Ch. V, residual As concentration from background sources during GaSbBi film growth is non-negligible. Thus, constructing new cluster expansions to permit As occupancy in addition to Sb and Bi occupancy of the anion sites might shed new light on the stability of the reconstructions, perhaps permitting a semiconducting $c\,(2 \times 10)$ configuration to remain stable. The second improvement is to allow $\mathrm{Bi_{Sb}}$ and $\mathrm{As_{Sb}}$ substitution in the bulk of the slabs, to simulate the true GaSbBi(As) surface rather than using the Bi/GaSb surface system as a proxy.

The appearance of the (2×1) reconstruction in the Bi/GaSb phase diagram is of great interest. This surface has been suggested as the best surface for growing high Bi concentration GaAsBi films with CuPt_B bulk ordering,[85, 104] owing to the large Bi surface concentration and the lack of disorder at growth temperatures seen in Ch. IV. It is likely this is the case for GaSbBi as well, and as such it is of interest to obtain this reconstruction experimentally on GaSb. This is done in GaAs at low temperatures (~ 370°C or lower), where Ga is deposited to obtain a Ga-rich surface, after which Bi is deposited, resulting in the necessary low μ_{As}, high μ_{Bi} needed for the (2×1) reconstruction to appear. This may accomplish the same on GaSb, but the experimental conditions must be adjusted accordingly for the GaSb substrate.

One of the main challenges in this work was the sheer amount of enumeration needed to characterize the reconstructions, especially for the $c\,(2 \times 10)$ and $c\,(2 \times 6)$ reconstructions. Even with cluster expansion automation code, the number of configurations from allowing Ga, Sb, and Bi site occupancy from the start were too many for serial processing on a single computer. As the systems studied by the cluster ex-

pansion grow more complex, and the appearance of multiple computer cores continues to increase, the drive towards parallelized enumeration of configurations will increase. For this work, such improvements would allow larger supercell configurations to be enumerated and the simultaneous effects of Bi_{Sb} and Ga_{Sb} could be investigated for the $c(2 \times 10)$ system.

It is possible the combined effects of Bi and Ga substitution for Sb sites causes a Bi-containing $c(2 \times 10)$ reconstruction to appear. This would also permit exploration of the $c(2 \times 10)$ reconstruction with more Ga_{Sb} anti-site defects, potentially establishing the stable metallic $c(2 \times 10)$ configuration. Moreover, the residual As incorporation seen in the GaSbBi(As) growths suggest As may appear in these sites as well. All of these improvements to the accuracy of the cluster expansion may in the future be possible with improved enumeration techniques, leading to a more accurate characterization of the Bi/GaSb surface system.

8.5 Final Recommendations for Crystal Growers

The focus on GaAs and GaSb surfaces in this dissertation has been with an eye to improving heterostructure device interfaces. Surface morphology and atomic structure control are critical for producing sharper interfaces and higher quality devices, which the present work helps achieve. For growing high Bi concentration, high-quality GaAsBi or GaSbBi layers with $CuPt_B$ ordering, the (2×1) reconstruction is considered the best reconstruction to have during growth. This is likely due to the high concentration of Bi on the surface (1 Bi atom per every (1×1) unit area for the (2×1)-2 configuration in Fig. 4.3) and the persistent long range dimer order.[24, 38] Hence, according to Figs. 4.3 and 6.6, growing under high-Bi, low-As or low-Sb conditions will encourage the formation of the (2×1) reconstruction during growth.

On the other hand, a notable difference between the Bi/GaAs (Fig. 4.3) and the Bi/GaSb (Fig. 6.6) phase diagrams; the (2×1) reconstruction has a large region of

stability in the Bi/GaAs system but not in the Bi/GaSb system. Also, the (2×1) reconstruction in GaSbBi has not been experimentally proven to date, and may not be stable relative to Ga-Bi droplets. If this is the case, the (4×3) reconstruction must be used instead. Fortunately, the (4×3) reconstruction is more ordered in the Bi/GaSb system than the Bi/GaAs system. Growth on the intermediate Bi-containing (4×3) configurations is preferable given the more uniform composition. This would be relatively easy to achieve, since the regions of stability for the other configurations in Fig. 6.6 are small.

Bastiman *et al.* high-quality GaAsBi films grown at 400°C, considerably higher in temperature than other GaAsBi films.[103, 105] Ptak *et al.* showed GaAsBi forms droplets more easily at lower growth rates, with higher growth rates producing higher Bi concentrations with higher Bi fluxes.[85] Song *et al.* mitigated GaSbBi surface droplets through higher temperatures (330-390°C vs. the 300°C in this work) while keeping the Bi flux below the Bi vapor pressure and the Sb flux just above the Ga flux.[86] However, Bi concentrations were <1%, and the RHEED of the surface reconstruction was unknown during those growths. Hence, it is recommended for future work in optimizing GaAsBi and GaSbBi growths to aim for the following conditions:

1. Grow at as high a substrate temperature (that is, in the 330-400°C range) as possible without desorbing Bi. This will encourage higher quality films and discourage droplet formation.

2. As/Ga or Sb/Ga ratios should be only slightly above 1 to keep an anion-terminated surface without preventing Bi adsorption.

3. Use as much Bi as necessary to maintain the (2×1) reconstruction.

4. Use the fastest growth rate possible without suppressing Bi incorporation; Bi flux cannot be increased past the vapor pressure of the system, so growth rate

must be tailored to achieve the desired Bi concentration.

8.6 Potential Applications of GaAsBi, GaSbBi, and GaSbBiAs

GaAsBi and GaSbBi alloys have both complimentary and divergent uses. Both alloys are suitable for long wavelength optoelectronic devices, although GaSbBi is more suitable for longer wavelengths than GaAsBi, given the lower GaSb bandgap and the reduction caused by Bi. Moreover, concurrent As and Bi incorporation likely lowers the bandgap even further, a feature not as easy to obtain with GaAs using N or P. Therefore, GaAsBi would be a useful alloy for red-infrared optoelectronic devices, and GaSbBi or GaSbBiAs would be more suitable for the longer wavelengths in the infrared spectrum.

Based on the lattice expansion observed in GaAsBi via XRD,[9, 18, 56, 83, 106, 107] this alloy in the future could be lattice matched to larger lattice constant substrates such as InAs and InP. The strain auto-compensation behavior of GaSbBiAs could also permit lattice matching to the same InAs and InP substrates. Hence, heterostructure devices involving many different III-V semiconductors, all possibly lattice-matched to one another. This ability opens up potentially new avenues in bandgap engineering, allowing great flexibility in band structure while avoiding strain induced defects such as dislocations.

APPENDICES

APPENDIX A

Matlab Code for Surface Phase Diagram Plotting

The code below takes the cluster expansion data generated by CASM to produce the Bi/GaAs phase diagram. Both the predicted energies of all the configurations and the calculated DFT energies (energy.clex and energy) are used, along with the predicted and actual convex hull data (hull.clex and hull files). These files must be formatted such that the header line is removed and the "con" text in the configuration number column must be removed and the "energy.clex", "energy", "hull.clex", and "hull" files renamed to "eclexdata", "energydata", "hclexdata", and "hulldata", respectively. The code below as shown will construct the (4×3)-only phase diagram out of the energies predicted by the cluster expansion, not the "true" DFT energies.

The phase diagram plotted in Fig. 4.3 compares the calculated DFT energies, not the cluster expansion energies. In order to plot the DFT energies, the "eclexdata" and "energydata" files and the "hclexdata" and "hulldata" files must be switched. In order to plot the phase diagram for other reconstructions, some parameters need to be changed. The E0, E1, and E2 energies need to be replaced with the reference energies of the all-As, all-Ga, and all-Bi configurations. Ga_slab and As_slab must be changed to the number of Ga and As atoms in the slab, not counting the surface atoms. This is for subtracting out the bulk contribution to the energy. NSites must

be changed to the number of sites considered (usually the number of dimer sites). Area is the number of (1×1) unit area cells in the reconstruction.

This code was developed with the help of Dr. John C. Thomas with various edits and improvements over time by Adam Duzik.

```
    ======================
    EH=-8.19113;
    Ebulk=-9.73694;
    EAs=-.10800403E+02/2;
    EGa=-.14468964E+02/4;
    EBi=-.91679793E+01/2;
    eclex=load('eclexdata');
    energy_clex=eclex(:,1);
    Bi_clex=eclex(:,3); %x_As
    Ga_clex=eclex(:,4); %x_Bi
    names_clex=eclex(:,end); %Configuration names
%======================
    energy1=load('energydata');
    energy=energy1(:,1);
    Bi=energy1(:,3);
    Ga=energy1(:,4);
    names=energy1(:,end);
%======================
    hclex=load('hclexdata');
    energy_hclex=hclex(:,1);
    Bi_hclex=hclex(:,3);
    Ga_hclex=hclex(:,4);
    names_hclex=hclex(:,end);
%======================
    hull=load('hulldata');
    energy_hull=hull(:,1);
    Bi_hull=hull(:,3);
```

```
    Ga_hull=hull(:,4);
    names_hull=hull(:,end);
%==================== For Cluster expanded energies ==========
    clex_matrix=[Bi_clex Ga_clex energy_clex];
    chull_points=convhulln(clex_matrix);
    hpoint_index=unique([chull_points(:,1); chull_points(:,2); chull_points(:,3)]);
    %hpoint_low holds indeces of all convex hull points with formation energy < 0
indeces correspond to line numbers in eclexdata file
    hpoint_low=unique(le(energy_clex(hpoint_index),0).*hpoint_index);
    names_clex(hpoint_low(2:end))
%===== This figure is convex hull in terms of As and Bi concentration
figure; trisurf(chull_points, Bi_clex, Ga_clex, energy_clex);
    xlabel('As concentration')
    ylabel('Bi concentration')
    %Specify grids of As and Bi chem potential
    x=(-1:.05:0); %%As limits
    y=(-1:.05:0); %%Bi limits
    [mu_As, mu_Bi]=meshgrid(x,y);
    %Cdata is dummy grid for plane color data
    Cdata=0*mu_As+1;
%===Draw phase diagram using "canonical" chemical potential axes
    %Plane colors and display names are determined by indeces in eclexdata file
    %Remember to view phase diagram from bottom of the set of planes.
    %%Reference state energies in eV
    E0=-613.343;
    E1=-633.465;
    E2=-626.464;
```

```
%%First, add plane defined by reference states
E_tot=energy_clex+Bi_clex*(E2-E1)-(Ga_clex)*(E1-E0)+E1;
%%Num of Ga and As atoms in bare slab
Ga_slab=48;
As_slab=58;
%%Define area-normalized x_As and x_Bi
NSites=10;
NGa=Ga_slab+NSites*Ga_clex;
NAs=As_slab+NSites*(1-Ga_clex-Bi_clex);
NBi=NSites*Bi_clex;
Area=12;
x_As=(NAs-NGa)/Area-0.5;
x_Bi=NBi/Area;
A_clex=(E_tot-NGa*Ebulk-(NAs-NGa)*EAs-NBi*EBi)/Area;
%%Plot energy planes of points on convex hull
figure(2)
hold on
for ind=1:length(hpoint_low);
gamma_clex=A_clex(hpoint_low(ind)) - mu_As*x_As(hpoint_low(ind))...
- mu_Bi*x_Bi(hpoint_low(ind)) - EH;
surf(mu_As, mu_Bi, -gamma_clex, Cdata*ind/length(hpoint_low), 'DisplayName',
int2str(3E+08+hpoint_low(ind)), 'EdgeColor', 'none')
end
xlabel('mu_As (eV)')
ylabel('mu_Bi (eV)')
%%Load data for reference reconstructions (includes the c(4x4)beta and zeta(4x2)
reconstructions), and plot their energies
```

```
ref_conc=load('ref_conc');
ref_energy=load('ref_energy');
ref_Area=ref_conc(:,1)/2;
A_ref=(ref_energy-ref_conc(:,2)*Ebulk-(ref_conc(:,3)-ref_conc(:,2))*EAs)./ref_Area;
x_Asref=(ref_conc(:,3)-ref_conc(:,2))./ref_Area-0.5;
hold on
for ind=1:length(ref_energy);
gamma_ref=A_ref(ind)-mu_As*x_Asref(ind)-EH;
surf(mu_As, mu_Bi, -gamma_ref, Cdata*0, 'DisplayName', int2str(-ind))
end
```

APPENDIX B

Complete List of All Configurations on the Bi/GaAs Phase Diagram

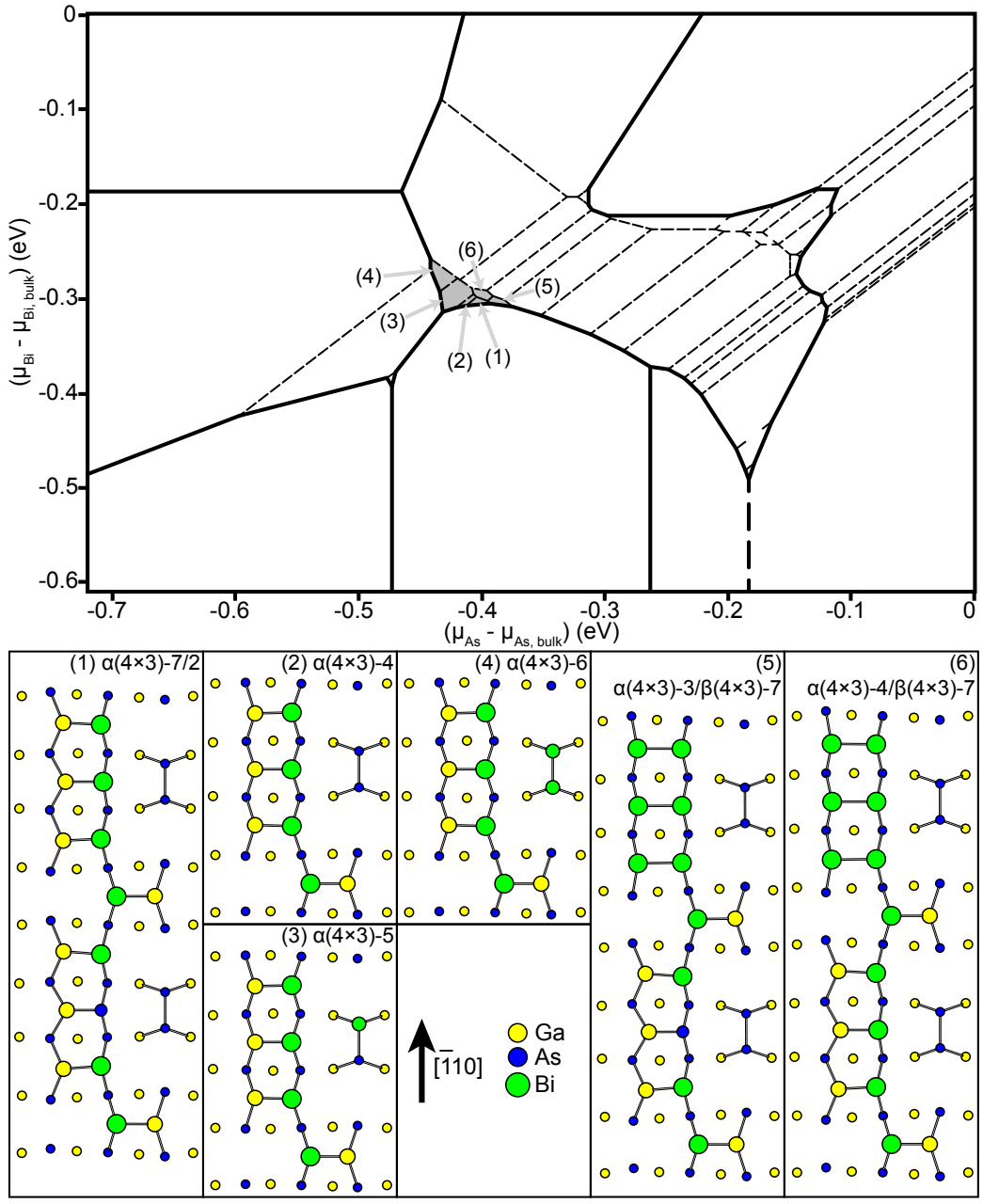

Figure B.1. The $\alpha(4 \times 3)$ configurations are given in regions (1-4), and the mixed configurations consisting of $\alpha(4 \times 3)$ and $\beta(4 \times 3)$ primitive cells are shown in regions (5-6). Numbers correspond to the labelled regions on the phase diagram.

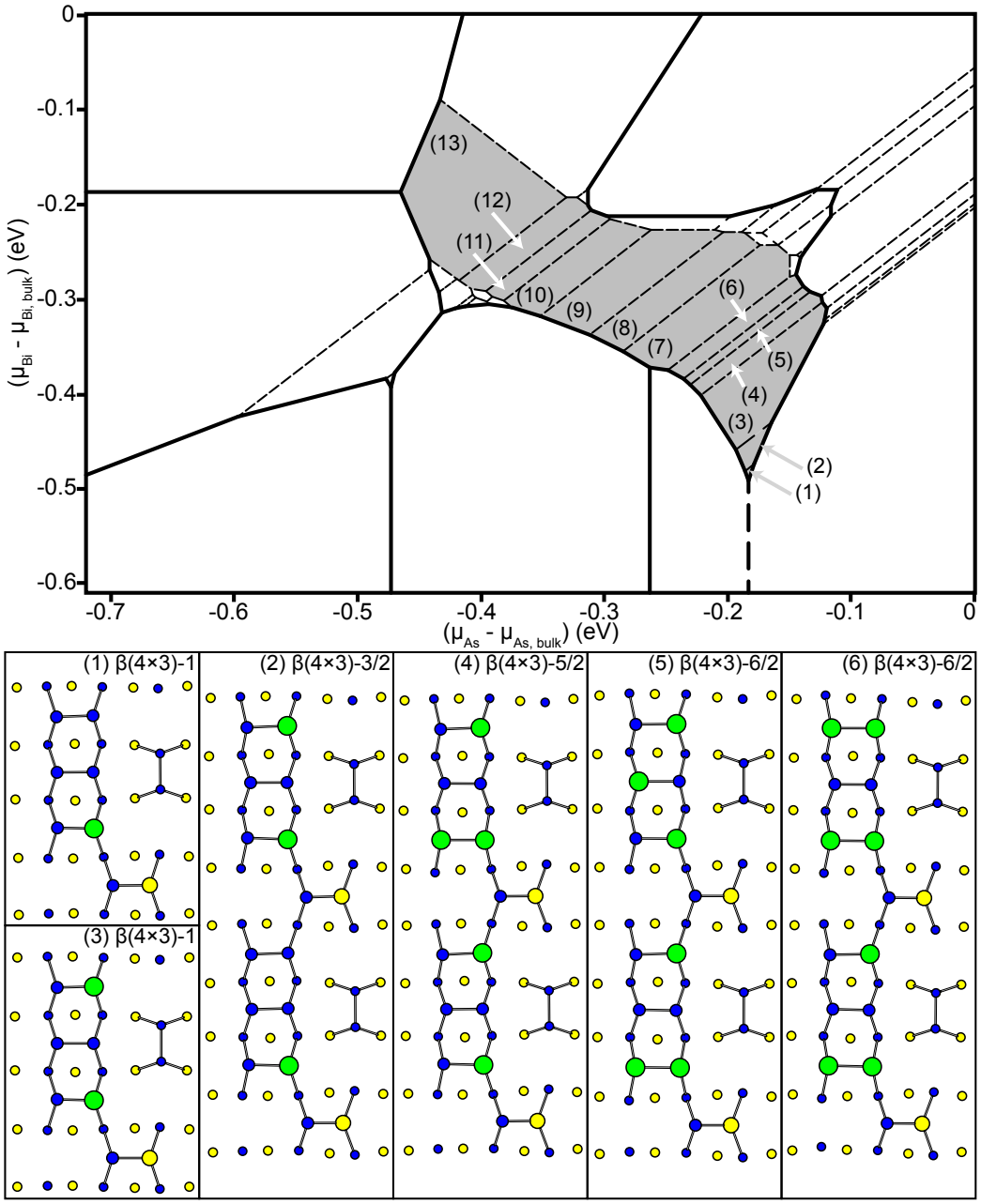
0
-0.1
-0.2
-0.3
-0.4
-0.5
-0.6
(μBi - μBi, bulk) (eV)
-0.7
-0.6
-0.5
-0.4
-0.3
-0.2
-0.1
0
(μAs - μAs, bulk) (eV)
(13)
(12)
(11)
(10)
(9)
(8)
(7)
(6)
(5)
(4)
(3)
(2)
(1)
(1) β(4×3)-1
(2) β(4×3)-3/2
(4) β(4×3)-5/2
(5) β(4×3)-6/2
(6) β(4×3)-6/2
(3) β(4×3)-1

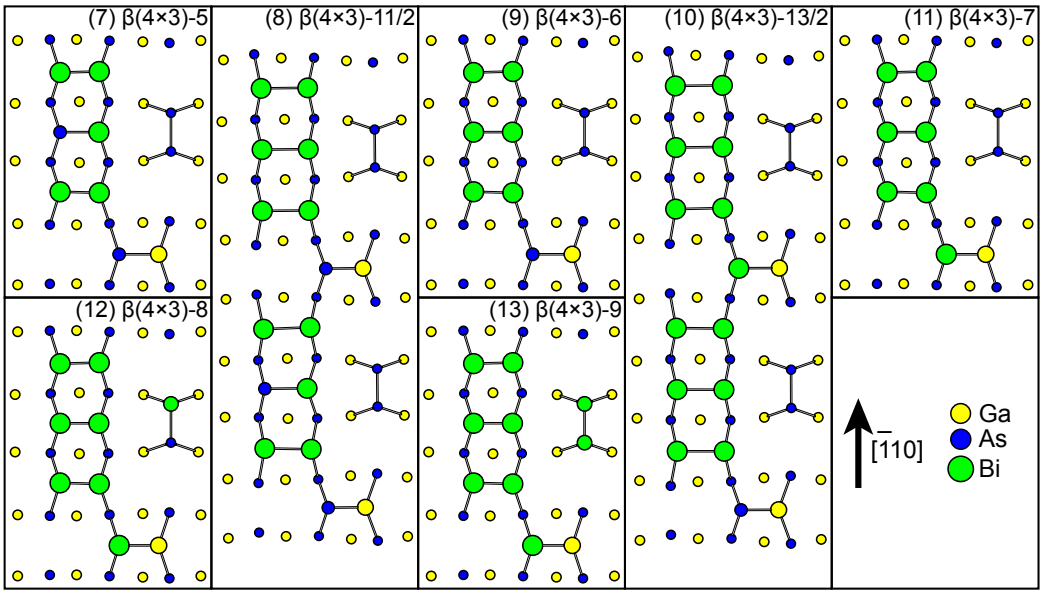

Figure B**.2.** The $\beta(4 \times 3)$ configurations as indicated in the regions on the phase diagram.

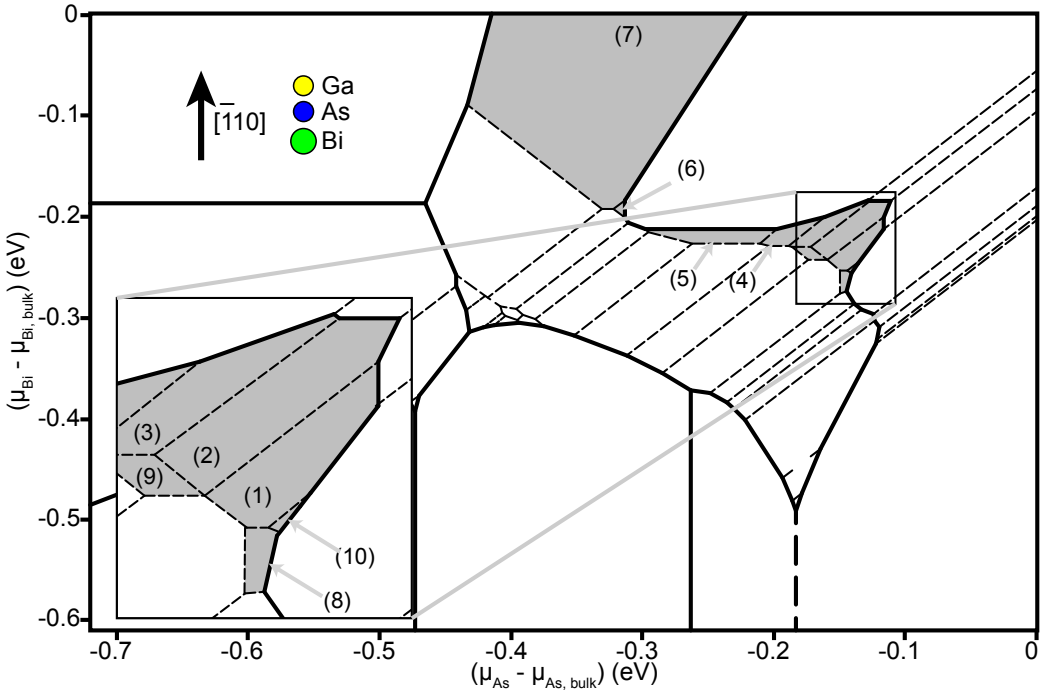
0
-0.1
-0.2
-0.3
-0.4
-0.5
-0.6
-0.7
-0.6
-0.5
-0.4
-0.3
-0.2
-0.1
0
(μBi - μBi, bulk) (eV)
(μAs - μAs, bulk) (eV)
[1̄10]
Ga
As
Bi
(1)
(2)
(3)
(4)
(5)
(6)
(7)
(8)
(9)
(10)

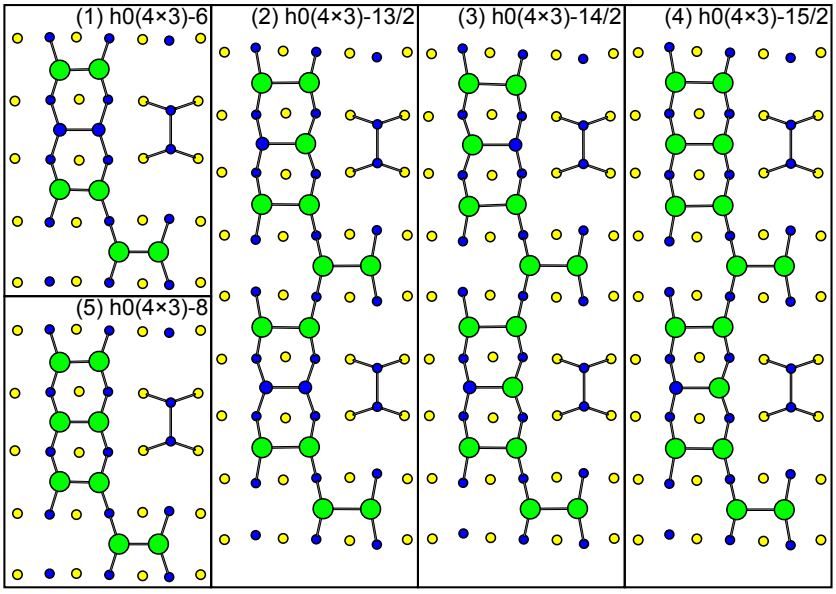
(1) h0(4×3)-6
(2) h0(4×3)-13/2
(3) h0(4×3)-14/2
(4) h0(4×3)-15/2
(5) h0(4×3)-8

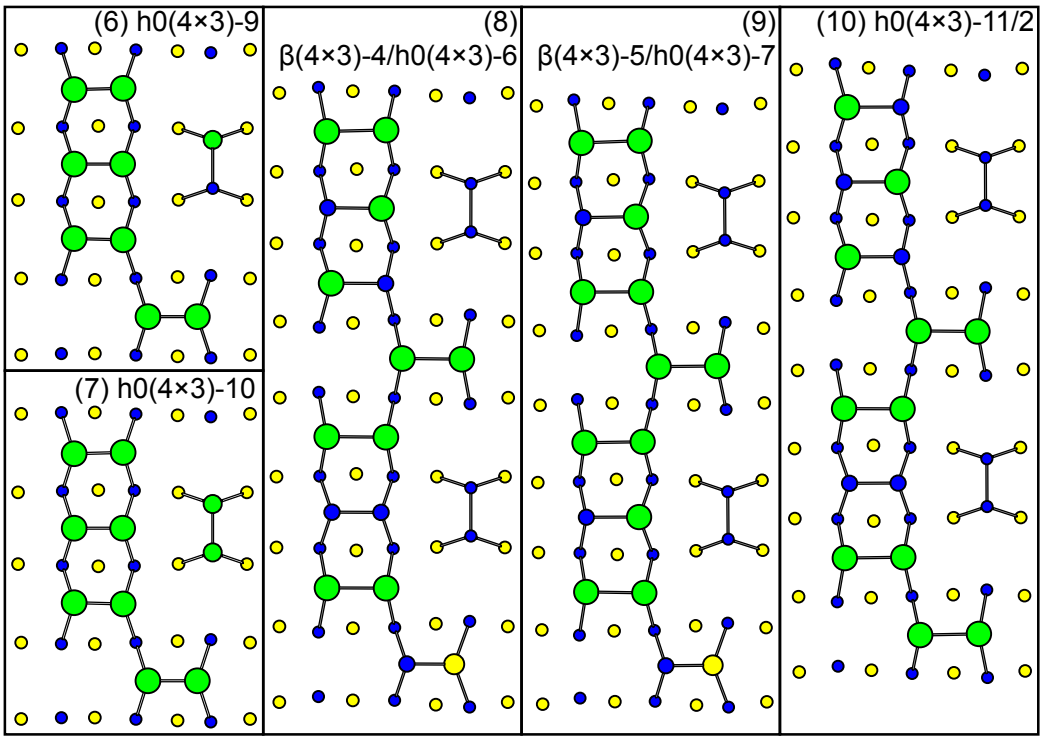

Figure B.3. The $h0\,(4\times3)$ are shown in regions (1-7) and (10), while the mixed configuration of $\beta\,(4\times3)$ and $h0\,(4\times3)$ primitive cells are stable in regions (8-9)

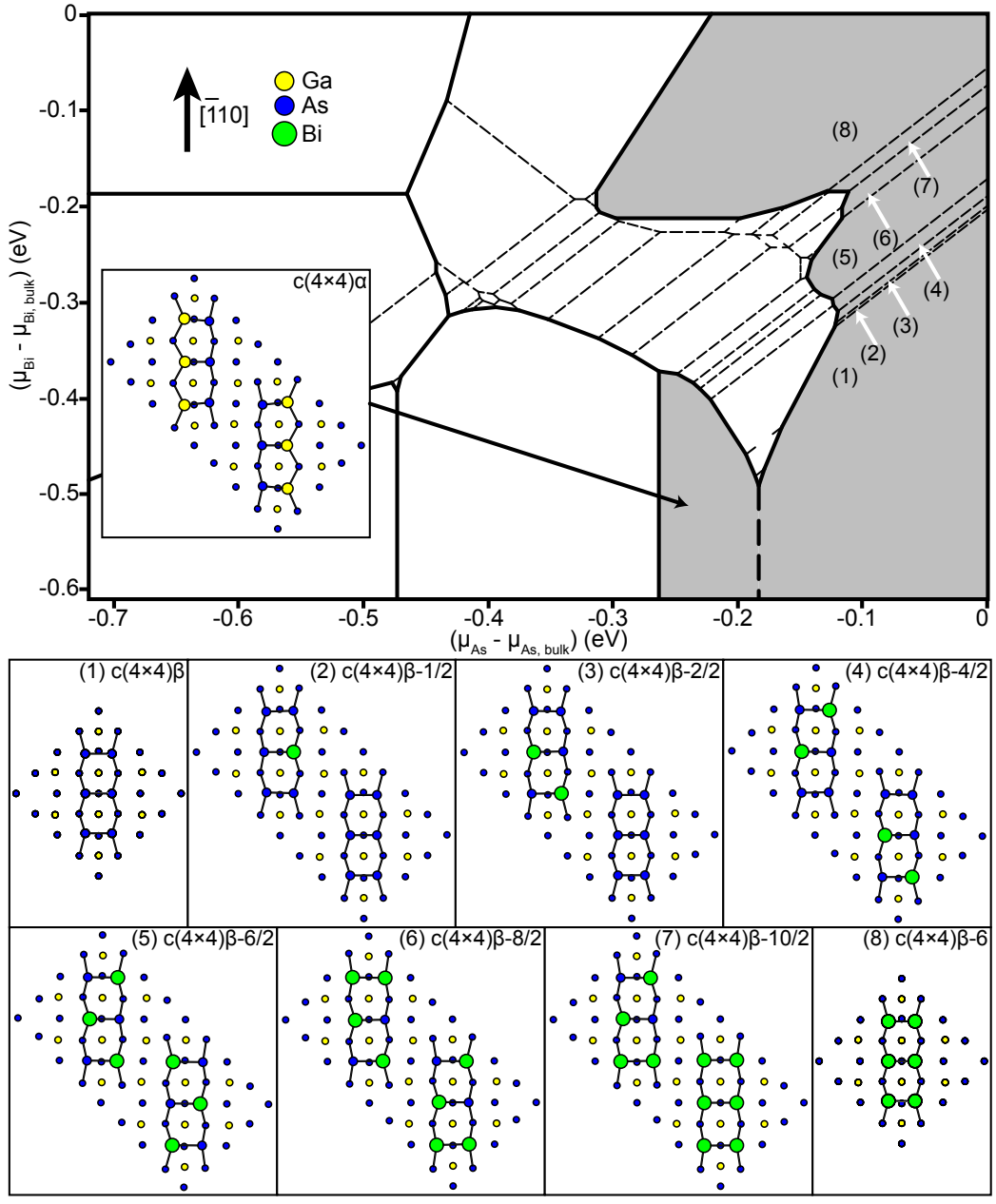

Figure B.4. The $c\,(4 \times 4)$ configurations and the regions of stability.

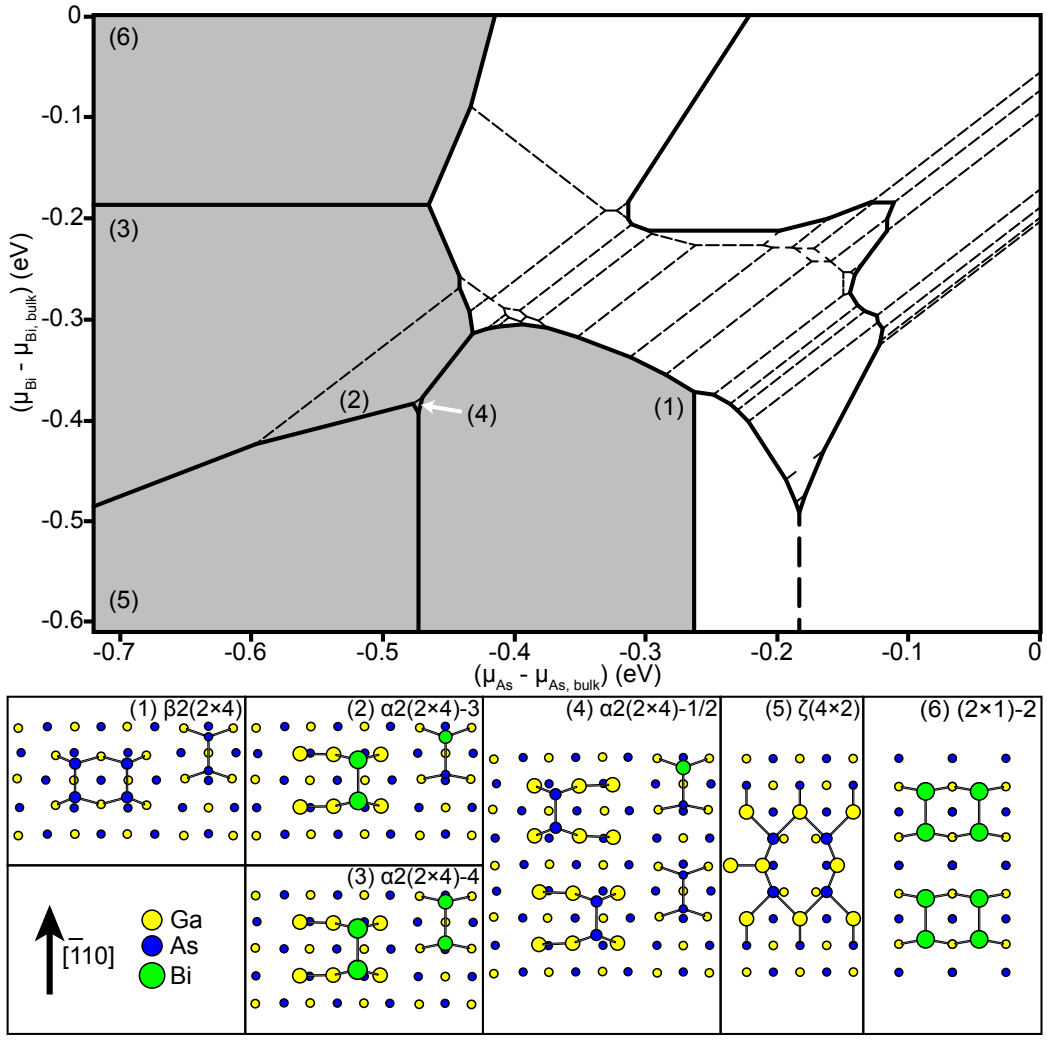

Figure B.5. The remaining $\beta 2\,(2\times 4)$ (1), $\alpha 2\,(2\times 4)$ (2-4), $\zeta\,(4\times 2)$ (5), and (2×1) (6) configurations and corresponding regions of stability.

APPENDIX C

Matlab Code for Fitting GaSbBi(As) RBS Spectra

```
%=====================
%Code to analyze RBS data and put together the composite RBS simulation from
%Ga droplets, Bi droplets, and bare GaSbBi
%Written by Adam Duzik on 2-9-2013
%Version 8 is V7 but with the plotting a little different. The droplet and
%the underlying GaSbBi curves are now merged
%(i.e., GaDroplets + GaCoveredGaSbBi
%and BiDroplets + BiCoveredGaSbBi)


%close all figures first
    close all


%clear all variables
    clear all


%The saveFig flag is either 0 or 1, set it to 1 to save the plotted figures
    saveFig = 1;
    if exist('sampleFolder', 'var') ~= 1
    sampleFolder = input('Enter the sample number: ', 's');
    disp(['Analyzing RBS for ' sampleFolder '...'])
    end
    if exist(sampleFolder, 'dir') ~= 7
    error('Error: sample directory does not exist')
    end
    if exist(fullfile(sampleFolder, 'RBSFittingParameters'), 'file') ~= 2
    error('Error: no fitting parameters found')
    end
```

```
%========Parameter Definition=============
%Define stopping powers for pure Ga and Bi (in ev/ 1E15 atoms/cm^2)
%These will be needed to adjust the relative yield of the GaSbBi underlying
%the droplets. These were calculated in SimNRA.
%The stopping power of GaSbBi varies with the composition, but it is close
%to 86 ev/ 1E15 atoms/cm^2.
    GaStopPow = 70.951;
    BiStopPow = 122.164;
    %Import the fitting parameters file
    fitParams = dlmread(fullfile(sampleFolder, 'RBSFittingParameters'), ' ', 0, 1);
%Define the keV/ch, channel offset, and particles*sr (in terms of n * 1E+10)
%values for rescaling the Universal Bi and Ga RBS curves
    channelOffset = fitParams(1,1);
    keV_Ch = fitParams(2,1);
    partSR = fitParams(3,1);
%partSRFinal is the multiplier for the particles*sr value; increase it to
%shift the whole curve up, 1 to leave things "as is"
    partSRFinal = fitParams(4,1);
%The thicknesses listed in Bi_Ga_ThicknessList are for the values measured
%off the SEM/AFM images. The following multipliers allow for thicker or
%thinner values to be considered without having to reconstruct the
%thickness file
    GaThickMult = fitParams(5,1);
    BiThickMult = fitParams(6,1);
%Define the index, that is the next iteration of these plots.
%Change it if you don't want to overwrite your previous plots
```

```
    index = ['Ga' num2str(GaThickMult) 'xBi' num2str(BiThickMult) 'x'];
%Define limits for the figures.
    unzoomedX = fitParams(7,1:2);
    unzoomedY = fitParams(8,1:2);
    zoomedX = fitParams(9,1:2);
    zoomedY = fitParams(10,1:2);
%Sometimes the RBS .txt files are not all the same length.
%Most the stuff at the end is 0 anyway, so we define a cutoff here so
%everything is of uniform length.
%values for the Oct 2012 runs
    cutoff = fitParams(11,1);
    GaCutoff = fitParams(12,1);
%Define the area fractions of Ga and Bi of the TOTAL image as measured
%from the EDS. We'll multiply this by the height fractions later.
    thetaGa = fitParams(13,:);
    thetaBi = fitParams(14,:);
%RBS fitting parameters always has at least 2 columns of numbers, which can
%cause thetaGa and thetaBi to have two entries when they should only have
%one. The second entry will be zero for both in this case, which we filter
%out here.
    if (length(thetaGa) == 2 && thetaGa(2) == 0 && thetaBi(2) == 0)
    thetaGa = thetaGa(1);
    thetaBi = thetaBi(1);
    end
%values for the Mar 2013 runs
    % cutoff = 1900;
    % GaCutoff = 4200;
```

```
%==========Load Files============
%Get the list of data files
    GaSbBiFileList = textread(fullfile('UniversalGaSbBi', 'MatlabGaSbBiFileList'),
'%s');
    GaSbBiStopPowList = importdata(fullfile('UniversalGaSbBi', 'StoppingPowers'),
' ');
    Bi_Ga_ThicknessList = importdata(fullfile(sampleFolder, 'Bi_Ga_ThicknessList'),
'', 1);
    Bi_Ga_ThicknessList.data(:,1) = BiThickMult * Bi_Ga_ThicknessList.data(:,1);
    Bi_Ga_ThicknessList.data(:,2) = GaThickMult * Bi_Ga_ThicknessList.data(:,2);
%Bi_Ga_ThicknessList is the list of actual thicknesses for the Bi and Ga
%droplets. The RBS for them will be interpolated from a set of universal
%RBS simulations of certain thicknesses of pure Bi and Ga layers
    Bi_Ga_Floor = floor(Bi_Ga_ThicknessList.data / 10) * 10;
    Bi_Ga_Ceiling = ceil(Bi_Ga_ThicknessList.data / 10) * 10;
    FloorActualDifference = Bi_Ga_ThicknessList.data - Bi_Ga_Floor;
    CeilingActualDifference = Bi_Ga_Ceiling - Bi_Ga_ThicknessList.data;


%==========Define Parameters Based on Files============
%List of each height's fraction of total counts within each droplet
    heightFracFile = dlmread(fullfile(sampleFolder, 'heightFrac'), '', 1, 0);
%Define start and end points for the height fractions considered
    heightFracStart = 1;
    heightFracIncrement = 1;
    heightFracEnd = length(heightFracFile);
    %heightFracNumPixelsTotal = 902144; %For SE images (with scale bar cropped
out) (1024*881)
```

```
    %heightFracNumPixelsTotal = 204800; %For EDS SE images (512*400)
    heightFracNumPixelsTotal = 262144; %For AFM images (512*512)
    heightFracNumPixelsDrops = sum(heightFracFile(heightFracStart:...
    heightFracIncrement:heightFracEnd)) + heightFracFile(1);
    numGaSbBiPixels = (heightFracNumPixelsTotal - heightFracNumPixelsDrops)...
    /heightFracNumPixelsTotal; %Fraction of all pixels that are bare GaSbBi
    heightFrac = zeros(heightFracEnd,1);
    channelGaSbBi = zeros(GaCutoff, 1);
    rbsExperimental = zeros(GaCutoff, 1);
    for i = 1:length(thetaGa);
%For every GaSbBi RBS fit, open that file and then average it with the pure Ga and
Bi RBS fits
%Iterate through the specified GaSbBi film-only fits (no Ga or Bi layer on top)
    for filmFileIndex = 1:size(GaSbBiFileList, 1);

%Define output folder
    outputFolder = fullfile(sampleFolder, [sampleFolder '_V8_' GaSbBiFileListfilm-
FileIndex]);
    if exist(outputFolder, 'dir') ~= 7
    mkdir(outputFolder)
    end

%Now iterate through each of the Pure Ga and Pure Bi files to get the effects of
the droplets on the surface
    sampleGaSbBiData = dlmread(fullfile(sampleFolder, [sampleFolder '...
    _ExperimentalRBS.txt']), '', 1, 0);
```

```
%Get the channel values for the x axis of the plots
    channelGaSbBi(1:GaCutoff, 1) = 1:1:GaCutoff;

%Get the experimental data
    rbsExperimental(1:cutoff, 1) = sampleGaSbBiData(1:cutoff,2);

%Read the simulation data and stopping power for the 300nm GaSbBi film
    GaSbBiSimData = dlmread(fullfile('UniversalGaSbBi', GaSbBiFileListfilmFileIndex, [GaSbBiFileListfilmFileIndex '_1060.txt']), '', 1, 0);
    GaSbBiStopPow = GaSbBiStopPowList(filmFileIndex);

%Preallocate matrices
    weightedGaSbBi = zeros(GaCutoff,2);
    weightedGaSbBi(:,1) = (1 / keV_Ch) * (channelGaSbBi - channelOffset);
    weightedGaSbBi(1:size(GaSbBiSimData,1),2) = keV_Ch * partSR * numGaSbBiPixels * GaSbBiSimData(:,3);
    nonzeroWeightedGaSbBi = weightedGaSbBi(weightedGaSbBi(:,2) ~= 0, :);
    if size(weightedGaSbBi,1) ~= 0
    interpGaSbBiData = interp1(nonzeroWeightedGaSbBi(:,1), nonzeroWeightedGaSbBi(:,2), channelGaSbBi);

%Replace all the NaNs in the interpDropData vectors with 0 so they
%plot correctly
    interpGaSbBiData(isnan(interpGaSbBiData)) = 0;
    else
    interpGaSbBiData = 0;
    end
```

```
    weightedGa = zeros(GaCutoff,2);
    weightedBi = zeros(GaCutoff,2);
    weightedGaDropData = zeros(GaCutoff, 2);
    weightedBiDropData = zeros(GaCutoff, 2);
    for dropletFileIndex = heightFracStart:heightFracIncrement:heightFracEnd

%Define the height fraction
    heightFrac(dropletFileIndex,1) = heightFracFile(dropletFileIndex,1);

%Import the floor and ceiling files from which the RBS at the
%actual thicknesses will be calculated
    GaDropFloor = dlmread(fullfile('UniversalRBS_BI_Ga', ['Ga_' num2str(Bi_Ga_Floor(dropletFile
2)) '.txt']), '', 1, 0);
    BiDropFloor = dlmread(fullfile('UniversalRBS_BI_Ga', ['Bi_' num2str(Bi_Ga_Floor(dropletFileIn
1)) '.txt']), '', 1, 0);
    GaDropCeiling = dlmread(fullfile('UniversalRBS_BI_Ga', ['Ga_' num2str(Bi_Ga_Ceiling(droplet
2)) '.txt']), '', 1, 0);
    BiDropCeiling = dlmread(fullfile('UniversalRBS_BI_Ga', ['Bi_' num2str(Bi_Ga_Ceiling(dropletFi
1)) '.txt']), '', 1, 0);
    GaDropFloor(GaCutoff, 3) = 0;
    BiDropFloor(GaCutoff, 3) = 0;
    GaDropCeiling(GaCutoff, 3) = 0;
    BiDropCeiling(GaCutoff, 3) = 0;
    GaThickness = Bi_Ga_ThicknessList.data(dropletFileIndex,2);
    BiThickness = Bi_Ga_ThicknessList.data(dropletFileIndex,1);

%Set the RBS of Ga and Bi droplets equal to the next highest
```

```
%Ga/Bi droplet RBS - the first two columns are the same
%regardless of which file is used. Column 3 will be replaced
%with the rule of mixtures RBS simulation between the floor and
%ceiling Ga and Bi thicknesses.
    GaDropData(:,1) = (1 / keV_Ch) * (GaDropCeiling(:,1) - channelOffset);
    BiDropData(:,1) = (1 / keV_Ch) * (BiDropCeiling(:,1) - channelOffset);
    GaDropData(:,3) = keV_Ch * partSR * 0.10 * (FloorActualDifference(dropletFileIndex,
2) * GaDropCeiling(:,3) + ...
    CeilingActualDifference(dropletFileIndex, 2) * GaDropFloor(:,3));
    BiDropData(:,3) = keV_Ch * partSR * 0.10 * (FloorActualDifference(dropletFileIndex,
1) * BiDropCeiling(:,3) + ...
    CeilingActualDifference(dropletFileIndex, 1) * BiDropFloor(:,3));

%Need to calculate the thickness of the underlying GaSbBi
%carved out by the droplet etching. Calculates the thickness of
%the droplet beneath the surface, then calculates the
%equivalent atoms/1E15 cmˆ2 thickness in terms of GaSbBi
    Ga_GaSbBiFilmThickness = 1059 - (GaStopPow * GaThickness * (1 - (1 / GaTh-
ickMult))) / GaSbBiStopPow;
    if Ga_GaSbBiFilmThickness ¡ 0
    Ga_GaSbBiFilmThickness = 0;
    end
    Bi_GaSbBiFilmThickness = 1059 - (BiStopPow * BiThickness * (1 - (1 / BiThick-
Mult))) / GaSbBiStopPow;
    if Bi_GaSbBiFilmThickness ¡ 0
    Bi_GaSbBiFilmThickness = 0;
    end
```

```
    Ga_GaSbBiFloorThickness = floor(Ga_GaSbBiFilmThickness / 10) * 10;
    Bi_GaSbBiFloorThickness = floor(Bi_GaSbBiFilmThickness / 10) * 10;
    Ga_GaSbBiCeilingThickness = ceil(Ga_GaSbBiFilmThickness / 10) * 10;
    Bi_GaSbBiCeilingThickness = ceil(Bi_GaSbBiFilmThickness / 10) * 10;
    Ga_GaSbBiFloorData = dlmread(fullfile('UniversalGaSbBi', GaSbBiFileListfilm-
FileIndex, ...
    [GaSbBiFileListfilmFileIndex '_' num2str(Ga_GaSbBiFloorThickness) '.txt']), '',
1, 0);
    Bi_GaSbBiFloorData = dlmread(fullfile('UniversalGaSbBi', GaSbBiFileListfilm-
FileIndex, ...
    [GaSbBiFileListfilmFileIndex '_' num2str(Bi_GaSbBiFloorThickness) '.txt']), '', 1,
0);
    Ga_GaSbBiCeilingData = dlmread(fullfile('UniversalGaSbBi', GaSbBiFileListfilm-
FileIndex, ...
    [GaSbBiFileListfilmFileIndex '_' num2str(Ga_GaSbBiCeilingThickness) '.txt']), '',
1, 0);
    Bi_GaSbBiCeilingData = dlmread(fullfile('UniversalGaSbBi', GaSbBiFileListfilm-
FileIndex, ...
    [GaSbBiFileListfilmFileIndex '_' num2str(Bi_GaSbBiCeilingThickness) '.txt']), '',
1, 0);
    %Pad these data matrices with zeros up to GaCutoff
    Ga_GaSbBiFloorData(GaCutoff, 1) = 0;
    Bi_GaSbBiFloorData(GaCutoff, 1) = 0;
    Ga_GaSbBiCeilingData(GaCutoff, 1) = 0;
    Bi_GaSbBiCeilingData(GaCutoff, 1) = 0;

%Interpolate the data with the given thickness
```

```
if Ga_GaSbBiFilmThickness == 0
Ga_GaSbBiData(:,3) = keV_Ch * partSR * Ga_GaSbBiFloorData(:,3);
else
Ga_GaSbBiData(:,3) = keV_Ch * partSR * 0.10 * ((Ga_GaSbBiFilmThickness - Ga_GaSbBiFloorThickness) * Ga_GaSbBiCeilingData(:,3) + ...
(Ga_GaSbBiCeilingThickness - Ga_GaSbBiFilmThickness)...
* Ga_GaSbBiFloorData(:,3));
end
if Bi_GaSbBiFilmThickness == 0
Bi_GaSbBiData(:,3) = keV_Ch * partSR * Bi_GaSbBiFloorData(:,3);
else
Bi_GaSbBiData(:,3) = keV_Ch * partSR * 0.10 * ((Bi_GaSbBiFilmThickness - Bi_GaSbBiFloorThickness) * Bi_GaSbBiCeilingData(:,3) + ...
(Bi_GaSbBiCeilingThickness - Bi_GaSbBiFilmThickness)...
* Bi_GaSbBiFloorData(:,3));
end

%Now produce the RBS patterns that would exist with the Bi and Ga on top of the GaSbBi film
%Input the RBS data, shifted by the thickness of the droplets. Also add in the Ga and Bi only RBS
GaShiftGaSbBi = [((1 / keV_Ch) * (channelGaSbBi - channelOffset) - (2 * GaStopPow * GaThickness)/(1000 * keV_Ch)) Ga_GaSbBiData(:,3)];
BiShiftGaSbBi = [((1 / keV_Ch) * (channelGaSbBi - channelOffset) - (2 * BiStopPow * BiThickness)/(1000 * keV_Ch)) Bi_GaSbBiData(:,3)];

%Crop all data that is at a channel ¡ 0, weighting by thetaGa or thetaBi, as we
```

```
are only working with the film portion of the RBS spectra.
%We have not added the droplet RBS spectra in yet, and for the area fraction of the
GaSbBi to be 1, we need to weight only by thetaGa or thetaBi.
%Weighting using height fraction and droplet area fraction will cause the film portion
to be overestimated.
%The multiplier corrects the relative yield of the underlying
%GaSbBi film
    GaCropGaSbBi = ((2E6)^2)/((2E6 - (2 * GaStopPow * GaThickness))^2) * GaShift-
GaSbBi(GaShiftGaSbBi(:,1) ¿= 0, :);
    BiCropGaSbBi = ((2E6)^2)/((2E6 - (2 * BiStopPow * BiThickness))^2) * BiShift-
GaSbBi(BiShiftGaSbBi(:,1) ¿= 0, :);

%Now fill the rest of the matrix up to Gacutoff with zeroes
    GaCropGaSbBi(GaCutoff,1) = 0;
    BiCropGaSbBi(GaCutoff,1) = 0;

%Add in the Ga and Bi layer data, weighting the droplet data according to height
fraction and area fraction of the droplets (not the whole surface)
%weightedGa and weightedBi are the summations of all the droplet
%modified GaSbBi RBS spectra only.
    weightedGa(:,2) = weightedGa(:,2) + (heightFrac(dropletFileIndex)...
    /heightFracNumPixelsTotal) * thetaGa(i)/(thetaGa(i) + thetaBi(i))...
    * GaCropGaSbBi(:,2);% Number of GaSbBi pixels under the Ga
    weightedBi(:,2) = weightedBi(:,2) + (heightFrac(dropletFileIndex)...
    /heightFracNumPixelsTotal) * thetaBi(i)/(thetaGa(i) + thetaBi(i))...
    * BiCropGaSbBi(:,2);% Number of GaSbBi pixels under the Bi
    weightedGaDropData(:,2) = weightedGaDropData(:,2) + ...
```

```
    (heightFrac(dropletFileIndex,1)/heightFracNumPixelsTotal)...
    * thetaGa(i)/(thetaGa(i) + thetaBi(i)) * ...
    GaDropData(:,3); %Number of Ga droplet pixels
    weightedBiDropData(:,2) = weightedBiDropData(:,2) + ...
    (heightFrac(dropletFileIndex,1)/heightFracNumPixelsTotal)...
    * thetaBi(i)/(thetaGa(i) + thetaBi(i)) * ...
    BiDropData(:,3); %Number of Bi droplet pixels
    end


%=====================
%Multiply each individual curve by partSRFinal to shift the whole
%curve up or down
    weightedGaSbBi = partSRFinal * weightedGaSbBi;
    weightedGa(:,2) = partSRFinal * weightedGa(:,2);
    weightedBi(:,2) = partSRFinal * weightedBi(:,2);
    weightedGaDropData(:,2) = partSRFinal * weightedGaDropData(:,2);
    weightedBiDropData(:,2) = partSRFinal * weightedBiDropData(:,2);


%Set the weighted droplet channel axes equal to the nonweighted
%channel axes
    weightedGaDropData(:,1) = GaDropData(:,1);
    weightedBiDropData(:,1) = BiDropData(:,1);
    weightedGa(:,1) = (1 / keV_Ch) * (channelGaSbBi - channelOffset);
    weightedBi(:,1) = (1 / keV_Ch) * (channelGaSbBi - channelOffset);
%Need to extract all points where the counts are not zero
    nonzeroWeightedGa = weightedGa(weightedGa(:,2) ~= 0, :);
    nonzeroWeightedBi = weightedBi(weightedBi(:,2) ~= 0, :);
```

```
    nonzeroWeightedGaDropData = weightedGaDropData(...
    weightedGaDropData(:,2) ~= 0, :);
    nonzeroWeightedBiDropData = weightedBiDropData(...
    weightedBiDropData(:,2) ~= 0, :);

%Now we have to interpolate the droplet RBS spectra at each of
%the channelGaSbBi points since the channel axis for the RBS
%data and GaSbBi films are plotted against that while the
%droplet data is plotted against a different set of channel
%axis points
    if size(nonzeroWeightedGaDropData,1) ~= 0
    interpGaDropData = interp1(nonzeroWeightedGaDropData(:,1),...
    nonzeroWeightedGaDropData(:,2), channelGaSbBi);

%Replace all the NaNs in the interpDropData vectors with 0 so they
%plot correctly
    interpGaDropData(isnan(interpGaDropData)) = 0;
    else
    interpGaDropData = zeros(GaCutoff,1);
    end
    if size(nonzeroWeightedBiDropData,1) ~= 0
    interpBiDropData = interp1(nonzeroWeightedBiDropData(:,1),...
    nonzeroWeightedBiDropData(:,2), channelGaSbBi);
    %Replace all the NaNs in the interpDropData vectors with 0 so they
    %plot correctly
    interpBiDropData(isnan(interpBiDropData)) = 0;
    else
```

```
    interpBiDropData = zeros(GaCutoff,1);
    end

%Do the same interpolation with the thinner GaSbBi film under the
%droplets
    if size(nonzeroWeightedGa,1) ~= 0
    interpGaGaSbBiData = interp1(nonzeroWeightedGa(:,1), nonzeroWeightedGa(:,2),
channelGaSbBi);

%Replace all the NaNs in the interpDropData vectors with 0 so they
%plot correctly
    interpGaGaSbBiData(isnan(interpGaGaSbBiData)) = 0;
    else
    interpGaGaSbBiData = zeros(GaCutoff,1);
    end
    if size(nonzeroWeightedBi,1) ~= 0
    interpBiGaSbBiData = interp1(nonzeroWeightedBi(:,1), nonzeroWeightedBi(:,2),
channelGaSbBi);
    %Replace all the NaNs in the interpDropData vectors with 0 so they
    %plot correctly
    interpBiGaSbBiData(isnan(interpBiGaSbBiData)) = 0;
    else
    interpBiGaSbBiData = zeros(GaCutoff,1);
    end
    figure
    disp(['Plotting the RBS for: ' GaSbBiFileListfilmFileIndex])
    hold all
```

```
%Plot the experimental RBS data as a scatter plot
    scatter(channelGaSbBi(:), rbsExperimental(:), 8, [0 0 0],...
    'DisplayName', 'Experimental RBS')

%Now plot the individual composite plots of GaSbBi, Ga, and Bi
    plot(channelGaSbBi, interpGaSbBiData, '–',...
    'DisplayName', 'GaSbBi', 'LineWidth', 2)
    plot(channelGaSbBi, interpGaGaSbBiData + interpGaDropData, '–',...
    'DisplayName', 'Ga/GaSbBi', 'LineWidth', 2)
    plot(channelGaSbBi, interpBiGaSbBiData + interpBiDropData, '–',...
    'DisplayName', 'Bi/GaSbBi', 'LineWidth', 2)

%The following can be uncommented to plot the droplet and covered film components of the spectra separately
    %plot(channelGaSbBi, interpGaGaSbBiData, '–',...
    'DisplayName', 'Ga/GaSbBi', 'LineWidth', 2)
    %plot(channelGaSbBi, interpBiGaSbBiData, '–',...
    'DisplayName', 'Bi/GaSbBi', 'LineWidth', 2)
    %plot(channelGaSbBi, interpGaDropData, '–',...
    'DisplayName', 'Ga Droplets', 'LineWidth', 2)
    %plot(channelGaSbBi, interpBiDropData, '–',...
    'DisplayName', 'Bi Droplets', 'LineWidth', 2)
    plot(channelGaSbBi, interpGaSbBiData + interpGaGaSbBiData + interpBiGaSbBiData + interpGaDropData + interpBiDropData, 'Color', [0.5 0.5 0.5], 'LineWidth', 2, 'DisplayName', 'Combined')
    xlim(unzoomedX), ylim(unzoomedY)
```

```
    xlabel('Channel');
    ylabel('Counts');
    figureTitle = strrep([GaSbBiFileListfilmFileIndex ', thetaGa = '...
    num2str(thetaGa(i)) ' , thetaBi = ' num2str(thetaBi(i))], '_', '_');
    title(figureTitle);
    legend('-DynamicLegend', 'Location', 'NorthEast')
    set(gca, 'Box', 'on')
    if (saveFig == 1)
    print(gcf, '-depsc2', fullfile(outputFolder, ...
    [GaSbBiFileListfilmFileIndex index 'ThetaGa' num2str(thetaGa(i))...
    'ThetaBi' num2str(thetaBi(i)) '.eps']))
    saveas(gcf, fullfile(outputFolder, ...
    [GaSbBiFileListfilmFileIndex index 'ThetaGa' num2str(thetaGa(i))...
    'ThetaBi' num2str(thetaBi(i)) '.fig']), 'fig')
    end

%Save the same figure with the field of view focused on the
%plateaus
    xlim(zoomedX), ylim(zoomedY);

%Limits for the Mar 2013 runs
    %xlim([1400 1850]), ylim([0 1000]);
    if (saveFig == 1)
    print(gcf, '-depsc2', fullfile(outputFolder, ...
    [GaSbBiFileListfilmFileIndex 'Zoomed' index 'ThetaGa'...
    num2str(thetaGa(i)) 'ThetaBi' num2str(thetaBi(i)) '.eps']))
```

```
%Copy the RBS parameters to a file with the same name as the plots
%so we can look up what fitting parameters we used to generate it
    copyfile(fullfile(sampleFolder, 'RBSFittingParameters'), ...
    fullfile(outputFolder, [GaSbBiFileListfilmFileIndex 'Zoomed' index...
    'ThetaGa' num2str(thetaGa(i)) 'ThetaBi' num2str(thetaBi(i)) '.txt']))
    end

%======================
%Close the figures so the plots don't keep accumulating on the same
    %graph
    %close all
    end
    end
```

APPENDIX D

Complete List of All (4×3) Configurations on the Bi/GaSb Phase Diagram

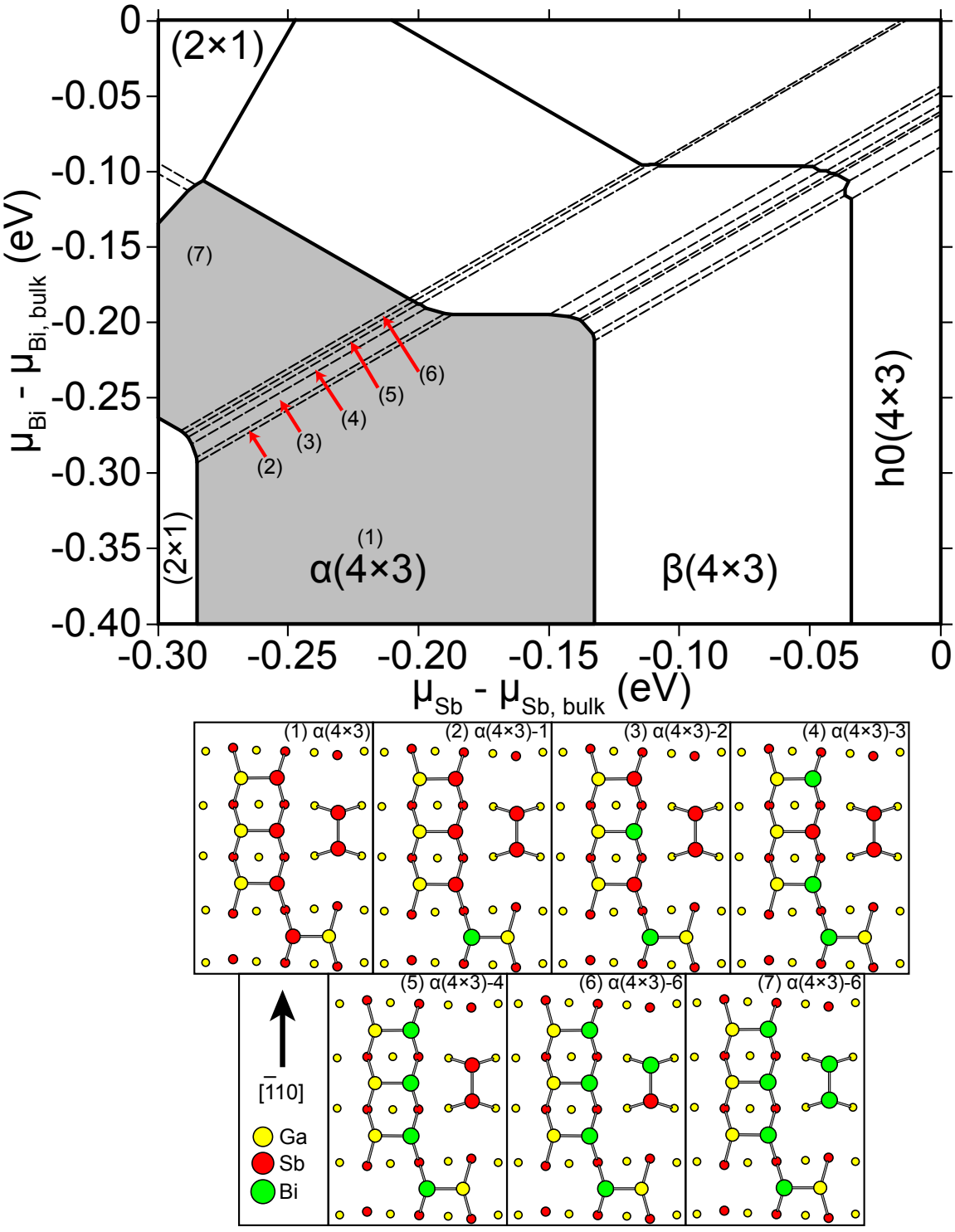

Figure D.1. The stable Bi/GaSb $\alpha(4 \times 3)$ groundstates.

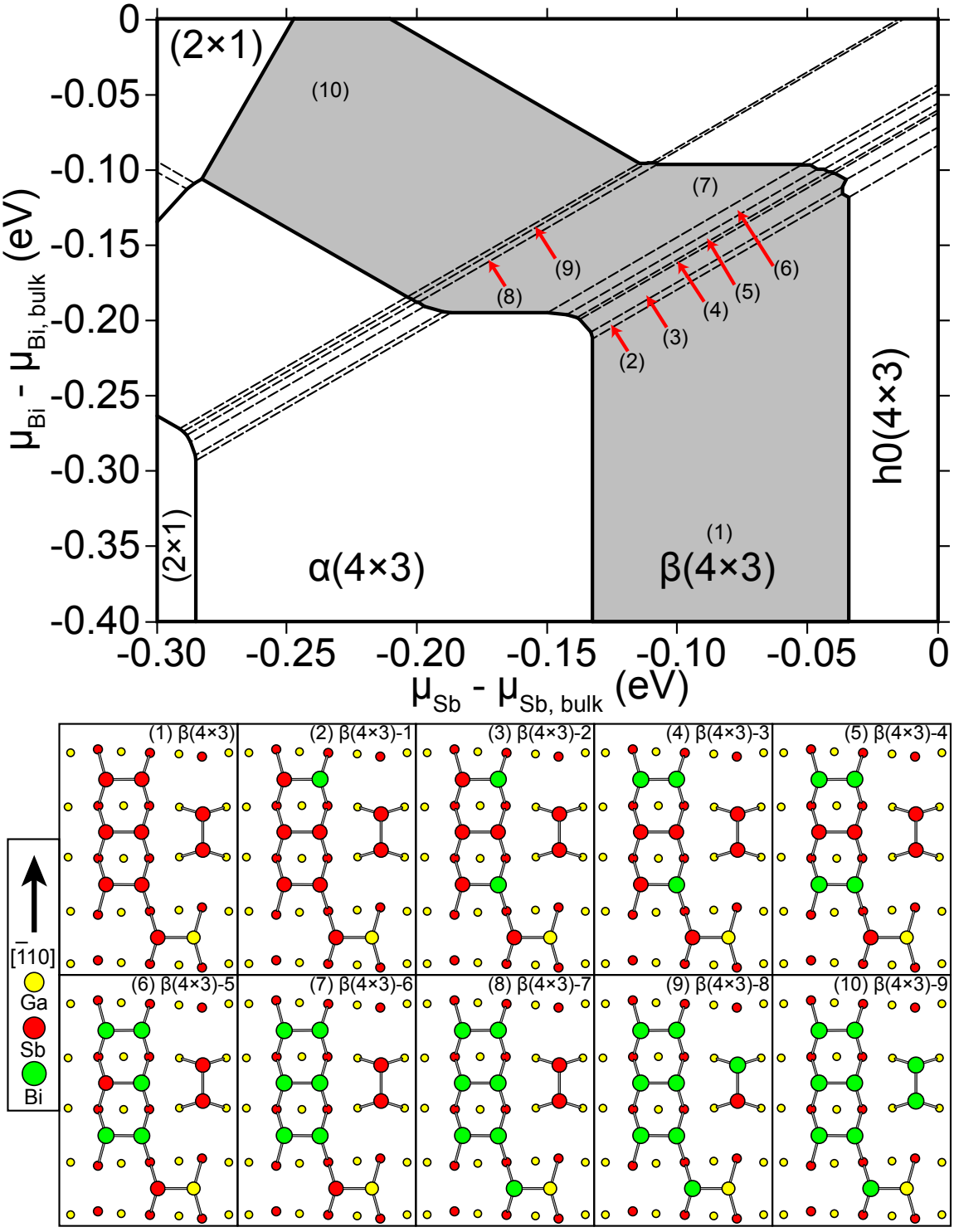

Figure D.2. The stable Bi/GaSb $\beta\,(4\times 3)$ groundstates.

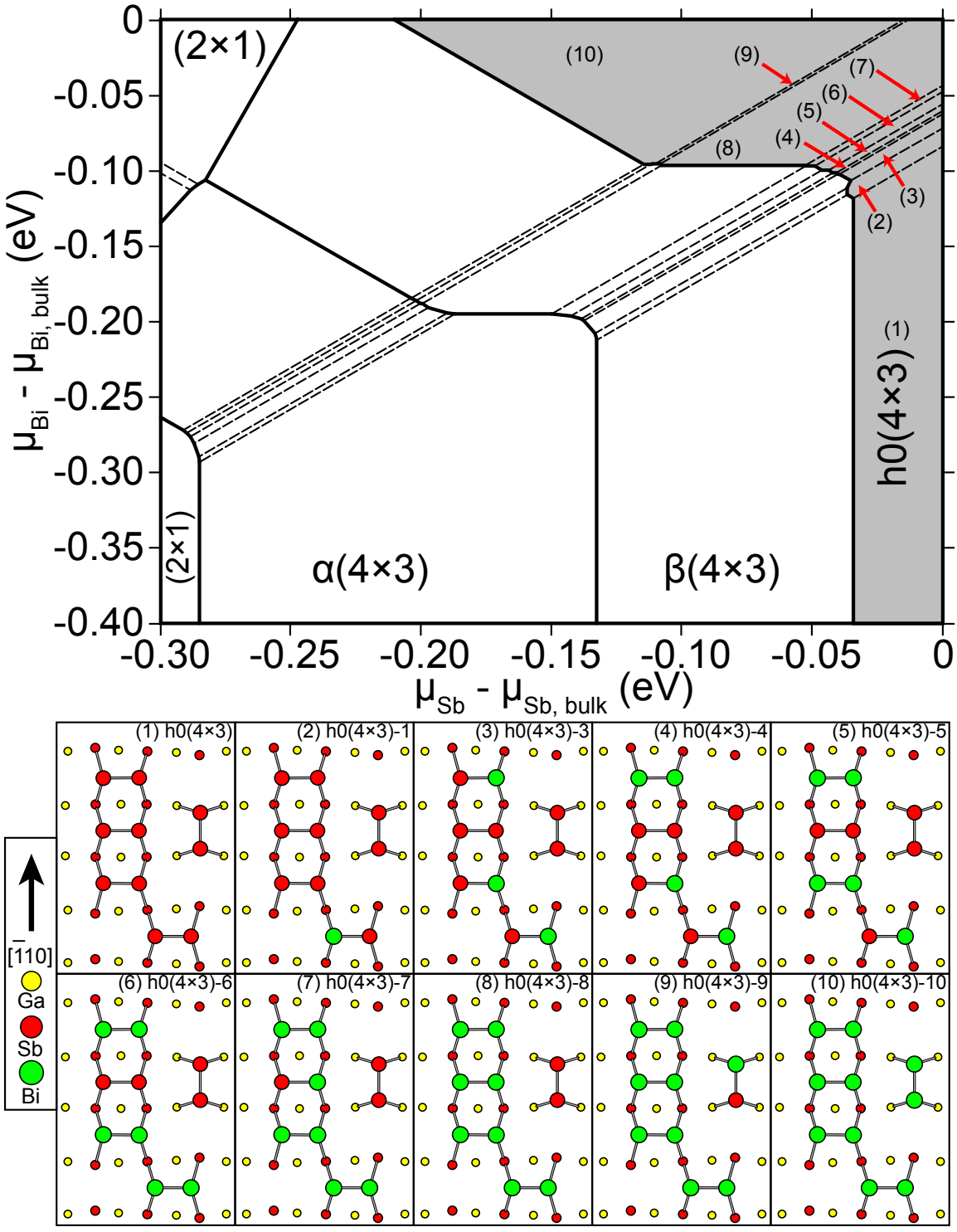

Figure D.3. The stable Bi/GaSb $h0\,(4\times3)$ groundstates.

BIBLIOGRAPHY

BIBLIOGRAPHY

[1] A. Barron, *Molecular Beam Epitaxy* **http://cnx.org/content/m25712/1.2/** (Accessed 5/11/2013).

[2] M. Schmid, *The Scanning Tunneling Microscope* **http://www.iap.tuwien.ac.at/www/surface/stm_gallery/stm_schematic** (Accessed 7/10/2013).

[3] X. Lu, D. A. Beaton, R. B. Lewis, T. Tiedje, Y. Zhang, *Applied Physics Letters* **95**, 041903 (2009).

[4] S. Francoeur, S. Tixier, E. Young, T. Tiedje, A. Mascarenhas, *Physical Review B* **77** (2008).

[5] G. Pettinari, *et al.*, *Applied Physics Letters* **92**, 262105 (2008).

[6] S. Tixier, *et al.*, *Applied Physics Letters* **86**, 112113 (2005).

[7] S. Francoeur, *et al.*, *Applied Physics Letters* **82**, 3874 (2003).

[8] V. Pacebutas, K. Bertulis, G. Aleksejenko, A. Krotkus, *Journal of Materials Science: Materials in Electronics* **20**, 363 (2008).

[9] V. Pacebutas, *et al.*, *Semiconductor Science and Technology* **22**, 819 (2007).

[10] D. A. Beaton, R. B. Lewis, M. Masnadi-Shirazi, T. Tiedje, *Journal Of Applied Physics* **108**, 083708 (2010).

[11] R. N. Kini, L. Bhusal, A. J. Ptak, R. France, A. Mascarenhas, *Journal Of Applied Physics* **106**, 043705 (2009).

[12] R. Kini, *et al.*, *Physical Review B* **83** (2011).

[13] D. G. Cooke, F. A. Hegmann, E. C. Young, T. Tiedje, *Applied Physics Letters* **89**, 122103 (2006).

[14] D. G. Cooke, E. Young, T. Tiedje, e. al, *... Terahertz Science and ...* (2007).

[15] B. Fluegel, *et al.*, *Physical Review Letters* **97**, 067205 (2006).

[16] B. Fluegel, *et al.*, *Physical Review B* **76** (2007).

[17] S. K. Das, T. D. Das, S. Dhar, M. de la Mare, A. Krier, *Infrared physics & technology* **55**, 156 (2012).

[18] T. Tiedje, E. C. Young, A. Mascarenhas, *International Journal Of Nanotechnology* **5**, 963 (2008).

[19] P. Laukkanen, *et al.*, *Physical Review Letters* **100** (2008).

[20] M. Punkkinen, *et al.*, *Physical Review B* **78**, (2008).

[21] M. Ahola-Tuomi, *et al.*, *Surface Science* **600**, 2349 (2006).

[22] E. Young, *physics.ubc.ca* (2006).

[23] M. Masnadi-Shirazi, D. A. Beaton, R. B. Lewis, X. Lu, T. Tiedje, *Journal of Crystal Growth* **338**, 80 (2012).

[24] A. G. Norman, R. France, A. J. Ptak, *Journal Of Vacuum Science & Technology B* **29**, (2011).

[25] R. Osório, J. Bernard, S. Froyen, A. Zunger, *Physical Review B* **45**, 11173 (1992).

[26] P. A. Bone, J. M. Ripalda, G. R. Bell, T. S. Jones, *Surface Science* **600**, 973 (2006).

[27] A. Ohtake, *Surface Science Reports* **63**, 295 (2008).

[28] J. Houze, S. Kim, S. Kim, S. Erwin, e. al, *Physical Review B* (2007).

[29] C. Hogan, R. Magri, R. Del Sole, *Physical Review Letters* **104**, 157402 (2010).

[30] L. Whitman, P. Thibado, S. Erwin, B. Bennett, B. Shanabrook, *Physical Review Letters* **79**, 693 (1997).

[31] Q. Xie, J. E. Van Nostrand, R. L. Jones, J. Sizelove, D. C. Look, *Journal of Crystal Growth* **207**, 255 (1999).

[32] *Michigan Engineering — Welcome to MIBL* **http://www.engin.umich.edu/research/mibl/tandem.html** (Accessed 4/20/2013).

[33] M. Mayer, *SIMNRA User's Guide* , Max-Planck-Institut für Plasmaphysik, Garching, Germany, 6th edn.

[34] M. Mayer, *The fifteenth international conference on the application of accelerators in research and industry* (AIP, 1999), pp. 541–544.

[35] W. Kohn, L. J. Sham, *Physical Review* **140**, A1133 (1965).

[36] P. Hohenberg, *Physical Review* **136**, B864 (1964).

[37] G. KRESSE, J. FURTHMULLER, *Physical Review B* **54**, 11169 (1996).

[38] A. Duzik, J. C. Thomas, A. Van der Ven, J. M. Millunchick, *Physical Review B* **87**, 035313 (2013).

[39] J. SANCHEZ, F. DUCASTELLE, D. GRATIAS, *Physica A* **128**, 334 (1984).

[40] A. Van der Ven, J. C. Thomas, Q. Xu, J. Bhattacharya, *Mathematics and Computers in Simulation* **80**, 1393 (2010).

[41] V. Blum, M. Walorski, A. ZUNGER, *Nature materials* (2005).

[42] N. Metropolis, A. W. Rosenbluth, M. N. Rosenbluth, A. H. Teller, E. Teller, *The journal of chemical physics* **21**, 1087 (1953).

[43] G. Ciatto, *et al.*, *Physical Review B* **78** (2008).

[44] D. L. Sales, *et al.*, *Applied Physics Letters* **98**, 101902 (2011).

[45] P. Laukkanen, *et al.*, *Surface Science* **601**, 3395 (2007).

[46] P. Laukkanen, *et al.*, *Applied Physics Letters* **90**, 082101 (2007).

[47] P. Laukkanen, *et al.*, *Physical Review B* **74** (2006).

[48] P. Laukkanen, *et al.*, *Surface Science* **600**, 3022 (2006).

[49] P. Laukkanen, *et al.*, *Surface Science* **598**, L361 (2005).

[50] D. Usanmaz, M. Cakmak, S. Ellialtioglu, *Journal Of Physics-Condensed Matter* **20**, 265003 (2008).

[51] A. AlZahrani, G. Srivastava, *Physical Review B* **79** (2009).

[52] M. Pillai, S. Kim, S. Ho, S. Barnett, *Journal Of Vacuum Science & Technology B* **18**, 1232 (2000).

[53] E. C. Young, S. Tixier, T. Tiedje, *Journal of Crystal Growth* **279**, 316 (2005).

[54] S. Tixier, M. Adamcyk, E. C. Young, J. H. Schmid, T. Tiedje, *Journal of Crystal Growth* **251**, 449 (2003).

[55] O. Romanyuk, V. Kaganer, R. Shayduk, B. Tinkham, W. Braun, *Physical Review B* **77** (2008).

[56] E. Young, M. Whitwick, T. Tiedje, *physica status solidi ...* (2007).

[57] X. Lu, D. A. Beaton, R. B. Lewis, T. Tiedje, M. B. Whitwick, *Applied Physics Letters* **92**, 192110 (2008).

[58] C. Pearson, C. Dorin, J. Millunchick, B. Orr, *Physical Review Letters* **92**, 056101 (2004).

[59] I. Chizhov, G. Lee, R. Willis, D. Lubyshev, D. Miller, *Physical Review B* **56**, 1013 (1997).

[60] J. Thomas, N. Modine, J. Millunchick, A. Van der Ven, *Physical Review B* **82** (2010).

[61] W. Barvosa-Carter, *et al.*, *Physical Review Letters* **84**, 4649 (2000).

[62] D. VANDERBILT, *Physical Review B* **41**, 7892 (1990).

[63] J. PERDEW, A. ZUNGER, *Physical Review B* **23**, 5048 (1981).

[64] D. CEPERLEY, B. ALDER, *Physical Review Letters* **45**, 566 (1980).

[65] J. Tersoff, D. HAMANN, *Physical Review Letters* **50**, 1998 (1983).

[66] A. Stroppa, X. Duan, M. Peressi, *Materials Science and Engineering: B* **126**, 217 (2006).

[67] A. Stroppa, X. Duan, M. Peressi, D. Furlanetto, S. Modesti, *Physical Review B* **75**, 195335 (2007).

[68] N. Ghaderi, S. J. Hashemifar, H. Akbarzadeh, M. Peressi, *Journal Of Applied Physics* **102**, 074306 (2007).

[69] X. Duan, M. Peressi, S. Baroni, *Physical Review B* **75**, 035338 (2007).

[70] X. Duan, S. Baroni, S. Modesti, M. Peressi, *Applied Physics Letters* **88**, 022115 (2006).

[71] N. Ghaderi, M. Peressi, N. Binggeli, H. Akbarzadeh, *Physical Review B* **81**, 155311 (2010).

[72] G. Ciatto, P. Alippi, A. Amore Bonapasta, T. Tiedje, *Applied Physics Letters* **99**, 141912 (2011).

[73] M. J. Seong, *et al.*, *Superlattices and Microstructures* **37**, 394 (2005).

[74] Z. Jiang, *et al.*, *Semiconductor Science and Technology* **26**, (2011).

[75] S. Jun, *et al.*, *Journal Of Applied Physics* **88**, 4429 (2000).

[76] M. D. Pashley, *Physical Review B* **40**, 10481 (1989).

[77] S.-H. Lee, W. Moritz, M. Scheffler, *Physical Review Letters* **85**, 3890 (2000).

[78] A. Duzik, J. Thomas, J. Millunchick, J. Lang, e. al, *Surface Science* **606**, 1203 (2012).

[79] J. Thomas, J. Millunchick, N. Modine, A. Van der Ven, *Physical Review B* **80** (2009).

[80] R. Wixom, N. Modine, G. Stringfellow, *Physical Review B* **67**, 115309 (2003).

[81] S. Froyen, A. Zunger, *Physical Review B* **53**, 4570 (1996).

[82] R. B. Lewis, D. A. Beaton, X. Lu, T. Tiedje, *Journal of Crystal Growth* **311**, 1872 (2009).

[83] S. Tixier, *et al.*, *Applied Physics Letters* **82**, 2245 (2003).

[84] M. Yoshimoto, *et al.*, *Japanese Journal of Applied Physics* **42**, L1235 (2003).

[85] A. J. Ptak, *et al.*, *Journal of Crystal Growth* **338**, 107 (2012).

[86] Y. Song, S. Wang, I. S. Roy, P. Shi, e. al, *Journal of Vacuum ...* (2012).

[87] G. Vardar, S. W. Paleg, M. V. Warren, M. Kang, e. al, *Applied Physics ...* (2013).

[88] M. Henini, *Molecular Beam Epitaxy*, From Research to Mass Production (Elsevier Science, 2012).

[89] C. Girard, J. P. Bros, J. Agren, L. Kaufman, *Calphad* (1985).

[90] K. Reyes, *et al.*, *arXiv.org, 1211.0486v4* (2012).

[91] Z. M. Wang, B. L. Liang, K. A. Sablon, G. J. Salamo, *Applied Physics Letters* **90**, 113120 (2007).

[92] M. DeJarld, K. Reyes, P. Smereka, J. M. Millunchick, *Applied Physics Letters* **102**, 133107 (2013).

[93] S. Wang, Y. Song, I. S. Roy, *Transparent Optical Networks (ICTON ...* (2011).

[94] J. E. Bickel, N. A. Modine, A. Van der Ven, J. Mirecki Millunchick, *Applied Physics Letters* **92**, 062104 (2008).

[95] J. Bickel, N. Modine, C. Pearson, J. Millunchick, *Physical Review B* **77** (2008).

[96] J. E. Bickel, C. Pearson, J. M. Millunchick, *Surface Science* **603**, 14 (2009).

[97] J. E. Bickel, N. A. Modine, J. M. Millunchick, *Surface Science* **603**, 2945 (2009).

[98] C. Hogan, R. Magri, R. Del Sole, *Physica Status Solidi B-Basic Solid State Physics* **247**, 1960 (2010).

[99] A. Van der Ven, J. Thomas, Q. Xu, B. Swoboda, D. Morgan, *Physical Review B* **78**, 104306 (2008).

[100] B. Puchala, A. Van der Ven, *Physical Review B* **in review** (2013).

[101] A. Bracker, M. Yang, B. Bennett, J. Culbertson, W. Moore, *Journal of Crystal Growth* **220**, 384 (2000).

[102] F. Bastiman, A. G. Cullis, J. P. R. David, S. J. Sweeney, *Journal of Crystal Growth* **341**, 19 (2012).

[103] F. Bastiman, Y. Qiu, T. Walther, *Journal of Physics: Conference Series* **326**, 012060 (2011).

[104] A. G. Norman, R. France, A. J. Ptak, *Journal Of Vacuum Science & Technology B* **29**, 03C121 (2011).

[105] F. Bastiman, A. R. B. Mohmad, J. S. Ng, J. P. R. David, S. J. Sweeney, *Journal of crystal ...* **338**, 57 (2012).

[106] Y. Takehara, *et al.*, *Japanese Journal of Applied Physics* **45**, 67 (2006).

[107] I. Moussa, H. Fitouri, A. Rebey, B. El Jani, *Thin Solid Films* **516**, 8372 (2008).